eman ta zabal zazu

Universidad del País Vasco

Euskal Herriko Unibertsitatea

Doctoral Thesis

Development of New Ni – Mn – Ga based High Temperature Shape Memory Alloys

Anabel Pérez Checa

Supervisors:

Prof. Jose Manuel Barandiarán

Prof. Volodymyr Chernenko

2019

Agradecimientos

"El tiempo es la cosa más valiosa que una persona puede gastar"

Theophrastus (300-287 a.C.)

Para todos los que me regalaron su tiempo:

Llega sin duda la parte más difícil de escribir de toda una tesis doctoral, los agradecimientos. No es tanto por no saber que agradecer si no por no dejar nada ni a nadie de todos los que han sido participes de este trabajo, que no son pocos.

En primer lugar, me gustaría agradecer a mis directores, Manu Barandiarán y Volodymyr Chernenko, la oportunidad y el apoyo que me han dado antes y durante la realización de esta tesis, ya que sin ellos nunca habría comenzado este camino.

Quiero agradecer también a la Fundación BCMaterials por la oportunidad que me otorgaron de realizar allí mi tesis. También por el uso de las instalaciones y la inestimable ayuda de todos sus componentes. Agradezco también al departamento de Electricidad y Electrónica, en el que he pasado gran parte del tiempo, por hacerme sentir como una más, y por la ayuda que me han brindado en todo momento; así mismo doy las gracias al departamento de Química Macromolecular en el que he realizado gran parte de mis medidas de DSC y DMA.

Gracias al Gobierno Vasco por la financiación concedida mediante la beca pre-doctoral (PRE-2015-1-0060).

No podría resumir solo en unas líneas la ayuda y el tiempo invertido por mi director en la sombra Jorge Feuchtwanger, el cuál ha dedicado su tiempo, esfuerzo, conocimientos y habilidades, que son muchas, en todas y cada una de las partes de este trabajo. Sin duda, gran parte del mérito de estos resultados son suyos.

No puedo olvidarme de mencionar al inmejorable Sgaikaa, conocido como Iñaki

Orue, por todo su tiempo y dedicación, pero sobre todo por su paciencia y predisposición para ayudar con cualquier imprevisto y solucionar el más grande de los problemas, no solo científicos si no mentales también. Así mismo, quiero agradecerles a Ivan por toda su ayuda, y transmisión de conocimiento y experiencia; y a Patricia que me ha atendido ante mis múltiples dudas, y en especial las del maravilloso y sencillo mundo de los neutrones... Gracias por los viajes a Holanda y al ILL y por todo el tiempo que me has dedicado. No podría dejar sin mencionar a Txema, que aunque tarde, llegó para revolucionar el tema y el grupo con grandes ideas y gran motivación, has aportado grandes cosas en este último año. Gracias también a Aitor Larrañaga no solo por las medidas de rayos X, si no por su dedicación y simpatía, y por estar siempre disponible para ruegos y preguntas.

I also had the privilege to work in an exceptional research group from Professor Kari Ullakko, in Finland. Thank you for the fruitful collaborations and research stays, especially to Dr. Oleksii Sozinov, Dr. Andrey Saren, Aleksandr Soroka, Janne Huimasalo and Dennys Musiienko for all their help and time.

Especial mención al *"Akelarre"*, una de las cosas que, sin duda, más voy a añorar, por nuestros viajes, quedadas, charlas, eventos, noticias, compañia y amistad, a Maite, Irati, Lulu, Libe, Catarina y a Martim, o primeiro bebê do Akelarre, GRACIAS!!!.

Una de las cosas que caracteriza al mundo de la ciencia es el ir y venir de gente, gente que te marca y te acompaña en distintas etapas, y que en mayor o menor medida son también responsables de esta tesis. No me olvido de todos los compañeros que han estado conmigo durante estos 4 años: la gente del departamento; Luca, Jorge S, Mattin, Iraultza, Eneko A, Lulu, Dani, Irati, Maite, Libe, Eneko G, Popi, Andoni, Catarina, Edu, Jorge, Mireia, Bea, Nerea, David G, Oscar, Inari, los Javis (Masa y Hamilton), Rosa, Pablo, Patricia, Pegah, Ali, Janire; Esti, Raquel, Raul N, Vaisleios, y a todo aquel que en este momento se me pueda olvidar..; a mis compañeros del BCMaterials, tanto a los más veteranos como a las nuevas incorporaciones, las que, a pesar de haber coincidido menos tiempo, han aportado su granito de arena.

Sin olvidar a *Furgoguay on the rocks* que han hecho mis viajes Donosti-Bilbao Bilbao-Donosti mucho más amenos, con desayunos incluidos, y momentos de terapia y risas (creo que no habría durado ni media tesis sin vosotros) eskerrik asko!

Y que decir de mis padres, mi hermano, patito, yaya y toda mi familia que me ha acompañado durante toda la vida, en todas y cada una de mis decisiones. Habéis sido mis guias y sin vosotros seguro que no habría llegado hasta aqui.

Azkenik.. baina hain garrantzitsua, Aitorei ere eman nahi dizkiot eskerrak. Zure pazientziagatik, zure laguntzagatik, bueno.. guztiagatik eskerrik asko zuri eta zure familiari!

Resumen

El desarrollo de procesos y tecnologías más eficientes en campos como aeronáutica, energía o robótica, requiere del diseño de nuevos materiales inteligentes que cubran las necesidades y exigencias de las nuevas aplicaciones. Dentro de los materiales inteligentes, las aleaciones con memoria de forma comprenden un grupo de materiales ampliamente utilizado como sensores y actuadores, dadas sus interesantes propiedades. El interés por estas aleaciones reside en su capacidad de presentar grandes deformaciones de manera reversible, las cuales, pueden ser inducidas mediante campo magnético, esfuerzo mecánico o temperatura. Estas aleaciones deben sus propiedades a una transformación de fase de primer orden, denominada transformación martensítica, que tiene lugar entre una fase de alta simetría a alta temperatura (austenita), y otra de menor simetría a baja temperatura (martensita). Esta fase de baja simetría o martensita, es de gran importancia debido a la formación, dutante la transformación, de variantes cristalográficas equivalentes a partir de un solo cristal de austenita.

Este tipo de aleaciones puede dividirse principalmente en dos grupos: aleaciones con memoria de forma convencional, conocidas como SMAs (Shape Memory Alloys) por sus siglas en inglés, y aleaciones con memoria de forma ferromagnética, FSMAs (Ferromagnetic Shape Memory Alloys). En ambos casos, la deformación inducida por temperatura o esfuerzo mecánico y temperatura, radica en la reorientación de las maclas en la fase martensita, sin embargo, mientras que en el caso de la memoria de forma convencional, la deformación se produce al pasar de la fase austenita a una martensita reorientada, la memoria de forma magnética, que se produce por efecto del campo magnético, ocurre enteramente en la fase martensita ferromagnética.

El principal problema para el uso real de estas aleaciones en las nuevas tecnologías es la necesidad de incrementar su temperatura de actuación por encima de los 373 K. Dado que el rango de aplicación viene determinado por la temperatura de transformación martensítica, (T_M), así como por la temperatura de Curie (T_C) en

el caso de las ferromagnéticas, el estudio de la evolución de dichas temperaturas con la estructura o la composición son determinantes para su diseño.

Uno de los sistemas más ampliamente estudiados, tanto en memoria de forma convencional como ferromagnética, son las aleaciones no estequiométricas basadas en el compuesto intermetálico tipo Heusler Ni_2MnGa. Dichas aleaciones presentan deformaciones de hasta un 12 % al ser sometidas a un campo magnético externo dando una respuesta inmediata en el orden de milisegundos. Así mismo, el fuerte acoplamiento que presentan entre la estructura cristalina y las propiedades magnéticas hace de ellas materiales muy interesantes y prometedores para su aplicación en el campo de sensores y actuadores.

A pesar de ello, la implementación real de estas aleaciones a alta temperatura es aún un campo en desarrollo debido a numerosos problemas sin resolver, como son, la incapacidad de elevar los intervalos de actuación manteniendo simultáneamente grandes deformaciones, la inestabilidad térmica y termomecánica, desestabilizaciones de la fase martensita, descomposición de fases y la necesidad de aplicar esfuerzos muy elevados para inducir la reorientación de maclas, entre otros.

Por todo ello, el objetivo principal de esta tesis consiste en el estudio y diseño de nuevas aleaciones con memoria de forma, tanto convencional como magnética, con funcionalidad a alta temperatura, teniendo como fin último su utilización en un futuro cercano en sensores y actuadores. En particular se centrará en el estudio del efecto de la composición en las distintas propiedades y la relación existente entre la estructura y el carácter magnético en estas aleaciones son de suma importancia para su óptimo diseño e implementación.

Con este propósito la tesis se ha dividido en cuatro capítulos de resultados: (i) desarrollo de aleaciones con memoria de forma convencional por encima de los 670 K y estudio de su estabilidad térmica y termomecánica; (ii) desarrollo de aleaciones con memoria de forma magnética por encima de 373 K y estudio del efecto de la adición de elementos (Fe, Co y Cu) en las propiedades magnéticas y estructurales; (iii) análisis de la relación existente entre el magnetismo y la estructura en las aleaciones multicomponentes (Ni–Mn–Ga–Fe–Co–Cu); y por último, (iv) evaluación de los parámetros críticos para la obtención del efecto de memoria de forma magnética a alta temperatura y su dependencia con la temperatura y la composición en monocristales de Ni–Mn–Ga–Fe–Co–Cu con T_M por encima de los 373 K.

En primer lugar, con el fin de analizar el efecto de la composición en las temperaturas de transformación y obtener aleaciones con T_M >670 K y deformaciones de al menos el 4 %, se ha comenzado con un sistema más sencillo de memoria de forma convencional basado en distintas composiciones de Ni–Mn–Ga. Para ello, se han identificado las diferentes fases presentes, β y $\beta + \gamma$, acorde al diagrama ternario NiMnGa, y se han obtenido muestras representativas de cada zona con temperaturas máximas de transformación de 773 K. Para este estudio se han utilizado muestras tanto policristalinas, producidas mediante horno de inducción, como monocristalinas, crecidas mediante el método de fusión por zona en un horno óptico. Por otro lado, se ha realizado un estudio de estabilidad térmica, mediante calorimetría diferencial de barrido (DSC) y termomecánica, mediante análisis dinamo-mecánico (DMA); y se ha evaluado el efecto de los tratamientos térmicos en dicha estabilidad. Este estudio ha permitido dilucidar los distintos mecanismos de estabilización de las fases β y $\beta + \gamma$. En el caso de las muestras pertenecientes a la región bifásica, el ciclado térmico ha dado lugar a una reducción de las temperaturas de transformación, así como de la cantidad de fase transformable, debido a la precipitación de fase γ, mientras que, para la región monofásica, no se ha observado ningun cambio. En cuanto a los ciclados termomecánicos realizados en los monocristales, se ha obtenido una reducción tanto de las temperaturas de transformación como de la deformación en ambas fases, alcanzando la estabilización alrededor de los 200 ciclos. A pesar de que la combinación de esfuerzo y temperatura ha resultado ser suficiente para inducir la precipitación de segundas fases en ambas regiones, la aplicación de los tratamientos termomecánicos propuestos ha dado lugar a la obtención de un monocristal con deformaciones estables del 3 % alrededor de 673 K.

En el capítulo 3, se han definido tres sistemas multicomponentes basados en la adición simultanea de Fe, Co y Cu con el fin de obtener una T_M >373 K y una T_C >423 K. De igual modo, se ha evaluado el efecto de la composición en las propiedades magnéticas y estructurales. El primer sistema, $Ni_{45}Co_5Mn_{25-x}Fe_xGa_{20}Cu_5$, se eligió con el fin de analizar el efecto de la sustitución de Mn por Fe (de 0 a 8 %) manteniendo constantes en un 5 % el Co y el Cu. El aumento de Fe ha dado lugar a una disminución de la T_M y de la relación estructural entre los parámetros de red (c/a) y a un incremento de la T_C. Así mismo, se ha obtenido un aumento de la imanación de saturación, debido, posiblemente, al incremento de las interacciones de canje ferromagnético.

Mediante los resultados obtenidos en el sistema $Ni_{45}Co_5Mn_{25-x}Fe_xGa_{20}Cu_5$ (x = 0 - 8) se definieron dos nuevas series con el fin de estudiar los efectos de la sustitución de Mn y/o Ga por Cu. Las dos series estudiadas fueron $Ni_{43}Co_7Mn_{20-x}Fe_2Ga_{21}Cu_{7+x}$ y (x = 0.25, 0.5, 0.75, and 1.0 at. %), y $Ni_{43}Co_7Mn_{20}Fe_2Ga_{21-x}Cu_{7+x}$ (x = 0.5, 1 y 1.5 at. %). Mediante la primera serie se ha obtenido una disminución inicial de la T_M y el c/a para valores de Cu $\leq$ 7.5 at. %, a partir del cual, comienzan a aumentar. Las temperaturas de Curie de la austenita permanecen constantes alrededor de los 439 K para todo el rango estudiado. Por otro lado, los resultados de la segunda serie revelan un incremento de la T_M y el c/a con el aumento de Cu mientras que la temperatura de Curie de la martensita ($T_C{}^M$) disminuye y la relativa a la austenita ($T_C{}^A$) permanece constante. Las tendencias observadas en ambas series están directamente relacionadas con el efecto del Cu en la estructura.

El estudio de estos tres sistemas ha permitido dilucidar la fuerte relación existente entre la estructura y las propiedades. En la Figura 1 se muestra la relación entre el c/a y la T_M de todas las muestras estudiadas junto con composiciones de Ni–Mn–Ga previamente publicadas por N. Lanska et al.[1] Esta figura muestra además el efecto de la adición de Fe, Co y Cu en la reducción del c/a, respecto a las aleaciones de Ni–Mn–Ga, lo que, experimentalmente está relacionado con una disminución del esfuerzo de maclado.

Por último, se han obtenido tres composiciones: (S0) $Ni_{43}Co_7Mn_{20}Fe_2Ga_{21}Cu_7$, (Fe4) $Ni_{45}Co_5Mn_{21}Fe_4Ga_{20}Cu_5$ y (Fe5) $Ni_{45}Co_5Mn_{20}Fe_5Ga_{20}Cu_5$, que presentan simultaneamente valores de T_M y T_C >373 K y 423 K respectivamente.

En el capítulo 4, con el fin de determinar el órden atómico en estos materiales y determinar la contribución magnética de los diferentes átomos y su relación con las posiciones atómicas y las distancias interatomicas, se ha realizado un estudio mediante difracción de neutrones en muestras tanto policristalinas como monocristalinas. Las muestras seleccionadas son las pertenecientes a la serie de Fe descrita en el capítulo 3. La muestra monocristalina se creció a partir de la composición de Fe 5 % mediante el método Bridgman-Stockbarger.

El análisis estructural muestra dos tipos de estructuras cristalográficas: una cúbica Fm-3m correspondiente a la austenita, y una fase tetragonal de simetría I4/mmm, correspondiente a la martensita. Respecto al orden atómico, los resultados revelan una clara tendencia del Cu por ocupar posiciones de Mn, mientras que las preferencias del Co y el Fe varian en función de la cantidad de Fe incorporado. Para un bajo

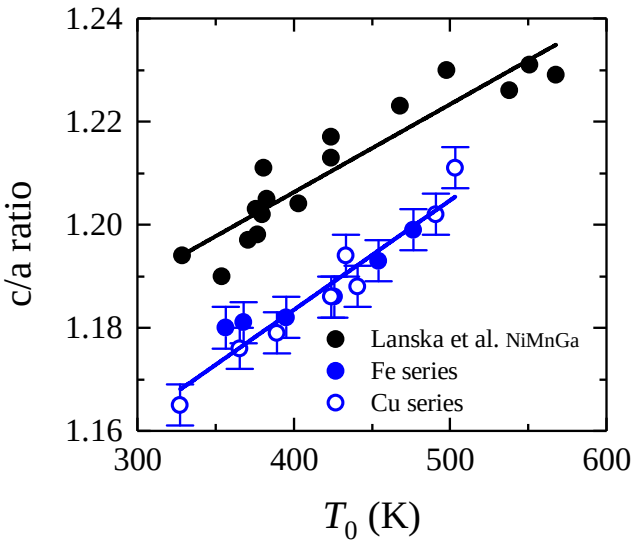

Figura 1: Dependencia de las temperaturas de transformación (T_0) con el c/a para las muestras con Fe (círculos rellenos azules) y Cu (círculos huecos azules), y los datos obtenidos por Lanska et al.[1] en relación a muestras de Ni–Mn–Ga (círculos rellenos negros).

contenido en Fe, el Co se distribuye entre las posiciones de Ni y Ga, mientras que a altas concentraciones, se ve mayoritariamente relegado a las posiciones del Ga. En el caso del Fe, este tiende a ocupar las posiciones de Ni y Mn. Por otro lado, el Mn se distribuye entre las 3 posiciones existentes, y el Ni y el Ga se mantienen en sus respectivas posiciones. Esta disposición de los átomos tiene una gran influencia en las propiedades magéticas, debido a las distintas distancias Mn–Mn presentes en la celda unidad. Considerando que el acoplamiento del Mn–Mn a distancias cortas se invierte, pasando a ser antiferromagnético, se ha correlacionado el aumento de las imanación de saturación con la disminución de Mn en posiciones antiferromagnéticas y, por tanto, con el orden atómico.

De igual modo, se ha realizado un análisis mediante diffracción de neutrones polarizados sobre la muestra monocristalina $Ni_{45}Co_5Mn_{21}Fe_4Ga_{20}Cu_5$. Esta técnica permite determinar la contribución magnética promedio de los átomos magnéticos para cada posición, así como la obtención del mapa de densidad de spin para las fases austenita y martensita. Los valores obtenidos evidencian una contribución magnética mayoritaria localizada en las posiciones de Mn, apreciándose en menor medida, en las posiciones de Ni, y en menor aún, en las de Ga (Ver Figura 2). Los resultados obtenidos mediante esta técnica en cuanto al momento magnético total, se compa-

raron con los obtenidos mediante las medidas magnéticas.

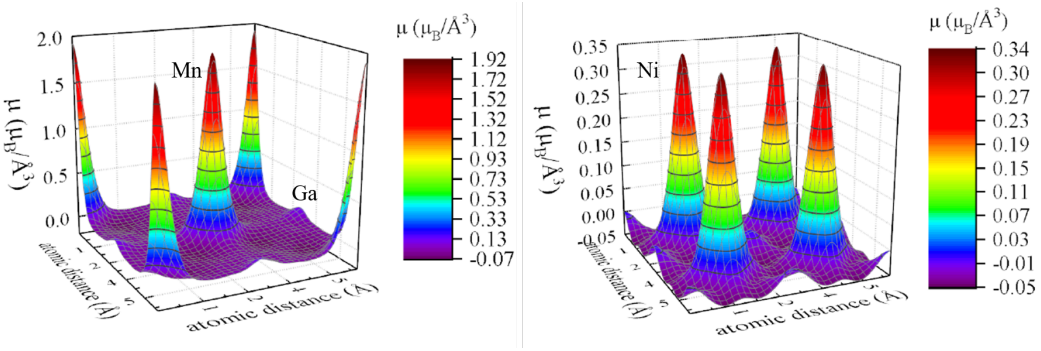

Figura 2: Mapa de densidad de spin en el plano (100) para x = 0 (izq) y 1/4 (dcha) obtenido para la estructura $L2_1$ medida en la fase ferromagnética a 400 K con un campo aplicado de 7 T.

Por último, en el capítulo 5, se han seleccionado las muestras policristalinas estudiadas en las series de Cu y Fe, que presentaban valores de T_M y T_C por encima de 373 K y 423 K respectivamente, y se han crecido monocristales a partir de ellas mediante el método Bridgman-Stockbarger.

A partir de dichos monocristales, se ha realizado un estudio sistemático de la evolución de la estructura, el esfuerzo de maclado (*twinning stress*), σ_{tw}, y las propiedades magnéticas, (constante de anisotropía (K_u) y el esfuerzo magnético (*magnetostress*) (σ_{mag})), en función de la temperatura y la composición. Estos parámetros son esenciales para la obtención de actuación magnética a alta temperatura. Los resultados obtenidos muestran una dependencia linear de σ_{tw}, K_u, y σ_{mag} con la temperatura para todas las muestras, mientras que su dependencia con la estructura es más compleja y está influenciada por la composición. Así mismo, la adición de hierro ha sido crucial en el diseño de nuevas aleaciones, resultando en la mejora de las propiedades magnéticas, (incremento de la constante de anisotropía y el *magnetostress*); y estructurales (la reducción de la tetragonalidad y el *twinning stress*). Sin embargo, es necesario reducir, incluso más, el σ_{tw} con el fin de satisfacer la condición de $\sigma_{mag} > \sigma_{tw}$ necesaria para obtener actuación magnética a altas temperaturas.

Abstract

In recent years, the evolution of current technologies has generated ever more stringent requirements for shape memory alloys (SMAs). One of the main hurdles to overcome for a real-world implementation of these materials is the increase of the actuation temperature ranges over 373 K.

This Thesis deals with the design and study of new conventional SMAs and new ferromagnetic shape memory alloys (FSMAs), both based on the Ni–Mn–Ga system, for high temperature applications. With this aim, a first Ni–Mn–Ga system, exhibiting non-modulated martensite, was designed for high temperature SMAs. A single crystal growth technology was optimized for the alloy production. The systematic study performed for this system revealed the effect composition has on the martensitic transformation temperatures and determined the thermal and thermomechanical stabilization mechanisms of the different phase regions. Particularly, the elaborated thermo-mechanical cycling resulted in record-breaking parameters of shape memory actuation: a stable cyclic strain of 3% at 673 K.

The results obtained in the ternary Ni–Mn–Ga system served as the starting point for the subsequent work, which consisted in the development of a more complex multicomponent system for high temperature ferromagnetic shape memory applications. In this case, the simultaneous addition of Fe, Co and Cu to a quasi-stoichiometric Ni_2MnGa systems was selected with the aim of increasing both the martensitic transformation and Curie temperatures to over 373 K and 423 K respectively. The composition and temperature dependencies of the transformation, as well as the structural and magnetic properties of the non-modulated martensites were analyzed for three different series based on the multicomponent Ni-Mn-Ga-Co-Fe-Cu system. The first series, $Ni_{45}Co_5Mn_{25-x}Fe_xGa_{20}Cu_5$, allowed us to correlate the changes in the properties with the addition of Fe, whereas the $Ni_{43}Co_7Mn_{20-x}Fe_2Ga_{21}Cu_{7+x}$ and $Ni_{43}Co_7Mn_{20}Fe_2Ga_{21-x}Cu_{7+x}$ series enabled an in-depth analysis of the effect of

Mn/Ga substitution by Cu.

Based on these results, in which a relation between composition, structure, and magnetic properties was found, an in-depth research of the interdependence between these properties by means of neutron diffraction was performed. The unique capacities provided by the neutron scattering techniques made it possible to resolve the atomic order of the Fe alloys series, this being correlated with an increase of the saturation magnetization. The later effect is found to be produced by the variation of exchange interactions between Mn–Mn pairs, which depends on their pairwise distances in the crystallographic unit cell. The results from polarized neutron diffraction studies led to the determination of the magnetic moment distribution in the different unique sites of the martensite and austenite structures.

The last part of the thesis provides a path towards the applicability of high temperature FSMAs by studying the functional properties of the Ni–Mn–Ga–Co–Fe–Cu alloys developed for the exploration of the possibility of magnetic actuation in non-modulated tetragonal FSMAs. The relevant parameters for obtaining a large magnetostrain at high temperature, such as magnetocrystalline anisotropy, twinning stress and magnetostress, were analyzed as a function of the temperature and composition. For this study, single crystals with three compositions selected from the previous results, exhibiting simultaneously high martensitic and Curie temperatures, were grown. The same linear temperature dependence of the magnetocrystalline anisotropy, twinning stress and magnetostress was obtained in all the alloys. However, their dependence with the tetragonality ratio proved to be more complex and compostion dependent. The parameters obtained for one of the alloys at about 370 K were very close to fulfilling the conditions for large magnetostrains in non-modulated martensites.

This Thesis sheds light on the field of high temperture actuation of FSMAs, contributing to it with a fundamental understanding of the transformation behavior in both Ni–Mn–Ga and Ni–Mn–Ga–Co–Fe–Cu alloy systems, and highlighting their large potential as actuator materials for high temperature SMA and FSMA inovative applications, respectively.

List of Publications

This thesis is supported on the following publications:

1. A. Pérez-Checa, J. Feuchtwanger, J. M. Barandiaran, and V. A. Chernenko, "Ni-Mn-Ga high temperature shape memory alloys: Function stability in β and $\beta + \gamma$ regions" *Journal of Alloys and Compounds*, vol. 741, pp. 148-154, 2018

2. A. Pérez-Checa, J. Feuchtwanger, D. Musiienko, A. Sozinov, J. M. Barandiaran, K. Ullakko and V. A. Chernenko, "High temperature $Ni_{45}Co_5Mn_{25-x}Fe_xGa_{20}Cu_5$ ferromagnetic shape memory alloys" *Scripta Materialia*, vol. 134, pp. 119-122, 2017.

3. A. Pérez-Checa, J. Feuchtwanger, J. M. Barandiaran, A. Sozinov, K. Ullakko and V. A. Chernenko, "Ni–Mn–Ga–(Co, Fe, Cu) high temperature ferromagnetic shape memory alloys: Effect of Mn and Ga replacement by Cu" *Scripta Materialia*, vol. 154, pp. 131-133, 2018.

4. A. Pérez-Checa, D. Musiienko, A. Saren, A. Soroka, J. Feuchtwanger, A. Sozinov, J. M. Barandiaran, K. Ullakko and V. A. Chernenko, "Study of the critical parameters for magnetic field-induced strain in high temperature Ni-Mn-Ga-Co-Cu-Fe single crystals" *Scripta Materialia*, vol. 158, pp. 16-19, 2019.

Contents

List of Figures

List of Tables

Chapter 1

Introduction

1.1 Active Materials

Active materials are those that exhibit the ability to modify some of their physical properties in the presence of an external stimulus. Particularly, the materials that respond mechanically to applied external fields (thermal, electric, magnetic ...) comprise an important class of active materials. Historically, they have proved to be very interesting from a scientific point of view, due to the complex physical mechanisms acting behind the observed behavior; and from the technological point of view for their application in new devices such as sensors or actuators. Active materials with mechanical properties can be further subdivided into materials that exhibit direct or indirect coupling. In the direct coupling, either the mechanical stress or an external field could act as the input force while the other becomes the output. In contrast, in the indirect coupling, the mechanical properties can be modified by the external field through the change of a third property. This indirect coupling lacks the reciprocity of the two-way coupling of the active materials that directly couple two fields. Classical materials with direct coupling are piezoelectric ceramics (PZT),[2] magnetostrictive materials (Terfenol-D)[3,4] or conventional (NiTinol) and magnetic shape memory alloys (Ni-Mn-Ga). Shape memory alloys (SMAs) comprise an important class of active materials with direct coupling. These materials are characterized by their ability to recover their previous form when subjected to a certain external stimulus such as thermomechanical or magnetic variations. SMAs have attracted considerable attention in recent years in a broad range of applications, due to their unique properties. The first observation of the shape memory effect was

in 1932 by Arne Ölander[5] who found the pseudoelastic effect in an Au-Cd alloy. Nevertheless, this effect was not widely studied until William Buehler and Frederick Wang[6] found the shape memory effect (SME) in a nickel-titanium (NiTi) alloy in 1963. Apart from their ability to retain their shape, these materials are able to exhibit strains even up to around 12 %. Additionally, they present many other useful properties, such as superelasticity, high force to volume ratio, high damping capacity, good chemical resistance and the typical qualities of metals like resistance, stiffness, workability, and so on. This combination enables their use as sensors and actuator in numerous fields[7] such as industrial applications,[8,9] microsystems,[10] automotive,[11] aeronautics,[12,13] biomedical,[14–16] robotics[17,18] and even in the textile industries.[19]

1.2 Martensitic Transformation

The main phenomena behind the conventional and magnetic shape memory effect is a phase transformation called the martensitic transformation. This process is a first order solid-solid phase transformation and takes place in a diffusion-less manner, as the atoms are moving less than the interatomic distances and retain their positions relative to each other. This implies that both phases must have the same composition. These materials exhibit two stable phases with different crystallographic structures & properties and a rigorous crystallographic connection between them. At high temperatures, they present a high symmetry phase (cubic) called austenite, whereas, at low temperatures, they turn to a lower symmetry phase termed martensite, which can have a tetragonal, orthorhombic or monoclinic crystal structure. The transformation occurs in a range of temperatures and has a thermal hysteresis associated. The area of the hysteresis is related with the energy dissipation processes in the crystal lattice. As observed in Figure 1.1 the transformation can be characterized by four transformation temperatures: T_{ms}, T_{mf}, T_{as}, and T_{af}. T_{ms} and T_{mf} indicate the temperatures, during cooling, at which the martensite starts and finish respectively to form; and T_{as} and T_{af} are the equivalent temperatures for the austenite formation during heating.

When transforming to the lower symmetry phase upon cooling, the transformation stresses are accommodated by twinning, resulting in the formation of twin variants. These variants can be defined as crystallographically equivalent structures, which differ in their orientation with respect to the material axes. The planes that

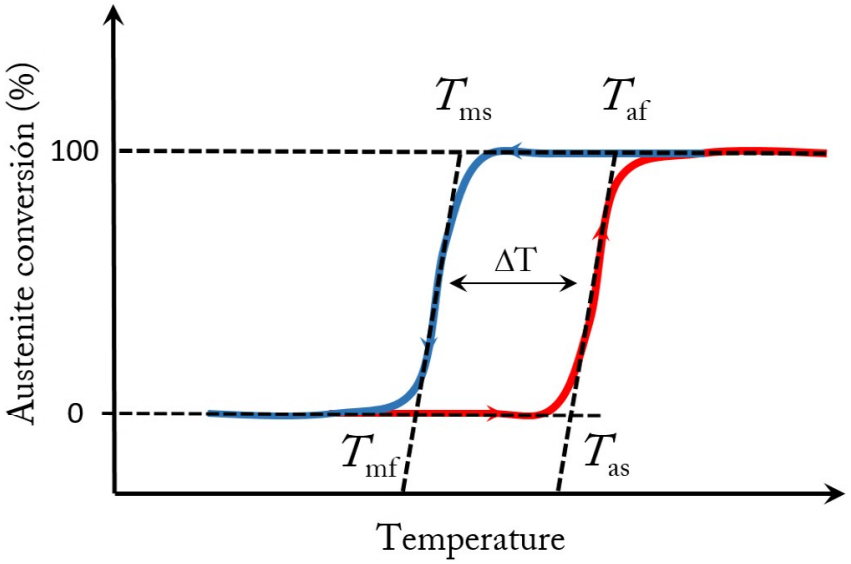

Figure 1.1: Thermal hysteresis loop of the martensitic transformation. Characteristics temperatures are indicated as T_{ms}, T_{mf}, T_{as}, and T_{af} according to the two-tangents method.

separate the adjacent variants are called twin boundaries. The crystal structure of the twin respect its adjacent twin is a mirror image (See Figure 1.2). Unless an external force is applied to the system, the distribution of these variants is random and no macroscopic effect is observed. Besides the thermally induced transformation, SMAs can also display stress-induced phase transformations. Above T_{af}, and in the presence of an applied load, the martensite starts to form with a preferential nucleation and growth of one of the variants. When the stress is released, the detwinned martensite becomes unstable, and the sample returns to the original high temperature arrangement. In this case, a macroscopic deformation is associated with the transformation. This effect to recover austenite by unloading is also known as superelasticity.

1.3 Shape Memory Effect

The shape memory effect is the ability to "remember" a previous form after a deformation. For the SMAs this phenomena is related to the martensitic transformation and occurs when a deformed martensite recovers the original shape when transforming to the austenite upon heating over T_{af}. The mechanism is schematically explained

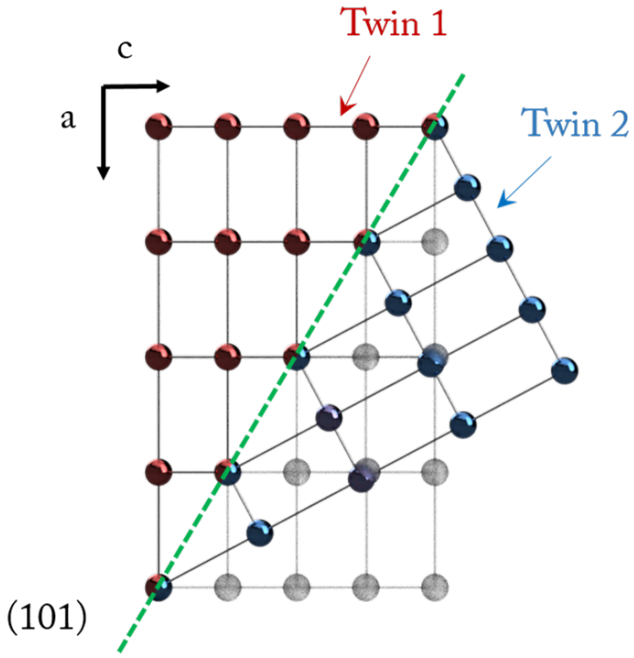

Figure 1.2: A two-dimensional schematic diagram of two adjacent tetragonal twin variants separated by a twin boundary (Green dashed line).

in Figure 1.3 by the stress-strain-temperature diagram.

Starting from the austenite and cooling down to the T_{mf}, a twinned martensite is formed, without any macroscopic change (1). From 1 to 2, a mechanical stress is applied, and the twinned martensite elastically deforms. At a certain stress (2), called twinning stress (σ_{TW}), the martensitic reorientation stars and at the end of the plateau, the de-twinned martensite is formed, with an associated macroscopic deformation (from 2 to 3). Further stress leads to an elastic deformation of the de-twinned martensite (4). Upon removing the applied stress, the macroscopic deformation is retained (5). Finally, the original parent phase is returned by heating above T_{af} (from 6 to 7). This effect is known as one-way shape memory effect, as the "remembered" phase is only the austenite. This behavior is an intrinsic characteristic of the SMA; however, a two-way shape memory effect could be also obtained by additional training. In the two-way shape memory effect, the material is able to remember two structures, the austenitic one at high temperature and the trained one in the martensite phase. In this case, the material is able to go between the two phases just by a temperature change, and on both, cooling and heating, a macroscopic deformation is observed. This property was commonly used for the design of

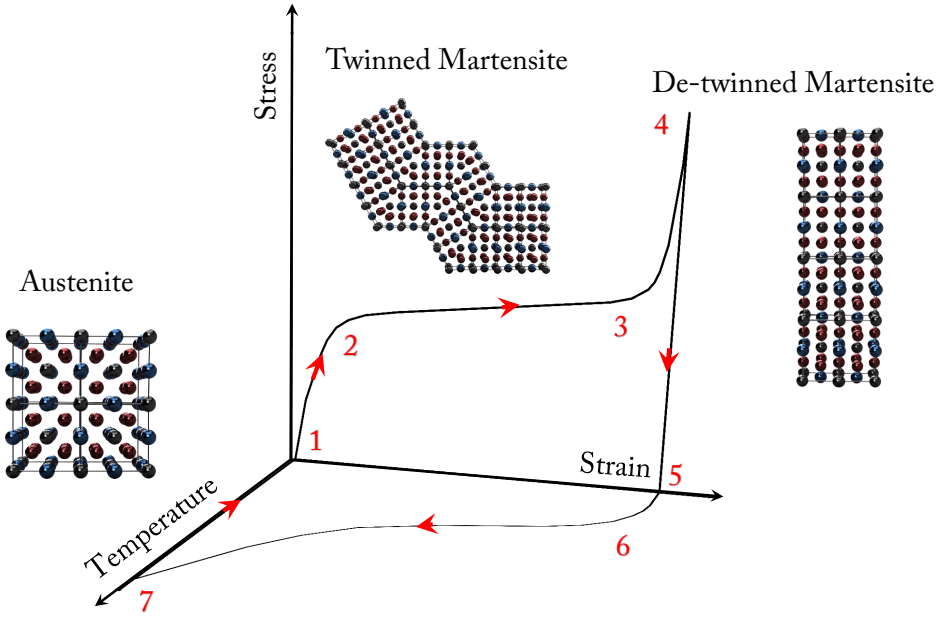

Figure 1.3: Shape memory effect and the corresponding structures presented in the different stages of the transformation.

actuators which can generate force or motion with a temperature change.

1.4 Magnetic Field Induced Strain

Ferromagnetic shape memory alloys (FSMAs) comprise an important group inside SMAs that also exhibit ferromagnetic behavior. These materials are able to exhibit magnetic field induce strains (MFIS) up to 12%.[20] The main phenomenon behind the MFIS is the magnetic field reorientation of the twin boundaries. The prototypical material for MSM applications is the Ni-Mn-Ga system, which has been the most studied among other ferromagnetic ones. This system was firstly studied in 1995.[21] One of the main characteristics of ferromagnetic materials is the presence of a nonzero spontaneous magnetization, even in the absence of a magnetic field. Ni–Mn–Ga alloys, additionally exhibit a strong magnetocrystalline anisotropy in the martensite, that couples the easy direction of magnetization to a crystallographic direction of the crystal. Thus, in a twinned martensite, different directions of magnetization are presented (See Figure 1.4).

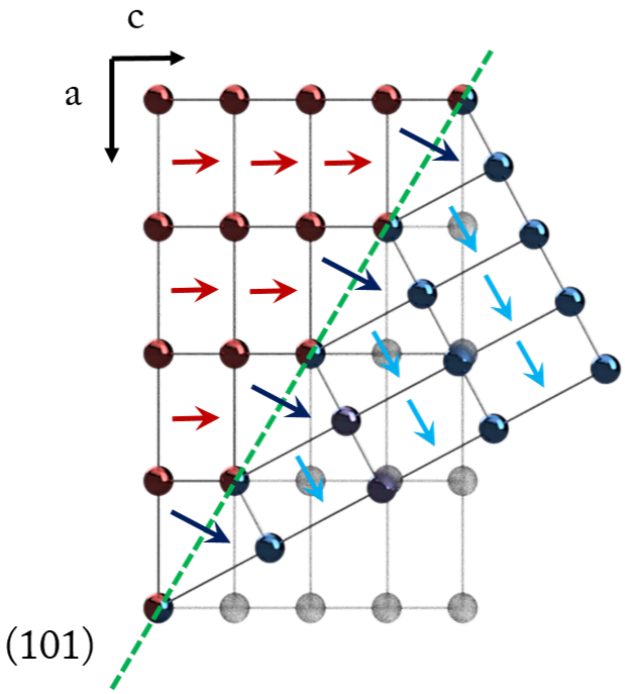

Figure 1.4: A two-dimensional schematic diagram of two tetragonal twin variants separated by a twin boundary (green dashed line) and the relative orientation of the magnetic moments.

Under an external magnetic field, the Zeeman Energy, which is expressed as:

$$E_{Zeeman} = -\mu_0 \vec{H} \cdot \vec{M}_s \tag{1.1}$$

where μ_0 is the magnetic permeability of free space, $\vec{H}$, the applied magnetic field and $\vec{M}_s$, the spontaneous magnetization; tends to rotate the magnetization in the direction of the external field.[22] On the other hand, the uniaxial magnetic anisotropy energy, described as:

$$E_{anisotropy} = K_u \cdot sin^2\theta \tag{1.2}$$

where K_u, is the anisotropy constant, and θ, the angle between the magnetization and the easy direction of magnetization; opposses the magnetization to move out of the easy direction.[23] In the framework of a simplified model, Figure 1.5, when applying an external magnetic field, a stress due to the Zeeman energy is generated on the twin boundaries, and, if the magnetocrystalline anisotropy is strong enough, the

reorientation of the variants will be more favorable than the rotation of the magnetic moments. Therefore, the variants with the magnetic moments in the direction of the applied field will grow at expenses to the others until a single variant state, with an associated strain, will be reached. This process is reversible and could be induced either by applying an orthogonal field or a mechanical stress. Figure 1.5 shows a schematic of the entire process.

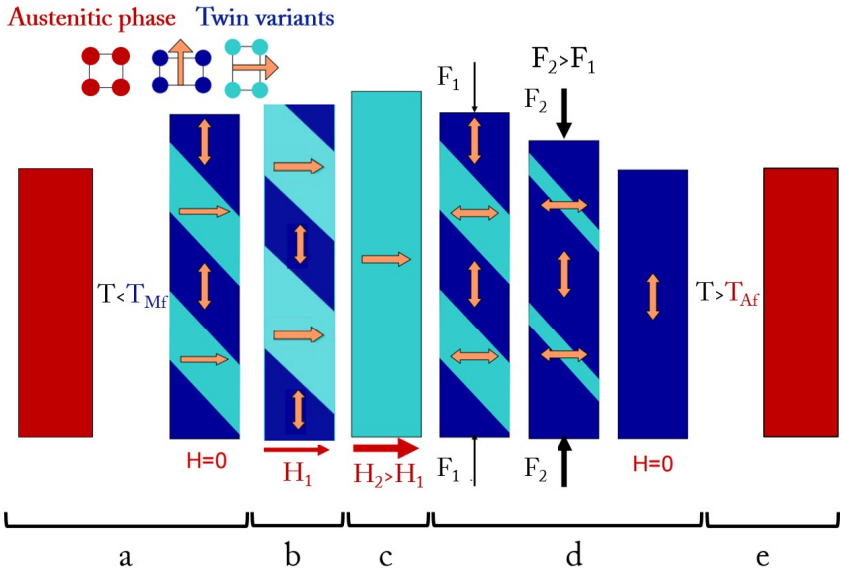

Figure 1.5: Schematic of the process of magnetic field induced strain and subsequent mechanical reset of the sample in a ferromagnetic shape memory alloy. a) The sample is first cooled from the austenite to a self-accommodated martensite phase without applying any magnetic field. The twin variants show different structural orientation and consequently different orientation of the magnetic moments (indicated by the yellow arrows). b) When applying a magnetic field the variant with the magnetic moments along the field grows at the expense of the other. c) By increasing the magnetic field, the full reorientation of the martensite variants occurs and a single variant representing also a single magnetic domain state of the sample is reached, resulting in a macroscopic deformation. d) Inverse process until the former single variant state is induced either by magnetic or mechanical stress. e) Further heating recovers the initial shape in the austenite phase.

Nevertheless, the possibility to obtain large magnetic induced deformations is conditioned to several materials properties. Firstly, a low symmetry martensite structure at the working temperature is needed. Additionally, the crystallographic relation between the cell parameters, c/a, of the martensite structure, has a huge

influence as it determines the maximum theoretical deformation achievable, ϵ_{max}. A detailed analysis of this relation for the different types of martensite structures will be discussed in the next section. A second requirement is the presence of highly mobile twin boundaries, which means, twinning stresses below 1-2 MPa. This twinning stress determines the minimum stress that must be overcome by the magnetic field, which produces magnetostress, to induce the twin boundaries' movement. At the same time, the value of magnetostress, reached in the magnetically saturated state, is also related to the c/a[1,24,25] and the uniaxial magnetic anisotropy constant, K_u,[26–28] of the martensite as:

$$\sigma_{mag} = (1 - a/c)^{-1} K_u \tag{1.3}$$

Therefore, the crystal structure of the martensite affects both the twinning and the magnetic stresses, and determines the maximum strain attainable.

1.5 The Ni–Mn–Ga system: Physical properties

The Ni–Mn–Ga alloy system is an intermetallic compound that displays a Heusler structure.[29] The austenite phase exhibits a Fm-3m symmetry with a $L2_1$ chemical ordering. This structure is composed by four interpenetrating fcc sublattices, each one with four atoms in the positions, A (000), B ($\frac{1}{4}\frac{1}{4}\frac{1}{4}$), C ($\frac{1}{2}\frac{1}{2}\frac{1}{2}$) and D ($\frac{3}{4}\frac{3}{4}\frac{3}{4}$).

For the stoichiometric composition, Ni_2MnGa, the Ni atoms occupy the B and D positions while Mn and Ga the A and C respectively. At temperatures above approximately 1073 K Mn and Ga become disordered, transforming to a B2 structure with a Pm-3m symmetry.

At low temperatures, the martensitic transformation occurs whereby the cubic phase turns to a low symmetry one. Usually, the martensite phase is described as a tetragonal phase with an I4/mmm symmetry. This structure is also known as non-modulated martensite. This unit cell is related to the parent phase by a 45° rotation around the (001) axis as described in Figure 1.6. The relation between the lattice parameters of both phases is described by $\frac{\sqrt{2}}{2}a = a'$, being a' the lattice parameter of the martensite and a the one of the parent phase.

The martensite phase can be also described as a fcc lattice, similar to the austenite one. In this case the relation between both phases consists of a contraction of the c-axis accompanied by the elongation of the two remaining axis.

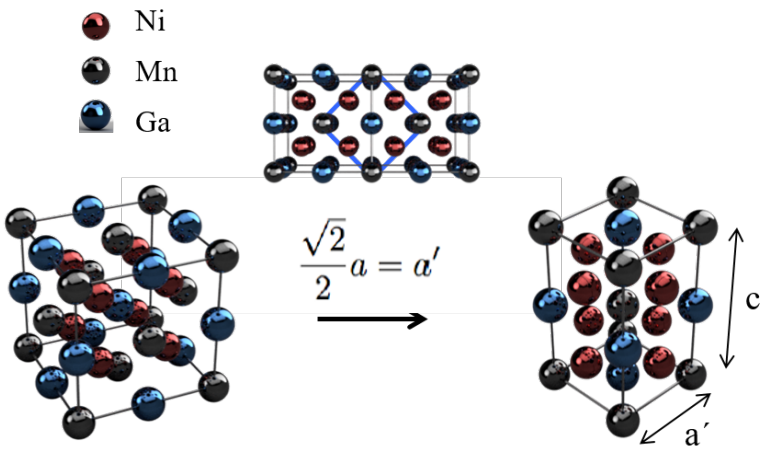

Figure 1.6: Unit cell of the austenite (left) and martensite (right) structures. The middle figure shows the relation between both structures by a 45° rotation around the (001) axis.

The high c/a value of the tetragonal lattice they exhibit allow to achieve large values of macroscopic deformations up to 20%. Normally, high values of c/a are associated with high values of twinning stresses preventing large MFIS. Recently, by a reduction of c/a a MFIS of 12% was observed in a non-modulated Ni–Mn–Ga based martensite.[30]

It is worth noting that in off-stoichiometric compositions different martensite structures, other than non-modulated tetragonal one, have been also found. The most commonly ones are the 5M and 7M structures. These structures can be described as monoclinic cells with different distortion degree and exhibiting lattice modulations.

The 5M martensite can be explained as a contraction along one of the <100> directions of the cubic phase, leading to a relatively strong deformation (c/a $\approx$ 0.94). This structure can be considered as close to the tetragonal one, however, the martensite lattice shows a periodic shuffling along the (110)[1-10] system, with a modulation period of five (110) planes. Generally, the alloys with this structure present enough low twinning stresses to exhibit MFIS,[31,32] and maximum deformations up to 6%.[33,34]

In the case of the 7M, the structure has been generally described in terms of an orthorhombic structure, exhibitig atomic shuffling with a periodicity of seven (110)

planes. Like in the 5M, the twinning stress in the 7M samples is usually very small, which enables the MFIS.[35,36] The maximum magnetic field induced deformation achievable in 7M martensites is $\approx 10\%$.[33,34]

1.6 High temperature shape memory alloys

Shape memory alloys actuating at high temperatures offer a simplification and an advance on the operating efficiency of mechanical devices for robotic, energy conversion, automotive applications, MEMS, and aerospace technologies.[37,38] The demands of these technologies, actually require SMAs with actuation temperatures above 373 K. Such a high value is difficult to reach in the case of FSMAs because both magnetic properties and martensitic transformation must be appropriated at elevated temperatures.

The practical implementation of high temperature shape memory alloys in devices is still under development due to a number of unresolved issues, such as thermal and thermomechanical stability, martensite stabilization, decomposition, high twinning stresses, etc.[39]

Due to the aforementioned still unresolved challenges, nowadays high temperature SMAs and FSMAs remain a relatively unexplored terrain. So far, the limit temperature at which the actuation of Ni–Mn–Ga alloys has been demonstrated still stands around 353 K[31] for ferromagnetic SMAs, which is well below typically demanded actuation temperatures in most industries. In the case of conventional SMAs, high actuation temperatures around 670-730 K have been already achieved;[37] however, the thermal and thermomechanical instabilities that they present have hindered their possible implementation in technology as high temperature sensors and/or actuators.

1.7 Objectives and structure of the Thesis

Following the discussion presented in the previous sections of this chapter, the main goal of the present thesis consists in the design and study of new conventional and ferromagnetic shape memory alloys with increased temperature actuation ranges, with the ultimate goal to be used as high temperature sensors and actuators in the near future. Through a better understanding of the composition effect and the correlation between the structure and the magnetic properties in SMAs, it is expected

that the work developed and presented in this thesis will directly impact the optimal implementation and practical performance of high temperature shape memory alloys in the automotive and space technologies.

The Thesis is structured in the following chapters:

Chapter 2 details a systematic exploration of different Ni–Mn–Ga alloys composition exhibiting martensitic transformations higher than 670 K and a stable recoverable actuation strain of 4 %. The mechanisms leading to the thermal and thermo-mechanical stability of these alloys and the effect of thermal treatments on these properties are disclosed. These studies have been performed on poly and single crystalline samples.

Chapter 3 focuses on the systematic study of polycrystalline multicomponent Ni–Mn–Ga–Fe–Co–Cu series, which have never been explored before. The effect of Fe and Cu addition on the martensitic transformation, structure and magnetic properties is discussed.

A deep study on the structure, chemical order and magnetic properties of the Fe series presented in the previous chapter is described in Chapter 4. The analysis of the chemical order and the magnetic moment distribution is performed by unpolarized and polarized neutron diffraction techniques. This study reveals the strong influence of the chemical order and the Mn–Mn interatomic distances on the magnetism of the alloys.

Finally, Chapter 5 centers around the functional properties of three Ni–Mn–Ga–Fe–Co–Cu single crystals. These compositions were chosen based on the results in Chapter 3. The most relevant parameters for magnetic field induced strain, such as twinning stress, magnetic anisotropy, and magnetostress, are analyzed as a function of the temperature and the evolution of the crystal structure.

Chapter 6 summarizes the conclusions from the previous chapters and suggests future work on the topic.

Finally, some experimental details and aspects are described in the appendix.

Chapter 2

High Temperature Shape Memory Alloys: Ni-Mn-Ga

2.1 Introduction

A growing interest has recently arisen in the development of High Temperature Shape Memory Alloys (HTSMAs), that can work at temperatures up to 820 K, in response to the demands from high-tech areas such as automotive or aerospace industries.[37,40] Ni-Mn-Ga alloys have been widely studied as magnetic and non-magnetic shape memory materials[20,41] and also they are good candidates for HTSMA. The high sensitivity of their properties with the composition makes them easily tunable materials,[42–44] which can exhibit high-temperature, low-hysteresis thermoelastic martensitic transformations, with a recoverable strain of over 9%,[45] and a good compressive and tensile superelastic behavior.[46,47] These properties combined in one alloy would make them real candidates for these applications.
Conventional systems, such as FeMnSi–, CuAlNi–, NiMn–, NiTi–,TiTa– etc;[48–51] already exhibit high transformation temperature, however, there is still no real breakthrough in their capabilities for real applications. The martensite stabilization and the thermal and thermo-mechanical stability of these systems constitute the main issues to be addressed in order to achieve good candidates for high temperature technologies.[52–54] Thus, a study of these aspects in a highly promising system for high temperature applications like Ni–Mn–Ga constitutes an important topic nowadays.

In this chapter, different compositions of Ni-Mn-Ga alloys are explored with the aim of elaborateing Ni-Mn-Ga HTSMAs with martensitic transformations temper-

atures (T_M) higher than 670 K and a stable recoverable actuation strain of 4 %. The mechanisms leading to the cycling stability (thermal and thermo-mechanical) in single- and polycrystalline forms of these alloys and the effect of thermal treatments on these properties are analyzed.

2.2 Experimental details

The Ni-Mn-Ga polycrystalline samples used in this study were produced in-house by melting the pure elements in an Indurect Compact Reitel induction furnace (at the University of Basque Country) under argon atmosphere. The samples were prepared from high purity elements (Alfa-Aesar Gallium 99.999%, Nickel 99.95%, and Manganese 99.95%). First, the pure elements were cleaned. In the case of Ga and Ni this consisted in cleaning with acetone and isopropanol in an ultrasonic bath to remove any organic traces and moisture before melting. In the case of Mn, the pieces were first cleaned with a nitric acid solution (5%) for approximately 1 min to remove the surface oxide, then rinsed with deionized water to remove the traces from the acid solution and finally with acetone and isopropanol as the former elements.

The elements were weighed according to the desired composition considering a maximum alloy weight of 20 g. The Mn and Ga were wrapped in Ni foil and placed, together with the Ni pieces, into a mullite crucible coated with Zirconium Oxide. This coating is used to avoid the reaction between the Mn and the crucible. The crucible was then placed inside the induction furnace. The furnace chamber was evacuated and refilled five times with Ar + H (5%) to ensure a reductive atmosphere. The melts were then cast into rods in a copper mold, with a cavity of 4 mm in diameter by 30 mm long .

Single crystals were grown from the polycrystalline rods by the floating zone method in an optical FZ-T-P1200-H-I-S furnace (Crystal System Corp) at the Basque Center of Materials, applications and nanostructures (BCMaterials). For the growth, an oriented seed was used to control the final orientation of the crystals. The samples were grown at 10 mm/h rate. Both the seed and supply material were rotated at 8 RPMs in a controlled atmosphere of 5% by volume Hydrogen in Argon gas (Air Liquide, Alphagaz 2 grade) with a constant flow of 3 standard liters per minute at an overpressure of 0.35 MPa. To avoid thermal shock, and to allow surface contaminants to evaporate before growth, the sample temperature was raised from room

temperature to the melting point in approximately 30 minutes.

All the samples were heat–treated after the melting or the growth during 24 h at 1223 K to homogenize the composition and 4 h at 723 K to allow the $L2_1$ chemical ordering. The heat treatment was done by wrapping the cut single and polycrystalline samples in Tungsten foil to avoid contact between the sample and ampule. The sample was then inserted into a quartz ampule with Tantalum foil as a non-evaporative Oxygen getter. The ampules were evacuated and then back-filled with high purity Argon gas to 1 bar to prevent the evaporation of Manganese from the alloy.

The compositions studied were selected as the ones with the highest martensitic transformation temperatures (see Table 2.1). In the Ni-Mn-Ga isothermal ternary phase diagram, three different phases can be observed: β (B2-ordered body-centered cubic (bcc)), γ (Ni-rich and Ga-depleted disordered face-centered cubic (fcc)) and $\beta + \gamma$ dual phase regions.[55] According to the phase diagram, (Figure 2.1), two groups of phase states were selected. On the one hand, a room-temperature non-modulated tetragonal martensite (2M), formed from a single β phase; and on the other hand a room temperature mixture of 2M martensite and precipitates of the non-transforming γ phase formed from a dual $\beta + \gamma$ phase structure.

The composition of all the samples was measured by EDX using a Bruker Quantax 70 detector in a Hitachi TM3000 Scanning Electron Microscope. The measurement was performed in three different parts of the sample and the resulted composition is an average of the different measurements. These results are summarized in Table 2.1.

The structural characterization of the samples was performed by X–ray diffraction, XRD, with a Philips X'Pert, MPD diffractometer with CuK_α radiation, at the Advanced Research Facilities (SGIker) of the University of the Basque Country.

The transformation temperatures of the samples studied were determined by a PerkinElmer Diamond Differential Scanning Calorimetry, DSC, at BCMaterials. The T_M temperatures are in Table 2.1. The thermal cycling stability under no load on the polycrystalline samples was probed by DSC using heating rates of 100 K/min in a temperature range which covers the full transformation range.

Magnetization measurements to determine the Curie Tempereture were performed in an in-house made vibrating sample magnetometer, VSM, at the University of Basque Country.

Table 2.1: Compositions of the as cast polycrystalline alloys (P1 – P4) and the as-grown single crystals (SC2 and SC3), martensitic start and austenitic finish temperatures, as well as their phase content at 773 K according to equilibrium diagram in Figure 2.1.

Sample	Composition (at%)	T_{af}(K)	T_{ms}(K)	Phase
P1	$Ni_{57.1}Mn_{26.5}Ga_{16.4}$	779	720	$\beta+\gamma$
P2	$Ni_{53.3}Mn_{30.7}Ga_{16}$	647	621	β
P3	$Ni_{56.9}Mn_{27.8}Ga_{15.3}$	781	724	$\beta+\gamma$
P4	$Ni_{57.6}Mn_{26.8}Ga_{15.6}$	776	689	$\beta+\gamma$
SC2	$Ni_{57.2}Mn_{23.5}Ga_{19.3}$	707	654	$\beta+\gamma$
SC3	$Ni_{56.4}Mn_{24.8}Ga_{18.8}$	788	736	β

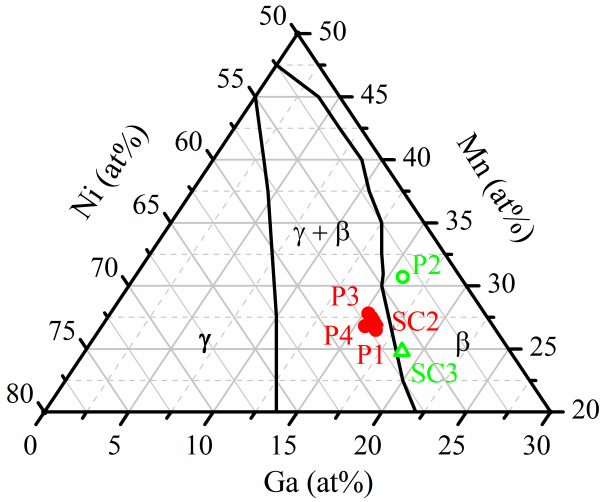

Figure 2.1: An isothermal section of the equilibrium Ni-Mn-Ga diagram at 773 K according to Ref.,[53] where the compositions of the studied alloys are indicated. Single crystals (SC) and polycrystalline alloys (P) are marked by the open triangles and open circles, respectively, when they belong to β phase zone; and by the full triangles and full circles, respectively, when they belong to a dual β + γ) phase region.

The dynamic mechanical analyzer, DMA, was employed to study the thermo-mechanical behavior of the two single crystals presented in this chapter. The equipment used was a Mettler Toledo DMA 1 located at BCMaterials. Two different regimes were used, dynamic and quasi-static ones (See Appendix B for the experimental details). As we were limited by the DMA to a maximal applicable force of 10 N, the samples' cross-sections were reduced to achieve the maximum possible

stress. Thus, prior to the cycling, rectangular samples with all 100-type faces, measuring approximately 0.6 x 0.6 x 20 mm, were cut by low speed saw with the long dimension approximately parallel to the boule axis. The rectangular prisms were then hand polished starting with 600 grit sandpaper followed by 800, 1200, 2400 and finally 4000 grit metallographic sandpaper from Struers until a mirror finish on the surfaces was achieved. Mechanical polishing was followed by electro polishing to remove the surface layer that might have been stressed during the mechanical polishing. The cathode was made from W.N. 1.4310 stainless steel (AISI 301 equivalent). The electrolyte used was 20 volume parts of ethanol (Panreac 96% v/v) to 1 part concentrated nitric acid (Alfa Aesar 67%) cooled in an ice-ethanol bath to -10 °C. The sample was placed approximately 5 mm from the cathode and a voltage of 9 V was applied during 30 seconds. The procedure was repeated four times, each time having one of the 0.6 x 15 mm faces parallel to the cathode.

2.3 Functional stability of the polycrystalline alloys

The martensitic trasformation temperatures play an important role while utilizing these materials in devices which require specific actuation ranges and stability. The determination of these temperatures and the evaluation of their stability during service life time is important from an application point of view.

Polycrystalline materials were selected for this study due to their ease of production in comparison to single crystals and to the possibility of reproducing specific compositions with a high accuracy.

The compositions studied were chosen with the aim of obtaining HTSMA, thus, three of the four alloys present transformation temperatures over 773 K, as observed in Table 2.1. The fourth sample, P2, even though it exhibits lower transformation temperatures, was selected as a representative sample of the β phase region.

2.3.1 Thermal behavior in the β region

Sample P2 was subjected to 300 heating-cooling DSC cycles in order to evaluate its thermal behavior. The 300 cycles were divided into three parts, each one of 100 cycles at a heating rate of 100 K/min. Every 100 cycles an additional cycle was performed at 20 K/min as a control. Figure 2.2 represents the heat flow variation as a function of the temperature. The blue curves correspond to the 1^{st} 100 cycles and the red and black ones to the 2^{nd} and 3^{rd} 100 cycles respectively. Two broad

peaks are observed on the DSC curves. An endothermic peak (up) which corresponds to the reverse transformation from martensite to austenite during heating; and an exothermic one (down), that belongs to the fordware transformation during cooling. The temperature shift between them is due to the thermal hysteresis associated with the transformation.

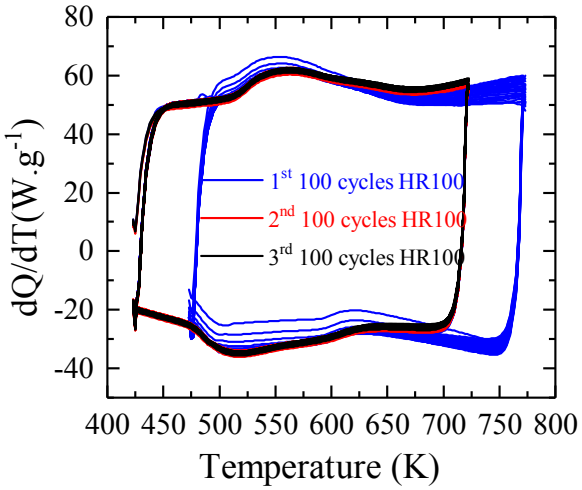

Figure 2.2: Evolution of the DSC cycling of the sample P2, showing the first 100 cycles in blue, the second 100 cycles in red and the last 100 cycles in black.

Figure 2.2 shows that the transformation peaks remain unchanged in shape and temperature range as the cycling progresses. This behavior indicates that the composition remains constant during all the proccess and there is no indication of a second phase precipitation, which is consistent with the expected nature of a pure β phase.

X–ray diffraction analysis was performed to determine the crystallographic structure and explore the possible structural changes through the cycling. The measurements were carried out in a two–θ range from 30 to 90°.

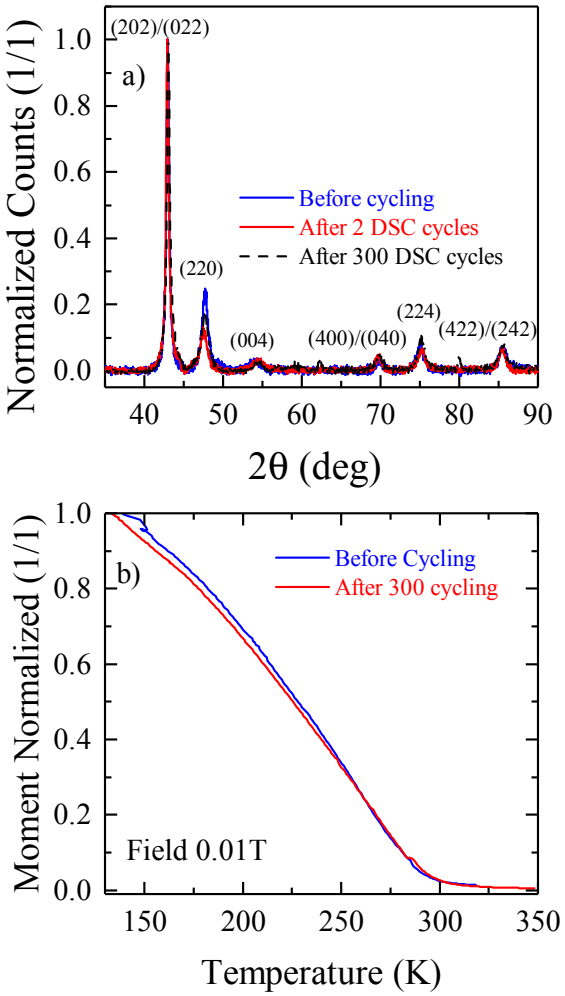

Figure 2.3: a) Diffraction patterns measured at room temperature for the P2 sample as cast, and after 2 and 300 cycles. b) Magnetization versus temperature measurements at 0.01 T before and after cycling.

Figure 2.3 (a) shows the room temperature diffraction patterns of the sample as cast (blue) and after 2 (red) and 300 cycles (black). All the reflections observed in the three measurements correspond to a body centered tetragonal phase and belong to the non-modulated martensite structure. For an easier comparison the hkl indexes correspond to the cubic phase structure. The symmetry and cell parameters of the sample were determined to be a I4/mmm symmetry with a = b = 3.815 Å and c = 6.760 Å. The presence of any additional phases would be identified by the appearence of extra reflections, which are not observed in the diffractograms. This fact, together

with the stable position of the existent reflections all along the cycling, bears out the good thermal stability of the alloy.

The strong sensitivity that Ni–Mn–Ga alloys exhibit between the properties and the composition, opens different ways to detect possible changes in the material. One of this properties is the Curie temperature, T_C. Even though, T_C is not a critical parameter for HTSMA applications, a change in the composition and consequently in the structure will have an influence on it.

Low-field magnetization measurements (0.01 T) as a function of the temperature were performed for the sample in as cast state (blue) and after 300 DSC cyles (red). The results are shown in Figure 2.3 for a temperature range from 140 to 350 K. A rapid increase of the magnetization with the temperature lowering, which corresponds to the T_C of the martensite, is observed at about 290 K. Above T_C, the material is paramagnetic. At higher temperatures the material transforms into the paramagnetic austenitic phase. Similar behavior is obtained for both curves without any temperature shift indicating that there is no change in the alloy composition before and after cycling. These results are consistent with the ones obtained by DSC and XRD.

2.3.2 Thermal behavior in the $\beta + \gamma$ region

As shown in Table 2.1, three polycrystalline samples, labeled as P1, P3, and P4, belong to the $\beta + \gamma$ region. The composition of the alloy P1 was designed, by modifying the Mn/Ga ratio, to obtain an alloy with high T_M falling in the two phase region of the ternary phase diagram. The samples P3 and P4 were selected by substituting in P1 Ga by Mn and Ni, respectively, in order to increase the T_M.

All the samples were subjected to 300 DSC cycles, as described in the previous section. Samples P1, P3 and P4 present similar behavior so only the results for P1 are shown as representative. Figure 2.4 depicts the heat flow as a function of the temperature for the sample P1. The blue curve corresponds to the 1^{st} 100 cycles and the red and black ones to the 2^{nd} and 3^{rd} ones respectively.

Contrary to what was observed for P2, (See Figure 2.2) the transformation peaks are initially narrow and well defined, but over the course of cycling, they become broader and less intense. There is a drop of the transformation temperature from approximately 773 K to 648 K. During the first 100 cycles the degradation process is quite drastic, however, it gradually begins to stabilize. This effect is related to the step-wise precipitation of the γ phase, as expected from their dual phase nature.

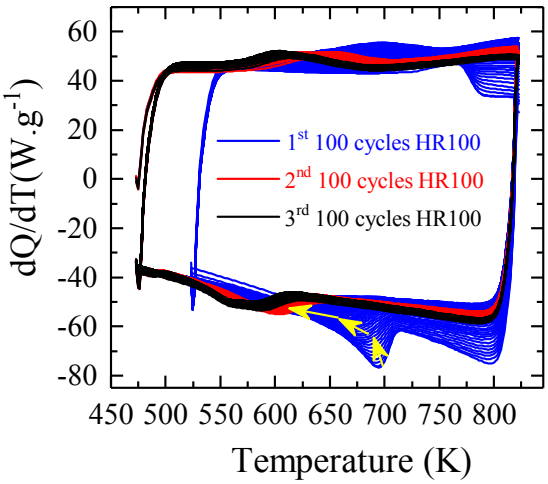

Figure 2.4: Evolution of the DSC curves of the sample P1, showing the first 100 cycles in blue, the second 100 cycles in red and the last 100 cycles in black. Yellow arrows show the direction of transformation shift.

The decrease of the peak intensity is directly correlated with the reduction of the volume fraction transformed, and, the temperature shift, is related to a change in the matrix composition, both, effects of the γ phase appearance.

Evidence of γ phase is also obtained from XRD and VSM analysis. The room temperature diffraction patterns were obtained for the samples P1, P3, and P4, in as cast state and after 2, and 300 cycles.

Figure 2.5 (a) shows the diffraction patterns of P1 as representative of the three alloys. The blue pattern belongs to the sample as cast, and the red and black ones correspond to the samples after 2 and 300 cycles respectivey. In this case, additional reflections at 49.5 ° and 88 ° in the two-θ range appear with the cycling. These reflections correspond to the (200) and (311) reflections of the cubic γ phase. The rest of the reflections belong to the non-modulated tetragonal martensite. Inset to figure 2.5 (a) shows a slight shift of the (220) reflection to higher angles, indicating a reduction of the a lattice parameter with the cycling.

The symmetry and the cell parameters of the martensite and the γ phase after cycling were also calculated from the room temperature diffractograms of the three samples. The results are summarized in Table 2.2.

The low-field magnetization as a function of temperature is depicted in Figure 2.5 (b). The curves show the results for the sample before cycling, in blue, and after

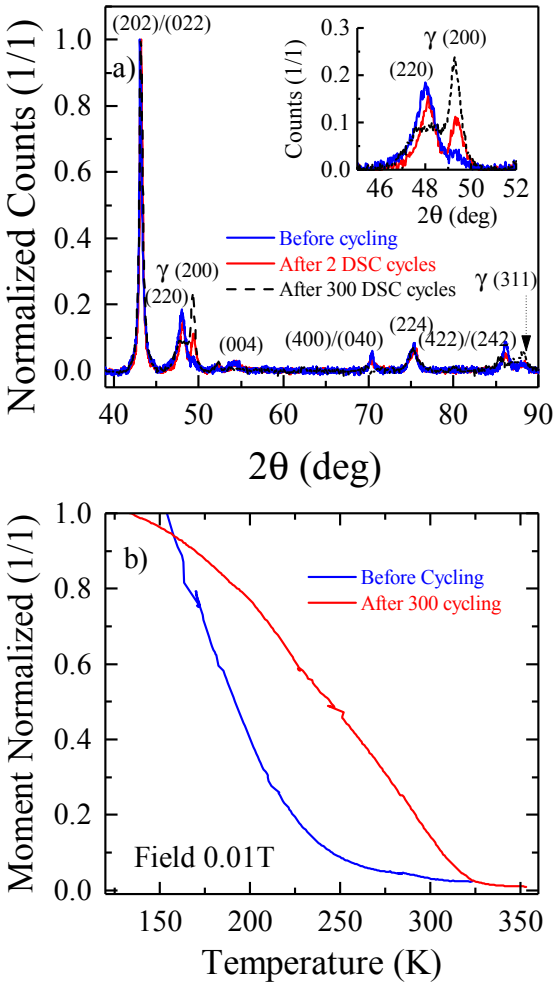

Figure 2.5: a) Diffraction patterns measured at room temperature for the P1 sample as cast, and after 2 and 300 cycles. The inset is an increment of the (220) and γ(200) reflections showing the increase of the last. b) Magnetization versus temperature measurements at 0.01 T before and after cycling.

300 cycles, in red. The shift of $T_C \approx 70$ K to higher temperatures is obtained for the sample after cycling. As discussed in the previous section, this shift is directly correlated with a change in the composition and the structure. Additionally, the slope of the T_C also decreases, which means that the sample could exhibit a composition gradient.

The presence of a second phase has been already corroborated by XRD mea-

Table 2.2: Cell parameters measured at room temperature for the samples P1, P3 and P4 after 300 cycles

Sample	Phase	Symmetry	Cell parameters
P1	$L1_0$	I4/mmm	a = b = 3.798 Å c = 6.770 Å
	Gamma	Fm-3m	c = 3.709 Å
P3	$L1_0$	I4/mmm	a = b = 3.789 Å c = 6.748 Å
	Gamma	Fm-3m	c = 3.714 Å
P4	$L1_0$	I4/mmm	a = b = 3.789 Å c = 6.768 Å
	Gamma	Fm-3m	c = 3.707 Å

surements, however, the size and distribution of this phase in the material are also important to understand their influence on the properties. Thus, SEM micrographs were obtained after the full cycling for the sample P1 (See Figure 2.6). From this figure, it is clearly seen that the alloy is constituted by two phases, a twinned martensite, which comprise the matrix of the alloy, and a gamma phase, indicated by a yellow arrow, forming precipitates along the grain boundaries. In the matrix the differently oriented twin variants can be distinguished by light and dark grey colors. The average size of the precipitates is of the order of micrometers. Some of the precipitates observed in the micrograph exhibit traces of twin boundaries, which suggests the formation of intermediate structures between the non-modulated martensite, and the cubic γ precipitates.

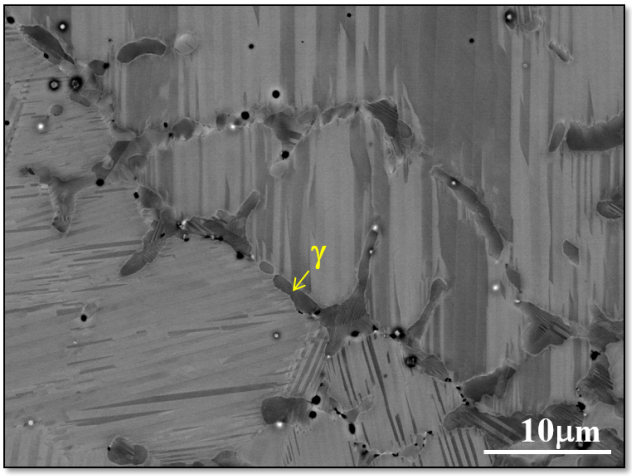

Figure 2.6: SEM micrograph showing the presence of γ phase on the grain boundaries of the P1 alloy after 300 DSC cycles.

Additionally, EDX measurements were performed using SGIker's shared SEM facility in both, precipitates and matrix to determine the composition difference. The resulting compositions are $Ni_{55.1}Mn_{26.3}Ga_{18.6}$ for the matrix and $Ni_{61.2}Mn_{27.2}Ga_{11.6}$ for the gamma precipitates.

2.4 Functional stability of the single crystals

For the evaluation of the thermo-mechanical cycling stability, single crystal samples were taken as representative materials of the intrinsic behavior due to the lack of grain boundaries. Two single crystals with different composition, SC2 and SC3, falling in the two different regions and exhibiting T_{af} over 700 K were selected for this study. To obtain reliable behavior, the quality and homogeneity of the single crystals produced became critical parameters.

To exemplify the single crystal growth let us consider the simplest case of a binary A-B system (See Figure 2.7). The alloy melt with an initial composition is cooled down to allow the solidification, when it reaches the red line, two different phases coexist, a liquid solution with L_1 composition and a solid one with composition S_1, which corresponds to the bottom part of the single crystal. With further cooling, the composition of the liquid and the solid solution becomes L_2 and S_2 and at lower temperatures L_3 and S_3, which corresponds to the upper part of the crystal. Thus, a composition gradient is expected along the crystal. In the case of Ni-Mn-Ga, the higher solubility of Mn in the liquid than in the solid, results in an enrichment of the crystal with Mn as the growth progresses. Schlagel et al.[56] suggested that convection also plays an important role in the composition gradient, altering the liquid composition through convective fluid flow.

Therefore, in order to minimize this effect, the temperature gradient of the melted zone must be as small as possible, and convection in this zone must be ensured. The floating melting zone was selected as the growth method for the single crystals as it presents small temperature gradients and guarantees the convection flow by the rotation of both, seed and sample in opposite directions during the full growth process.

To verify the homogeneity of the crystals produced, EDX analyses were performed along the crystal length. A small flat surface was grooved into the crystal to measure the composition distribution. The position corresponds to the measurement spot on

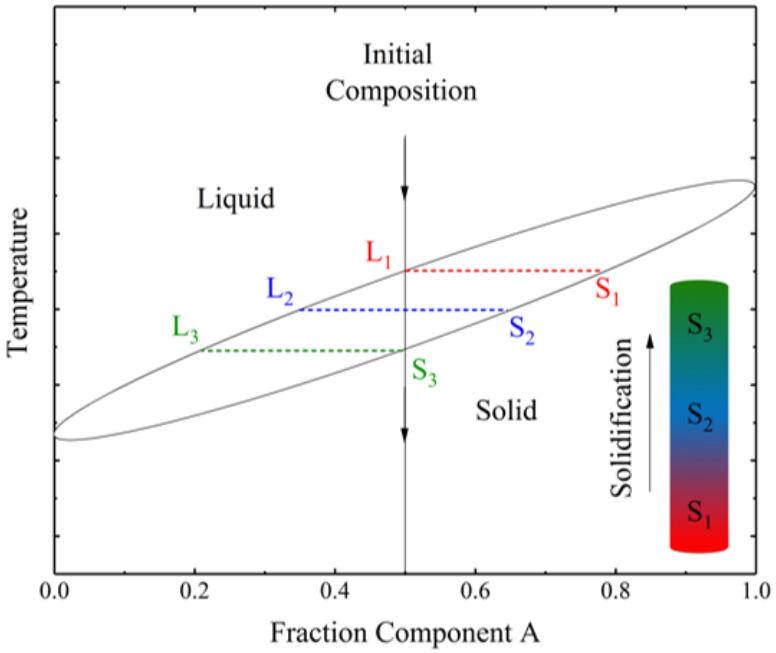

Figure 2.7: Schematic figure of a binary phase diagram at a constant pressure showing the composition evolution of the liquid and solid solutions during a cooling process.

the sample, the measurement spots were roughly evenly spaced along the sample length ($\approx$ 30 mm) from the bottom to the top. As can be seen, the composition is quite homogenous, to the point that, the difference between the value at each point and the average falls within the error bars (Figure 2.8), although a small tendency of less than a 1% of Mn increase (Ga decreas) is observed along the bar by the fitting lines.

The crystallographic orientation of the crystals was attempted to be determined by the Laue method using a molybdenum source, but due to the similarity of the Ni, Mn and Ga atomic x-ray scattering factors not enough difraction spots were obtained to ensure the proper orientation.

2.4.1 Thermo-mechanical behavior in the $\beta + \gamma$ region

Two different pieces were cut from the middle part of the crystal SC2. One of the pieces was measured in as grown state and the other one after heat treatment, to

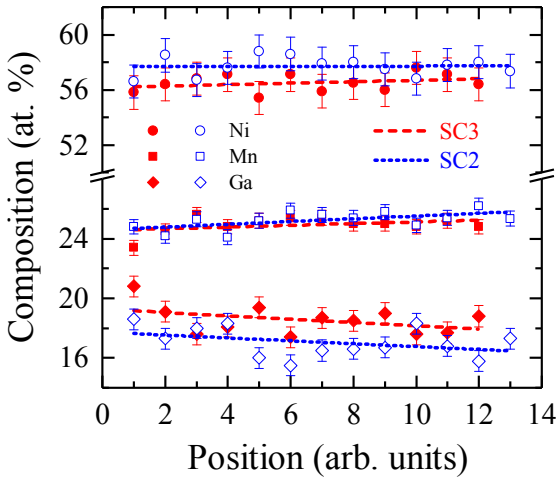

Figure 2.8: EDX measurements of the as-grown samples SC3 (blue) and SC2 (red). Composition measurements were taken at roughly evenly spaced points along the length of the sample (≈ 30 mm).

evaluate the effect of thermal treatments on the thermo-mechanical properties. The details of the heat treatment performed and the sample preparation were discussed before in the experimental section. The samples were long prisms with dimensions of 0.71 x 0.75 x 21.0 mm^3 for the as grown and 0.43 x 0.62 x 21.4 mm^3 for the heat-treated samples.
Beforehand, the characterization of the transformation temperatures was performed, and it is summarized in Table 2.1.

For the thermo-mechanical testing, the DMA technique was selected as it allows to measure in both, a quasi static mode, in which a constant force is applied in a temperature range, and a dynamic one where the sample is subjected to a sinusoidal deformation at a constant frequency during temperature variation. Both kind of measurements were done in tensile mode. Further details of this technique are discussed in Appendix B.

The experimental conditions used for the thermo-mechanical cycling under load for the samples in as grown state and heat-treated are specified in Table 2.3 and 2.4. The heating/cooling rate used was 20 K/min. The studied interval was adjusted during the measurement to ensure that the transformation temperatures were within the measurement range. As observed in Table 2.4, the load was chosen to 5 N to

keep the stress close to 20 MPa for the as-grown sample. A complete description of the method used is included in Appendix B.

Table 2.3: Experimental conditions for the static load thermal cycling of the as-grown SC2 sample.

Measurement	N° of cycles	Load (N)	Lenth (mm)	T_{Max} (K)	T_{Min} (K)
1st	5	10	10	723	473
2nd	50	10	10	723	473
3rd	50	10	10	723	473
4th	60	10	10	723	473
5th	50	10	10	723	473
6th	55	10	10	723	473
7th	65	10	10	723	473

Table 2.4: Experimental conditions for static load thermal cycling sample of SC2 after the heat treatment.

Measurement	N° of cycles	Load (N)	Lenth (mm)	T_{Max} (K)	T_{Min} (K)
1st	5	10	10	723	473
2nd	60	5	10	723	473
3rd	50	5	10	773	523
4th	50	5	10	773	523
5th	60	5	10	693	453
6th	55	5	10	693	453
7th	60	5	10	693	453

As expected from its dual phase nature, both two SC2 samples show a degradation process, however, despite being identical in composition and crystallographic orientation two clear distinct behaviors can be observed.

Figure 2.9 shows selected strain versus temperature cycles for the SC2 sample as grown (a) and heat-treated (b). The cycles show the behavior of the material during the transformation, when applying a constant force. At high temperatures, the austenite phase does not allow large deformation, however as it begins to transform to the martensite, the formation of oriented twins along the deformation directions results in a large macroscopic strain. From the strain versus temperature curves,

transformation temperatures can be also determined. The principal difference of the thermo-mechanical cycling in comparison with a pure thermal cycling is the formation of an almost single variant state in the martensite phase in the former case, and a self-accommodated variant structure, in which no macroscopic deformation is observed in the latter case.

From figure 2.9 (a) it is observed that, as the number of cycles is increasing, the strain versus temperature loops for the as-grown sample being initially square start to shift to lower temperatures with an increase of the transformation width. Moreover, as the cycling progresses, additional features start to appear and the phase transformation occurs in a stepwise fashion. In the case of the heat-treated sample, figure 2.9 (b), the loops' shape remains square-like over the full transformation and no drastic increase in the hysteresis is observed.

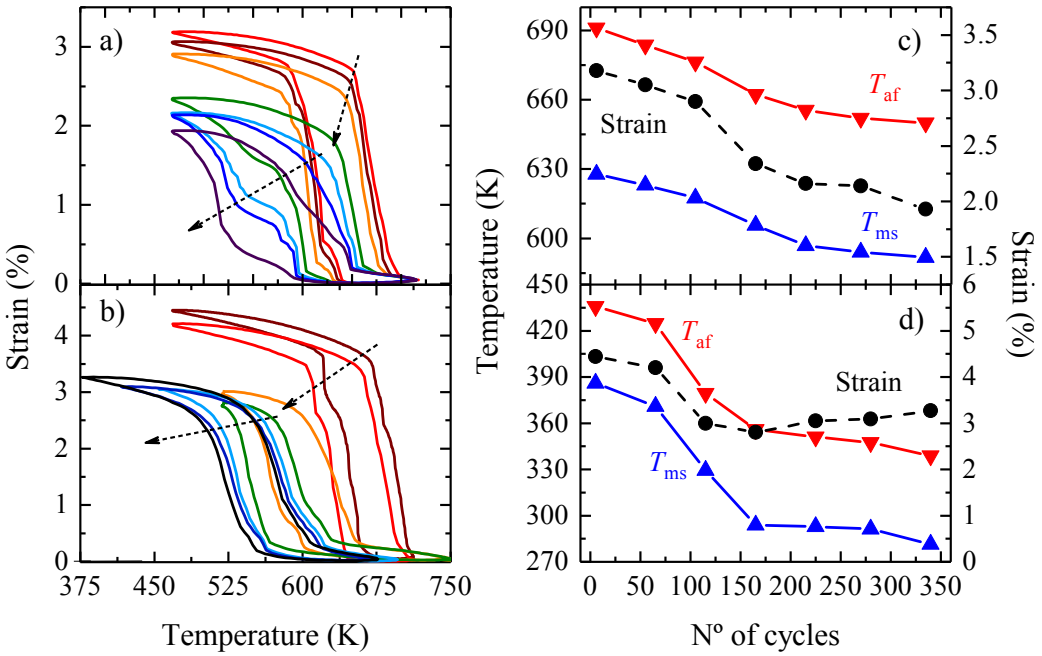

Figure 2.9: Selected strain versus temperature loops for the SC2 single crystal (a) as grown and (b) heat-treated. Evolution of the Martensitic start, T_{ms}, (blue down triangles), austenitic finish, T_{af}, (red up triangles) temperatures and the transformation-induced strain (black circles) as a function of the number of cycles for the as grown (c) and heat-treated (d) SC2 samples.

In both cases, there is a shift of the transformation to lower temperatures and a

decrease of the accumulated strain, which is related to the formation of the γ phase, as observed in the pure thermal cycling of the polycrystalline samples. The transformation temperatures, T_{ms} and T_{af} were determined from the strain-temperature loops by the tangent method. Both, the evolution of the transformation temperatures and strain as a function of the number of cycles is depicted in figures 2.9 (c) and (d) for the sample as grown and heat-treated respectively.

In the case of the heat-treated sample, a rapid drop of T_{af} and T_{ms} from 713 and 663 K is observed, followed by a plateau after approximately 160 cycles, with stabilized temperatures around 618 and 556 K respectively. For the as-grown sample, initial T_{af} and T_{ms} temperatures of 693 and 628 K gradually reduced and the slope changed around 210 cycles, however, it was still not clear if the fully stabilization had been achieved after 340 cycles. Even if the initial temperatures of the as-grown sample are lower, final values seem to be larger than the ones obtained for the heat-treated one; however, this fact should be taken with caution since stabilization is probably not complete.

Regarding the strain, the heat-treated sample shows larger values, both initially, with an almost 4.5 %, and after cycling showing 3.2 % of deformation. This non-monotonous decrease observed for both samples is related to the precipitation of the γ phase, with some incubation period and approaching equilibrium at around 150-200 cycles. However, the differences between the samples could be related to the different nucleation mechanisms. In this case, the heat treatment could acts as a pre-nucleation of the gamma phase prior to the cycling leading to a fast stabilization, while for the non heat-treated alloy the precipitation occurs only during the cycling.

In order to evaluate the influence of the precipitation on the mechanical properties and demonstrate the changes produced in the alloys, dynamic DMA measurements were performed. In this respect, dynamic mechanical analysis has proven to be a powerful tool in detecting the occurrence of structural and microstructural changes.[57] Two dynamic cycles with a frequency of 1 Hz and an oscillation strain amplitude of $2.5{\cdot}10^{-4}$ were performed before and after the total cycling. The heating and cooling rates were 2 K/min. The phase shift (tan δ) between the sinusoidal applied strain and the resulting stress gives information about the internal friction, whereas the E' modulus is obtained as the real part of the complex modulus.

The behavior obtained for both samples was similar, so, only the dependencies of the elastic modulus and loss tangent (tan δ) as a function of temperature for the as-grown sample before (blue curves) and after cycling (red curves) are shown in Figure 2.10 as representative ones.

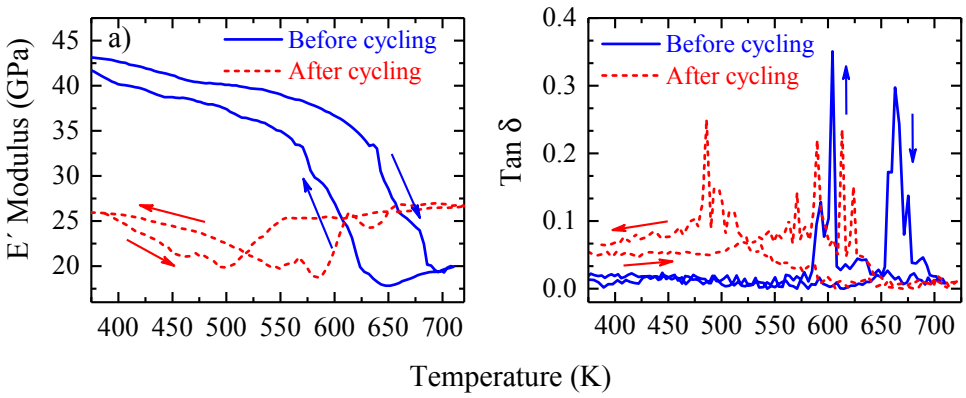

Figure 2.10: Heating-cooling temperature dependences of the elastic modulus (a) and concurrent loss tangent (b) of the as-grown sample SC2 before and after 340 thermo-mechanical cycles

The transformation temperatures can be clearly distinguished in both, E' Modulus, and Tan δ curves. In the E' Modulus' curve for the sample before cycling, an initial decrease with the temperature is observed in the martensite phase, followed by a drastic drop during the transformation and reaching a slightly increasing value in the austenite phase. The sample after cycling shows a 40% reduction (from ≈43 to ≈26 GPa) of the martensite + γ phase mixture's elastic modulus, in comparison to the sample before cycling. This effect is related to a rejuvenation process[46] and to the formation of deformation channels due to the spatial organization of crystal defects and/or particles. At the same time, the austenite phase becomes stiffer for more than 20% due to precipitation hardening.

Tan δ temperature dependence, before and after cycling, which is shown in Figure 2.10 (b), exhibits sharp peaks at the transformation temperatures during the cycling. These peaks are a result of the transient and non-transient contributions to the lattice softening through the transformation.[58] No essential variation of the energy dissipation capacity in the fully transformed phases before and after cycling

is observed, however, there is some lost during transformation, which is related to the reduction of the transformable phase and to the presence of residual stresses. Additionaly, the temperature shift of the transformation temperatures observed in the strain loops is also observed in the E'Modulus and Tan δ temperature dependent plots.

2.4.2 Thermo-mechanical behavior in the β region

For SC3, the same preparation procedure as for SC2 was followed. The dimensions of the samples as grown and heat-treated were 0.43 x 0.68 x 20.0 mm^3 and 0.52 x 0.80 x 20 mm^3 respectively.

The results of the measurements of the transformation temperatures are summarized in Table 2.1. To analyze the thermo-mechanical stability of SC3, static cycling up to 310 cycles was performed. The experimental conditions used for the thermo-mechanical cycling under load for the samples as grown and heat-treated are specified in Tables 2.5 and 2.6.

Table 2.5: Experimental conditions for static load thermal cycling of the as-grown SC3.

Measurement	N° of cycles	Load (N)	Lenth (mm)	T_{Max} (K)	T_{Min} (K)
1st	50	10	10	823	523
2nd	100	10	10	823	523
3rd	50	10	10	773	498
4th	50	10	10	753	453
5th	10	10	10	753	453
6th	25	10	10	753	453
7th	50	10	10	753	453

Regarding the results of the pure thermal cycling obtained in the polycrystalline samples from the β region, a stable thermo-mechanical behavior could be expected due to the absence of γ phase, however, degradation processes are observed in both samples. Selected strain versus temperature cycles for the sample in as grown and heat-treated states are shown in Figure 2.11 a) and b). The initial strain loops observed in two panels, (a) and (b), are similar to the ones of SC2, with a high de-

Table 2.6: Experimental conditions for static load thermal cycling sample of SC3 after the heat treatment.

Measurement	N° of cycles	Load (N)	Lenth (mm)	T_{Max} (K)	T_{Min} (K)
1st	35	10	10	823	523
2nd	55	5	10	823	523
3rd	35	5	10	823	523
4th	60	5	10	823	523
5th	50	5	10	798	473
6th	45	5	10	798	473
7th	50	5	10	798	473
8th	2	10	10	798	473

formation strain obtained in the martensite phase and a reduction during the transformation until the austenite phase is reached. Additionally, as in SC2, degradation processes occur.

A reduction of the transformation temperatures and the strain as the number of cycles increases is observed. The shape of the loops remains square like throughout the cycling, however, for the heat-treated sample they smear over the temperature.

T_{af}, T_{ms} and strain values were determined, as for the SC2 crystal, from the cycling loops. The evolution of these parameters as a function of the number of cycles is plotted in Figure 2.11 (c) and (d). The results show two distinct stabilization processes. In the as-grown sample there is a rapid drop of the transformation temperatures and strain which reach a stable value around 120 cycles, while for the heat-treated sample the decrease is more gradual and the slope changes roughly after 150 cycles. Initial strains for the samples are 3.8 % for the as grown and 8.2 % for the heat-treated, and, after degrading, they become 1 % and 2.7 % respectively. The same behavior is observed for the temperatures, as they shift from T_{af} of 713 K (as-grown) and 753 K (heat-treated) to 673 K as the stable temperature in both cases. Considering that the pure thermal cycling did not produce any precipitation of γ phase, the remarkable changes obtained for the transformation temperatures and strain during the thermo-mechanical cycling suggest that a combination of temperature and stress could induce the precipitation of γ phase even in the single β phase region.

In this case, taking into account that the pure thermal cycling, and therefore the

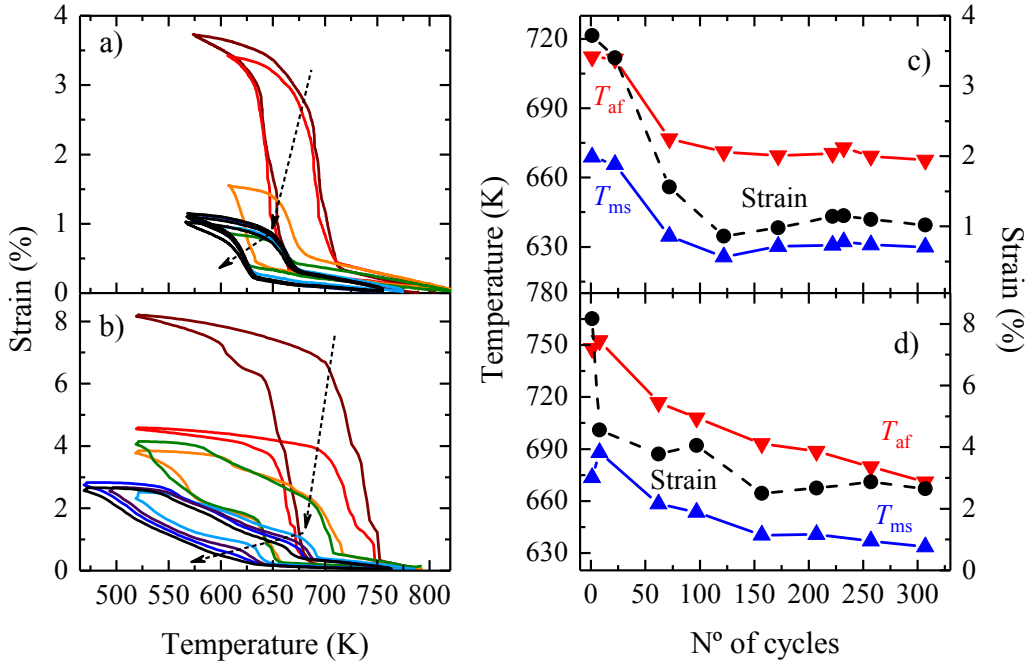

Figure 2.11: Selected strain versus temperature loops for the SC3 single crystal (a) as grown and (b) heat-treated. Evolution of the Martensitic start (T_{ms}), austenitic finish (T_{af}) temperatures and the transformation-induced strain as a function of the number of cycles for the as grown (c) and heat-treated (d) SC3 samples.

heat treatment, does not produce the formation of precipitates, the differences on the stabilization processes observed are related to the presence of residual stresses, which may influence the subsequent precipitates distribution during thermo-mechanical cycling.

To explain the possibility of a second phase precipitation in a single β phase region, the relative phase stability of the different phases under stress should be considered.

The ternary phase diagram in Figure 2.1, which shows the different phase stability regions relevant to this study, corresponds to an isothermal section under no stress. However, the Gibbs energy, G, which determines the equilibrium point between two phases, is also influenced by additional terms as shown in Eq. 2.1 with the $V^0\sigma_{ij}\epsilon_{ij}$

term for an applied stress,[59,60]

$$G^{Phase} = E - TS - V^0 \sigma_{ij} \epsilon_{ij} \tag{2.1}$$

Figure 2.12 shows a schematic representation of the Gibbs energy curves with and without an external applied stress. The red curve, which corresponds to the Gibbs energy in the absence of an applied stress, shows a unique energy minimum that leads to a single phase region stability. Under a certain stress, in the black curve, two energy minimum appears, so two different phases with two different compositions are now stable, becoming a dual phase region. That means, that a composition which falls in a single phase region under no stress, may fall in a dual phase when an external stress is applied.

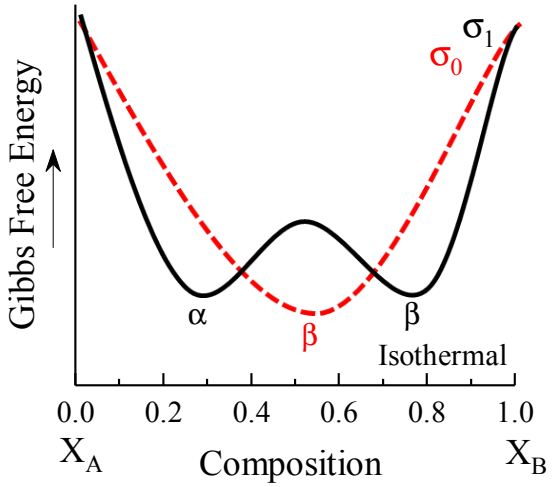

Figure 2.12: Schematic representation of the Gibbs Free Energy curve variation with (black line) and without applied stresses (red dashed line).

In order to corroborate the presence of γ precipitates and get evidence of this hypothesis, electron backscatter diffraction (EBDS) analysis was performed. EBDS technique provides information about the microstructural and crystallographic structure of the materials. Detailed description of the technique is included in Appendix B. EBSD was conducted using SGIker's shared SEM facility, which is equipped with an EBSD detector. This technique is highly sensitive to the surface defects so, to properly identify the phases additional electropolishing was performed in a nitric acid (25%) + ethanol solution applying a 30 V potential during 10 seconds.

For the analysis, the crystallographic structure of the martensite was defined as an $L1_0$-type ordered tetragonal unit cell, (I4/mmm symmetry), with cell parameters $aL1_0 = bL1_0 = 0.7604$ nm, $cL1_0 = 0.6711$ nm, in cubic coordinates of austenite $a_{bct} = b_{bct} = 0.5378$ nm, $cL1_0 = c_{bct}$ [43]), and a face-centered cubic lattice with a cell parameter: $a = b = c = 0.3576$ nm for the γ phase. Figure 2.13, depicts a SEM micrograph, showing the analyzed area, and two EBDS maps performed in this area.

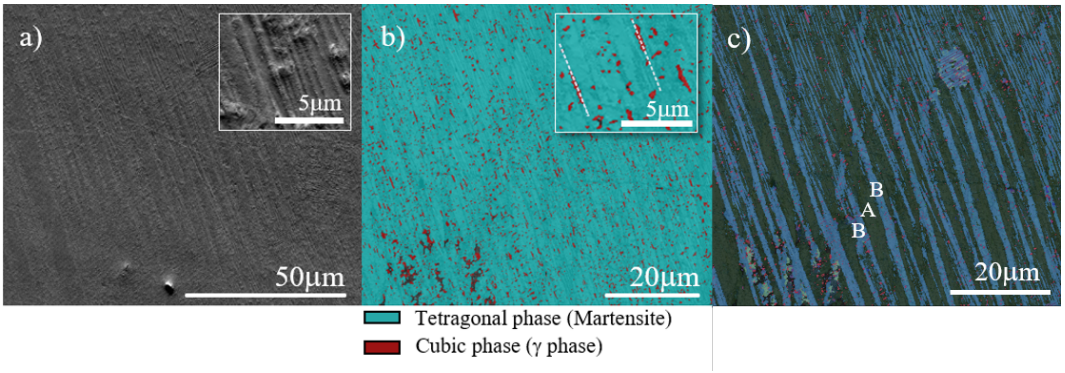

Figure 2.13: (a)SEM micrograph of the selected area of the thermo-mechanically cycled as-grown SC3 sample showing martensitic relief; (b) EBDS map of the surface area shown in (a) demostrating two different phases: the blue one corresponds to a non-modulated tetragonal martensite and the red one to cubic γ phase particles; (c) EBSD orientation map showing two twin variants, with different unit cell orientations A (grey ones) and B (blue ones). Insets show surface features in more detail.

The maps in Figure 2.13 show that the SC3 single crystal is mainly composed by two different phases. The plate-like microstructure observed in the SEM micrograph corresponds to the martensitic twins, while the round shape features are related to the presence of precipitates and/or to some impurities. The map (b) depicts the two different phases described above, and the map (c) shows the different crystallographic orientations of the twin variants. Both phases are clearly identified in the map (b): the blue one, which corresponds to the martensite matrix, and the red one, which corresponds to the γ precipitates. Additionally, two different twin orientations are alterned in the map (c), the grey one, named as A, and the blue one, B. Point EDX analysis was performed in some of the precipitates obtaining an average composition of $Ni_{62.3}Mn_{19.7}Ga_{18}$. The precipitates' shape is quite homogenous, with cross-sections less than 200 nm. The precipitates' distribution, specially for the elongated ones, seems to be oriented along the twins, as indicated in the inset (b). This fact reinforced the idea of a stable defect structure formed during cycling

that serves as a guide for the occurrance and disappearance of the same martensite variants during cycling.

These results support the idea of a stress-assisted precipitation of the γ phase. This process is a quite common phenomenon in other SMA's systems, and has been experimentally observed and modelled for Ni–Ti alloys,[61];[62] however, it has not been observed before for the Ni–Mn–Ga system.

Significant changes of the elastic modulus and loss tangents produced during cycling were also analyzed by dynamic DMA measurements, as for the SC2 sample.

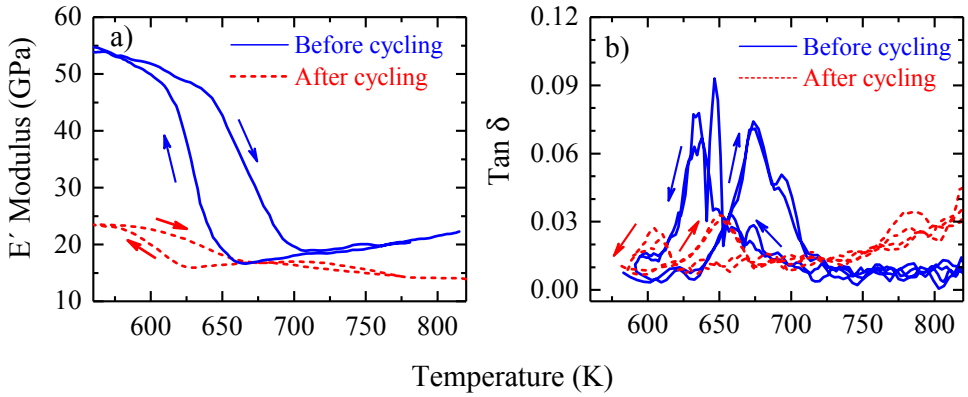

Figure 2.14: Heating-cooling temperature dependences of the elastic modulus (a) and concurrent loss tangent (b) of the as-grown SC3 sample before and after 310 thermo-mechanical cycles

Figure 2.14 depicts the elastic modulus (a) and loss tangents' (b) temperature evolution of the as-grown SC3 sample, before (blue) and after cycling (red). The behavior of the elastic modulus observed in Figure 2.14, is similar to the obtained for the dual phase region, however, in this case, a decrease of more than a half of its initial value is obtained for the martensite. In the austenite, the final decrease of the modulus is related to the higher temperatures reached in the former. The energy dissipation capacity decreases mainly during transformation. As observed for SC2, the two peaks corresponding to the martensitic transformation, and the shift of the transformation temperatures to lower values can be observed in the Tan δ curve.

2.5 Conclusions

High temperature shape memory alloys with transformation temperatures over 670 K were prepared. Two different kinds of alloys, from the β phase region and the dual $\beta + \gamma$ one were designed. Four polycrystalline alloys, and two single crystals, with compositions belonging to one or the other region were prepared. Thermal and thermo-mechanical cycling stability of the alloys was evaluated.

The results show two distinct behaviors. For the pure thermal cycling, the samples from the two phase region show a decrease of the transformation temperatures and the amount of transformable phase, due to the further precipitation of γ phase; while, the single β phase samples present no change in the transformation temperatures, due to the absence of second phases before and after cycling. Thermo-mechanical cycling, in turn, produces a decrease of both transformation and strain in all the alloys. The combination of temperature and an applied stress of 15-20 MPa is enough to induce the precipitation of a second phase even in the single phase region.

The thermal treatments also have a considerable influence on the thermo-mechanical behaviour of the alloys. In a dual phase region sample, the heat treatment acts as a pre-nucleation of the second phase, giving rise to different stabilization kinetics. In the case of the β phase region the effect is based on the stress release, leading to different precipitation processes. In both cases, initial transformation temperatures and strains were higher for the heat-treated samples.

The drastic difference between the temperature dependence of the elastic modulus for the sample as grown and cycled is in line with the consideration that the amount of γ phase is the main factor controlling the thermo-mechanical properties.

The thermo-mechanical cycling acted as a training procedure leading to a stable actuation at high temperatures, achieving for the heat-treated sample SC3 a recovery strain around 3% and a T_{af} of 673 K after cycling. Using this training method the appropriate levels of functionality at temperatures in the range of 673 – 773 K could be achieved, for compositions close to the studied ones.

Chapter 3

High Temperature Ferromagnetic Shape Memory Ni–Mn–Ga (Co, Cu, Fe) alloys: Composition effect

3.1 Introduction

Ni–Mn–Ga alloys have been extensively studied as magnetic shape memory alloys due to their potential application for actuators, sensors, energy harvesters and magnetic refrigeration systems.[34,42,63] The strong coupling between magnetic and elastic degrees of freedom, together with the large magnetic field-induced strains (MFIS) that they exhibit, about 10% for modulated martensites[36] and 12% for non-modulated ones,[30] make them promising candidates for many applications.

Nowadays, the development of high-temperature FSMAs (HTFSMAs), capable of working at temperatures over 373 K, has become an important task to fulfill the current requirements of modern technologies, especially, those used in the automotive industry. The temperature limit of the MFIS can be potentially extended to higher temperatures by using Ni–Mn–Ga tetragonal non-modulated (NM) martensites, which, for certain compositions, exhibit higher martensite transformation (T_M) temperatures. This sensitive dependence of martensitic transformation with composition is well-known for this kind of systems and was mentioned before for the HTMSA in the previous chapter. However, the key problem of the Ni–Mn–Ga ternary system is the relative stability of the Curie Temperature, (T_C), and the impossibility to get MFIS in the paramagnetic martensite.[1,41,64]

The use of additional elements comprises a new development path to solve the limitations of the ternary HTFSMA systems. Following this direction previous studies, have demonstrated that the addition of a fourth and even a fifth component such as Fe, Co or Cu, was an efficient way to tune the values of T_C and T_M temperatures alongside other materials' properties.[30,65–72]

Furthermore, it has been observed that the selective substitution of additional elements is also an important issue to understand the alloying effect on the final properties.[73,74] Several works have reported the effect of Cu addition on the Ni–Mn–Ga system. Replacing Mn or Ga with Cu in their respective sites linearly increases T_M but leads to a decrease of T_C[66,67,75,76] whereas substitution by Cu in the Ni sites results in a decrease of T_M.[77] Similar studies have been performed in order to determine the influence of preferential site occupancy for Co and Fe dopants.[68,69,71,78–80] These studies have shown that Co has a strong tendency to occupy the Ni sublattice, resulting in an increase of T_C and a decrease of T_M,[71,80] while Fe preferentially occupies Mn sites.[68,80]

Nevertheless, although some works have focused on increasing T_M and T_C by simultaneous addition of Co/Cu or Fe/Co pairs, no values higher than 353 K for T_M and T_C have been achieved in the same alloy.

In this chapter, different series of multicomponent alloys have been developed and systematically studied with the aim of tuning the martensitic transformation and Curie temperatures over 373 K and 423 K, respectively.

3.2 Experimental Part

Pollycrystalline samples were prepared at Lappeenranta University of Technology and at the University of Basque Country from high purity elements (Ga 99.999%, Ni 99.95%, Mn 99.95%, Co 99.95%, Cu 99.95% and Fe 99.99%) as described in section 2.2.

Two different molds were used for the casting: a copper mold with 4 mm in diameter and a steel one with 6 mm in diameter.

The alloys were homogenized at 1223 K during 24 h followed by a slow cooling to 723 K and held there for 4 h to promote a $L2_1$–structure. The powder samples were hand-milled and heat-treated at 923 K during 2h to relax the stresses. For the heat treatment, the powder was wrapped in Tungsten Foil and placed in an alumina crucible inside the in-house made furnace. The alloy's composition was determined

by EDX within a 0.5 at.% uncertainty.

For the characterization of the alloys, 4 mm in diameter by 1 mm length disks were cut with a low speed saw and polished until a mirror finish on the surfaces was achieved.

Differential Scanning Calorimeter (DSC) measurements were carried out with an 822e Mettler Toledo DSC instrument, located in the macromolecular chemistry department of the University of Basque Country. This technique was used to determine the martensitic transformation temperatures of the samples (T_{af} and T_{ms}) at a heating/cooling rate of 5 K/min. T_M values were determined by the tangent method.[81]

A Vibrating Sample Magnetometer from the SGiker services, located at the University of Basque Country was used to determined the Curie temperatures, of the austenite, T_C^A, or the martensite, T_C^M. T_C values were obtained as the minimum of the first derivative of the M(T) curve at 0.01 T field.

Both methods, DSC and VSM allow for the determination of T_M and T_C. However, DSC is more appropriate for T_M and M(T) for T_C, as seen in the figures below.

X-ray diffraction (XRD) in a Philips X'Pert, MPD diffractometer with CuKα radiation, from the SGiker services at the University of Basque Country, was used for the crystallographic analysis.

3.3 Influence of Fe

In this section, a simultaneous addition of Cu, Co and Fe to the stochiometric $Ni_{50}Mn_{25}Ga_{25}$ Heusler alloy is analyzed as an efficient procedure to conveniently tailor T_M and T_C over 373 K and 423 K, respectively, in a $Ni_{50-y}Co_yMn_{25-x}Fe_xGa_{25-z}Cu_z$ system.

In the Ni–Mn–Ga alloys the magnetism is mainly due to the contribution from the Mn atoms, and to a lesser degree from the Ni ones. In order to improve the magnetic properties a substitution with two magnetic atoms was proposed. The substitution of Ni by Co, which possess a higher saturation magnetization, and of Mn by Fe, that for the ternary system, resulted in an enhanced exchange interaction.[69,82] The addition of Cu in place of Ga, was selected to increase T_M, as was previously reported in several studies.[66,67,75,76]

As a starting point, the $Ni_{45}Co_5Mn_{25-x}Fe_xGa_{20}Cu_5$ system was selected, with

a fixed content of Co and Cu, and a substitution of Mn by Fe in a range from 0 to 8 at.%. The substitution of Ni by Co, Ga by Cu and Mn by Fe was decided based on a review of the relevant literature on the preferential site occupancy of these substitutional atoms. Nevertheless, the chemical order is analyzed in Chapter 4 by neutron diffraction to experimentally check the hypotheses reported in the literature.[71,79]

This series allowed, for the first time, a study of a six component Ni–Mn–Ga based system for high temperature applications and more specifically of the influence of Fe addition on the magnetic and structural properties.

The compositions of the samples studied are shown in Table 3.1. The labels of the samples, Fe0, Fe1, Fe2, Fe4, Fe5, Fe6 and Fe8 were given according to the nominal amount of Fe added. The compositions obtained by EDX analysis were in good agreement with the nominal ones.

Table 3.1: Nominal and measured by EDX compositions (at.%) of the studied samples. The compositions were determined with a 0.5% error.

Alloy	Nominal composition (at.%)	Measured composition (at.%)
Fe0	$Ni_{45}Co_5Mn_{25}Ga_{20}Cu_5$	$Ni_{45.1}Co_{4.8}Mn_{25.3}Ga_{19.6}Cu_{5.2}$
Fe1	$Ni_{45}Co_5Mn_{24}Fe_1Ga_{20}Cu_5$	$Ni_{44.7}Co_{4.8}Mn_{24.2}Fe_{1.4}Ga_{19.5}Cu_{5.4}$
Fe2	$Ni_{45}Co_5Mn_{23}Fe_2Ga_{20}Cu_5$	$Ni_{44.8}Co_{4.8}Mn_{22.7}Fe_{2.5}Ga_{19.7}Cu_{5.5}$
Fe4	$Ni_{45}Co_5Mn_{21}Fe_4Ga_{20}Cu_5$	$Ni_{44.6}Co_{4.8}Mn_{21}Fe_{4.4}Ga_{19.6}Cu_{5.6}$
Fe5	$Ni_{45}Co_5Mn_{20}Fe_5Ga_{20}Cu_5$	$Ni_{45}Co_{4.7}Mn_{20}Fe_{5.6}Ga_{19.2}Cu_{5.5}$
Fe6	$Ni_{45}Co_5Mn_{19}Fe_6Ga_{20}Cu_5$	$Ni_{44.6}Co_{4.9}Mn_{18.5}Fe_{6.4}Ga_{20.1}Cu_{5.5}$
Fe8	$Ni_{45}Co_5Mn_{17}Fe_8Ga_{20}Cu_5$	$Ni_{45.3}Co_{4.8}Mn_{16.4}Fe_{8.5}Ga_{19.5}Cu_{5.5}$

3.3.1 Structural analysis

XRD analysis for this series was performed on the polycrystalline samples. Room temperature X-ray diffraction (XRD) patterns are presented in Figure 3.1. They show that for an Fe content up to 6 % the phase is a non-modulated tetragonal martensite with an I4/mmm symmetry group.[83] The peak indices are given according to the austenite cubic phase. No additional reflections were observed. Only in the case of Fe8 two additional reflections, (220)A and (400)A, corresponding to the austenite phase were found. The coexistence of the two phases is related to the martensitic transfomation being close to room temperature.

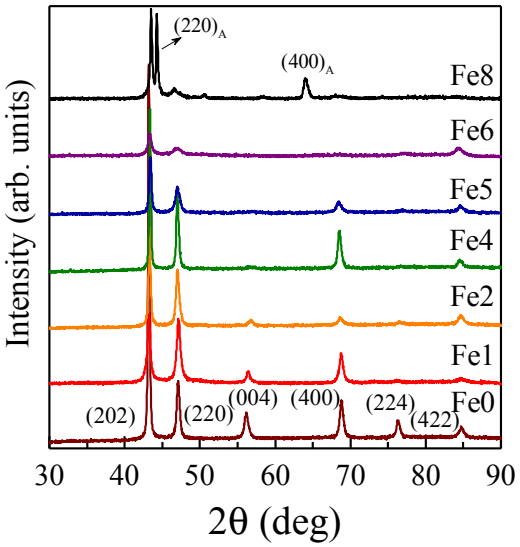

Figure 3.1: X–ray diffraction patterns at room temperature for polycrystalline samples of $Ni_{45}Co_5Mn_{25-x}Fe_xGa_{20}Cu_5$ (x = 0, 1, 2, 4, 5, 6, 8) alloys. The non-modulated tetragonal unit cell in the cubic coordinates is used for the pattern indexing. The two additional reflections observed in Fe8 correspond to austenitic (220)A and (400)A reflections.

Lattice parameters and c/a ratio in cubic coordinate system obtained by pattern matching refinements are collected in Table 3.2.

Table 3.2: Unit cell parameters and tetragonality ratio (c/a) of the non-modulated martensitic lattice measured at room temperature. a_0 is the cell parameter of cubic austenite in the Fe8 alloy.

Alloy	Cell parameters (nm)			Errors	c/a	Errors
	$a = b_{Mart}$	c_{Mart}	a_{Aust}			
Fe0	0.547	0.656	-	0.001	1.199	0.004
Fe1	0.549	0.655	-	0.001	1.193	0.004
Fe2	0.548	0.650	-	0.001	1.186	0.004
Fe4	0.550	0.650	-	0.001	1.182	0.004
Fe5	0.549	0.649	-	0.001	1.182	0.004
Fe6	0.550	0.649	-	0.001	1.180	0.004
Fe8	-	-	0.583	0.001	-	-

It is known that the twinning stress in Ni-Mn-Ga alloys increases with increasing

c/a ratio,[24] and therefore, a low c/a value is required for them to be magnetostrain active. The c/a values typically obtained for the ternary Ni–Mn–Ga system with a non-modulated martensite structure are in the range of 1.18-1.25. Moreover, N. Lanska et al.[1] and J. Pons et al.[84] reported that c/a values increase with increasing average transformation temperature, $T_0 = (T_{ms} + T_{af})/2$.

Figure 3.2 shows the room temperature evolution of c/a ratio, which decreases with increasing the Fe content (or decreasing T_0). However, the lowest value of 1.18 is still large for MFIS, which has only been reported for a non-modulated alloy with a c/a ratio close to 1.15.[65]

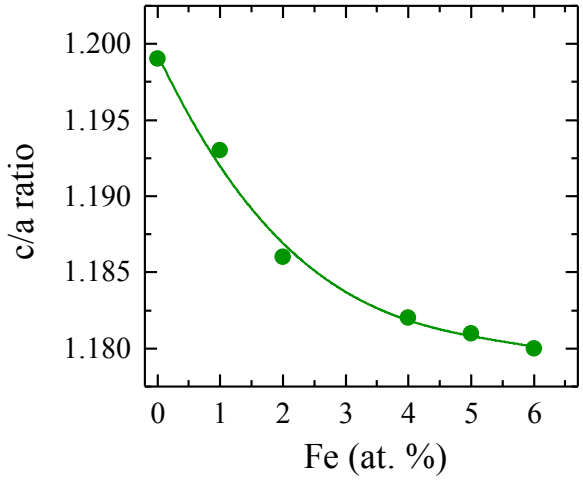

Figure 3.2: Compostion dependence of the c/a ratio for the studied samples. The line is used as a guide for the eye.

3.3.2 Transformation behavior

Figure 3.3 shows DSC curves of the polycrystalline alloys after the heat-treatment. The shift between heating/cooling curves is due to the hysteresis of the transformation: $\Delta T = T_{af} - T_{ms} \approx 10$ K for all the alloys. The values of T_{af} and T_{ms} are summarized in Table 3.3.

Well defined and sharp DSC peaks show a single transformation with no intermartensitic transformations. They also suggest no composition gradient or internal stresses in the samples.

The latent heat of the transformation was measured as an average of the peaks'

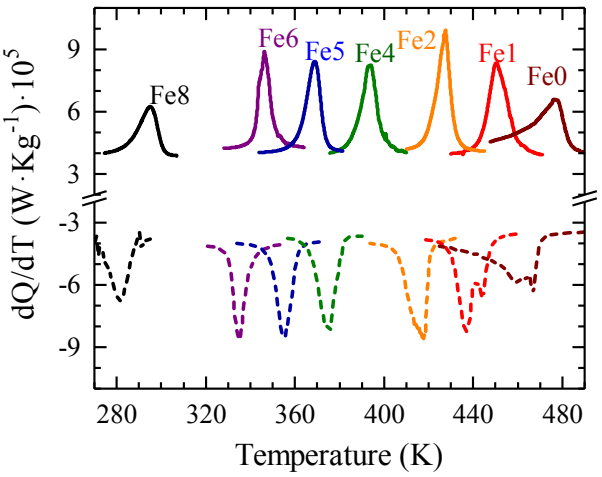

Figure 3.3: DSC thermograms on heating (solid lines) and cooling (dashed lines) for $Ni_{45}Co_5Mn_{25-x}Fe_xGa_{20}Cu_5$ (x = 0 - 8 at.%) alloys

Table 3.3: Alloy name, martensitic transformation temperatures, T_{af} and T_{ms}; determined by DSC, Curie temperatures, ${T_C}^M$ and ${T_C}^A$ determined by VSM; and latent heat, Q of the alloys studied.

Sample	T_{af}(K)	T_{ms} (K)	${T_C}^M$(K)	${T_C}^A$(K)	Q (J/g)
Fe0	483	470	313	–	4.6
Fe1	461	447	350	–	5.7
Fe2	432	420	397	–	5.2
Fe4	408	382	458[a]	439	4.5
Fe5	374	362	–	445	4.4
Fe6	351	340	–	448	3.6
Fe8	303	288	–	457	2.7

area on heating and cooling. Even if the latent heat variation is not very drastic between the different alloys, it seems to decrease for the alloys with an iron content higher than 5 at.%. This effect could be related to martensite destabilization, and a reduction in the amount of the transformable phase.

Figure 3.4 depicts M(T) curves. On heating Fe4, Fe5 and Fe6, show a magnetization increase at the martensitic transformation and a further reduction at the Curie temperature. The thermal hysteresis around 10 K, is the same as in DSC. The rest of the samples only show the Curie temperature. In the case of Fe0, Fe1 and Fe2 the

martensitic transformation cannot be detected as it falls in the paramagnetic regime, however, for Fe2 a small variation can be observed around 420 K, the T_{ms} obtained by DSC. Conversely, for the sample Fe8, the transformation was not detected as it occurs below the temperature range used.

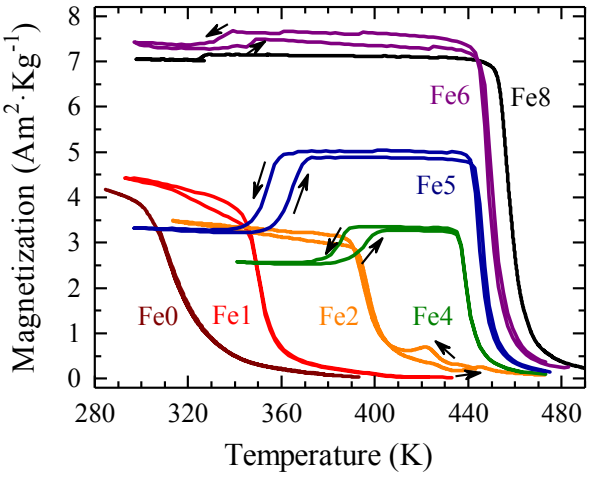

Figure 3.4: Temperature dependences of the magnetization in a magnetic field of 0.01 T for all the samples studied. The forward and reverse martensitic transformations are indicated by down and up arrows, respectively.

The T_M temperatures estimated from Figure 3.4 are in fairly good agreement with the values obtained from the DSC curves. Two different kind of T_C can be observed depending on whether they belong to martensite ($T_C{}^M$) or austenite ($T_C{}^A$) phases. The $T_C{}^A$ and $T_C{}^M$ values measured by VSM are summarized in Table 3.3.

Figure 3.5 depicts the composition dependence of structural and magnetic transformation temperatures. Martensite transformation temperatures linearly decrease with Fe content, at a rate of about -22 K/at.%. This trend shows no change on crossing from the paramagnetic to the ferromagnetic state of the austenite phase. The composition dependence of $T_C{}^A$ is weaker than $T_C{}^M$, the latter one drastically increases with increasing Fe content. The slope of the Curie temperature versus composition curves in the martensite is of 42 K/at.% and 4.4 K/at.% for the austenite one. Similar linear composition dependencies of the structural and magnetic transformation temperatures were also observed in $Ni_{50}Mn_{50-y}X_y$ (X=In, Sn and Sb) alloys.[85]

Considering a linear extrapolation of $T_C{}^M$ to higher Fe content, a higher T_C in

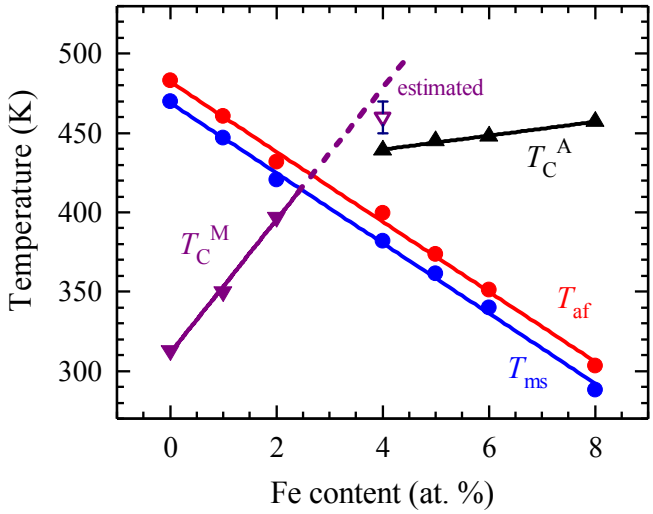

Figure 3.5: Concentration dependences of the transformation temperatures for studied alloys. T_{ms} and T_{af} are the martensitic start and austenitic finish transformation temperatures. ${T_C}^M$ and ${T_C}^A$ are the Curie points for martensite and austenite, respectively. The lines are linear fits to the corresponding experimental data. Dashed line is linear extrapolation of the ${T_C}^M$ evolution. A hollow triangle stands for ${T_C}^M$ point for Fe4 alloy estimated by the comparative method explained in the text.

the martensite than in the austenite will be obtained, which is in line with the concept of two different Curie temperatures, postulated by Chernenko et al.[47] It is impossible to obtain directly ${T_C}^M$ for these samples but can be estimated by extrapolating M(T) or by Arrot plots[86] for Fe2 and Fe4. Different approaches based on Arrott plot were previously used to determine ${T_C}^M$.[87] In this case, we use a comparative method between an alloy with defined ${T_C}^M$ (Fe2) and the analyzed one (Fe4). The magnetization curves were measured up to a maximum field of 8 T at every 5 K from 5 to 310 K. Figure 3.6 shows the square of the spontaneous magnetization vs. μ_0H/M (Arrott plot). The curves show the characteristic behavior of a ferromagnetic material. A clear reduction of the magnetization with the temperature is observed for both, Fe2 (a) and Fe4 (b), due to them nearing the Curie temperature.

To estimate Fe4's ${T_C}^M$ a similar temperature dependence of the saturation magnetization in the martensitic state for both alloys should be considered. Taking into acount this premise, a comparison of the reduced M/M$_s$ as a function of the reduced temperature, T/T_C, for the two alloys was performed. Spontaneous magnetization, M$_s$, at different temperatures was obtained by the M$_s^2$ values extrapolated from the

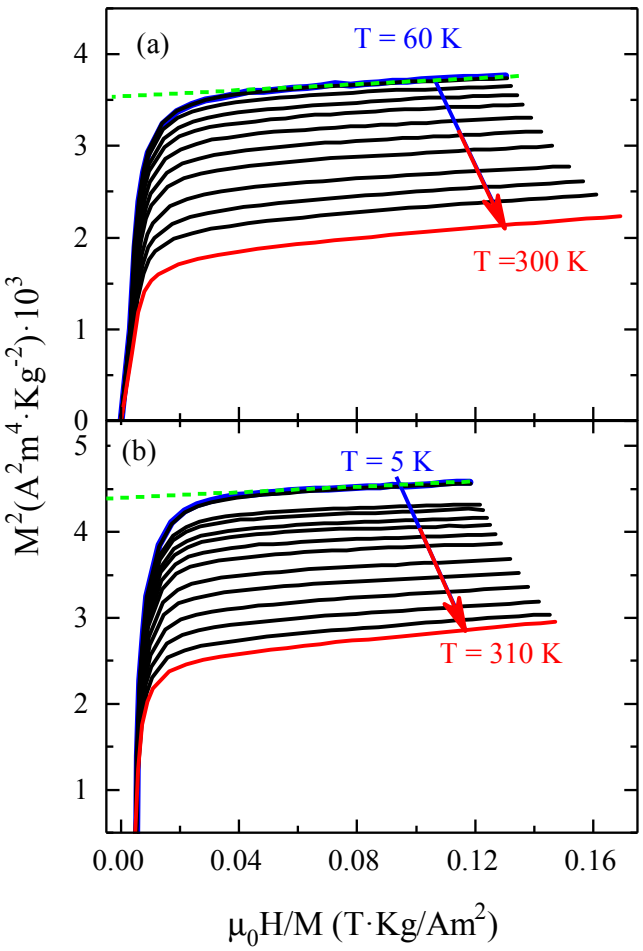

Figure 3.6: Selected Arrott plots (M^2 vs $\mu_0 H/M$) at different temperatures and linear extrapolation example (green dashed line) to obtain the spontaneous magnetization, M_s, for Fe2 (a) and Fe4 (b) alloys.

Arrott plots (M^2 vs $\mu_0 H/M$) (See the green dashed line in Figure 3.6 as an example). In the case of Fe4, different tentative values of ${T_C}^M$ were tested to make both curves coincide. Figure 3.7 shows the reduced M/M_s as a function of the reduced temperature T/T_C for the samples Fe2 and Fe4. A value of ${T_C}^M = 460$ K for Fe4 was taken as the temperature at which both curves coincide (see Figure 3.7).

In spite of being a rather rough estimation, the method allows to approximate the value of ${T_C}^M$, which is not otherwise accessible because of ${T_C}^M > T_{af}$. The estimated ${T_C}^M$ of 460 K is slightly below the value of 477 K obtained by extrapolation from experimental data, (See Figure 3.5) but it is still higher than the experimentally

obtained for the austenitic one. This result is in agreement with previous theoretical calculations made for the Ni-Mn-Ga system.[47]

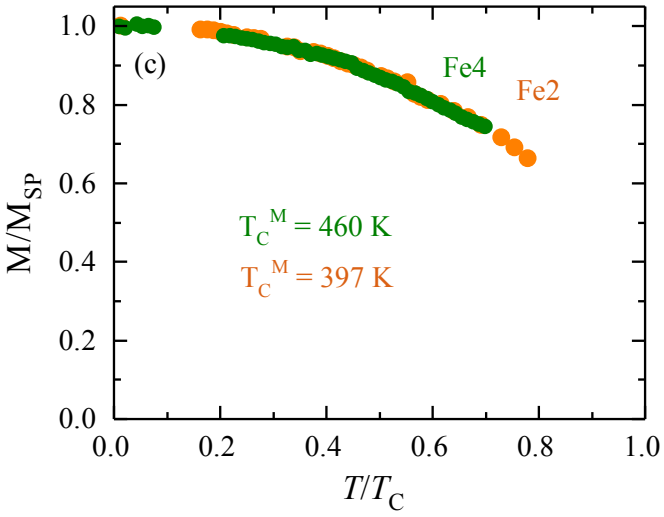

Figure 3.7: The reduced magnetization, M/M_s, as a function of the reduced temperature, T/T_C, for the Fe2 and Fe4 alloys. $T_C{}^M = 460$ K for Fe4 was estimated as the temperature at which both curves coincide.

3.3.3 Magnetic properties

Similar to the transformation and Curie temperatures, the saturation magnetization, M_s, is an important parameter for the FSMA's applicability as magnetic actuators. The maximum magnetostress, σ_{mag}, that could be induced in an alloy by the magnetic field is proportional to the M_s. Thus, this value should be maximized in the material to be really technologically applicable. The relation between M_s and σ_{mag} can be given by the following equations:

$$K_u = \frac{1}{2}(\mu_0 M_s \cdot H_k) \tag{3.1}$$

$$\sigma_{mag} = (1 - \frac{a}{c})^{-1} K_u \tag{3.2}$$

where the K_u, is the magnetic anisotropy, H_k, the anisotropy field and a/c, the ratio of the two independent crystal lattice parameters of the martensite.

Saturation magnetization, M_s, was determined at 10 K in applied magnetic fields up to 8 T. Figure 3.8 (a) illustrates the magnetization curves as a function of the applied field, M(H) for the samples studied. The results for sample Fe2 could not be considered due to thermal instabilities during the measurement at 10 K. The curves obtained show a behavior typical for ferromagnetic materials, reaching saturation at a field of about 1.5 T. M_s values were obtained from M(H) curves by a linear extrapolation of high field values to μ_0H=0. The values obtained were plotted as a function of Fe content in Figure 3.8(b) and are summarized in Table 3.4. The composition dependence of the saturation magnetization observed in this figure shows a drastic increase from 66 (Fe0) to 84 (Fe8) Am^2/kg .

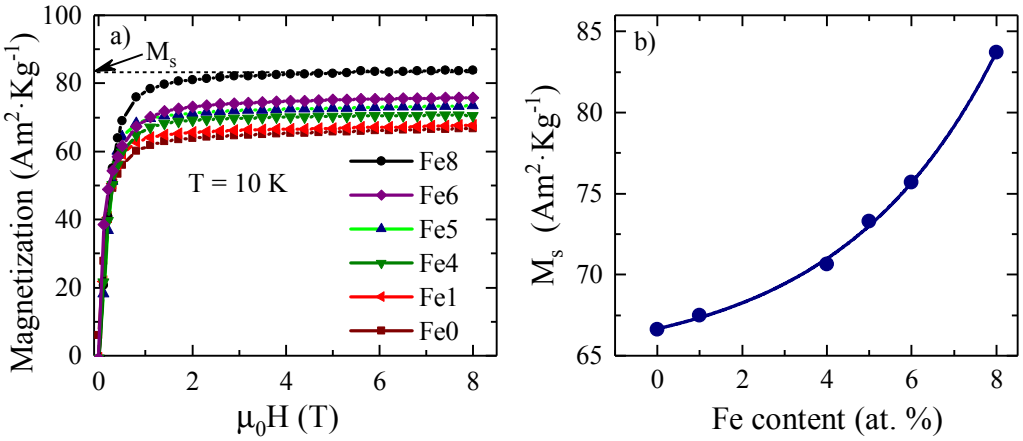

Figure 3.8: (a) Field dependence of magnetization at 10 K measured from applied fields from 0 to 8 T for the alloys studied. (b) Spontaneous magnetization at 10 K as a function of Fe content. The solid line is shown as a guide for the eye.

The main contribution to the magnetic moment in the Ni_2MnGa Heusler alloys comes from the Mn atoms.[88] As we replace Mn by Fe, the increase of T_C and decrease of T_M can be related to the ferromagnetic contribution of Fe atoms that increase the exchange interactions and stabilize austenite phase. Taking into account the data from Tables 3.1 and 3.3, this indicates that namely the magnetic interaction is a dominant factor affecting phase stability in quaternary Ni-Mn(Fe)-Ga system,[69,89] whereas the electron concentration governs phase stability in the ternary Ni-Mn-Ga system.[41]

Table 3.4: Alloy notation, and saturation magnetization determined for the alloys studied.

Sample	M_s (Am^2/kg) at 10 K
Fe0	66.6
Fe1	67.5
Fe2	–
Fe4	70.6
Fe5	73.3
Fe6	75.7
Fe8	84

3.4 Influence of Cu

We have found two HTFSMA compositions, Fe4 and Fe5, which exhibit simultaneously high T_M and ${T_C}^A$ temperatures. In order to understand the multiple doping mechanisms affecting the Ni-Mn-Ga-(Co, Fe, Cu) system, the effect of Cu addition on the transformation and Curie temperatures as well as on the crystallographic structure is now studied.

With the aim of analyzing the substitutions of Mn or Ga by Cu, two different series, (A) $Ni_{43}Co_7Mn_{20-x}Fe_2Ga_{21}Cu_{7+x}$ (x = 0.25, 0.5, 0.75, and 1.0 at.%), and (B) $Ni_{43}Co_7Mn_{20}Fe_2Ga_{21-x}Cu_{7+x}$ (x = 0.5, 1 and 1.5 at.%); and a base composition, S0, have been chosen. In these systems the amount of Co and Fe was fixed at 7 and 2 at.% respectively.

Measured compositions are summarized in Table 3.5. Several EDX measurements were averaged to reduce the instrumental error to 0.3%. Table 3.5 shows that the actual compositions are close to the nominal ones.

For the A series the composition change is within the instrumental error, however, a systematic increase of Cu is observed in both series, which leads comparability of the samples relative to each other.

3.4.1 Structural analysis

The structural analysis of the Cu series was performed for heat-treated powder samples. Figure 3.9 shows the room temperature XRD patterns of martensites for the A (a) and B (b) alloys series. The structures obtained were indexed in terms of the

Table 3.5: Nominal and measured composition (at.%) of the full set of samples measured by EDX. The compositions were determined with a 0.3% error.

Alloy	Nominal composition (at.%)	Measured composition (at.%)
S0	$Ni_{43}Co_7Mn_{20}Fe_2Ga_{21}Cu_7$	$Ni_{42.5}Co_{7.1}Mn_{19.7}Fe_{2.1}Ga_{21.2}Cu_{7.4}$
A1	$Ni_{43}Co_7Mn_{19.75}Fe_2Ga_{21}Cu_{7.25}$	$Ni_{42.6}Co_7Mn_19.2Fe_2Ga_{21.6}Cu_{7.6}$
A2	$Ni_43Co_7Mn_{19.5}Fe_2Ga_{21}Cu_{7.5}$	$Ni_{42.4}Co_{7.1}Mn_{19.4}Fe_2Ga_{21.1}Cu_8$
A3	$Ni_{43}Co_7Mn_{19.25}Fe_2Ga_{21}Cu_{7.75}$	$Ni_{43.1}Co_7Mn_{19}Fe_{2.1}Ga_{20.7}Cu_{8.1}$
A4	$Ni_{43}Co_7Mn_{19}Fe_2Ga_{21}Cu_8$	$Ni_{42.9}Co_{7.1}Mn_{19.2}Fe_{2.1}Ga_{20.4}Cu_{8.3}$
B1	$Ni_{43}Co_7Mn_{20}Fe_2Ga_{20.5}Cu_{7.5}$	$Ni_{42.9}Co_{6.8}Mn_{19.7}Fe_2Ga_{20.8}Cu_7.8$
B2	$Ni_{43}Co_7Mn_{20}Fe_2Ga_{20}Cu_8$	$Ni_{42.7}Co_{6.9}Mn_{19.3}Fe_{2.1}Ga_{20.6}Cu_{8.4}$
B3	$Ni_{43}Co_7Mn_{20}Fe_2Ga_{19.5}Cu_{8.5}$	$Ni_{42.7}Co_{7.2}Mn_{19.7}Fe_{2.3}Ga_{19.2}Cu_{8.9}$

non-modulated (NM) tetragonal structure.[83]

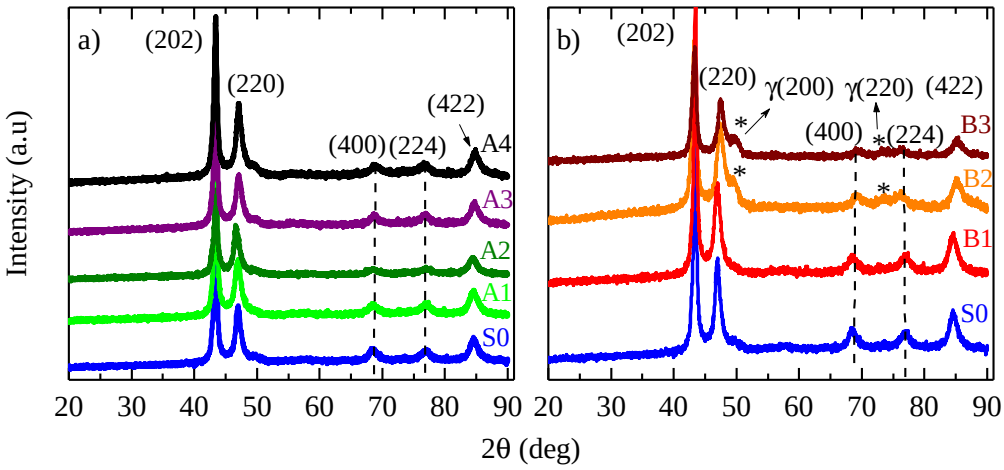

Figure 3.9: X-ray diffraction patterns at room temperature for the A (a) and B series (b). The non-modulated tetragonal unit cell in the cubic coordinates is used for the pattern indexing. Additional reflexions for the second phase (γ) are indicated by arrows and asteriscs.

In the case of the A series all the reflections presented correspond to the non-modulated martensite. On the contrary, for the B series, additional weak reflections, around $2\theta = 50°$ and $73°$, appeared for the samples with Cu content higher than 8 at.%. The intensities of the additional peaks increase with the increasing Cu content, however their locations on the 2θ scale remain nearly constant. This means that the additional peaks belong to a new phase. Previous studies in Ni–Mn–Ga–Cu alloys

determined that the solubility limit of Cu in this ternary alloy is close to 8 at.%.[75] Above this amount of Cu, a second phase precipitation occurs. The additional peaks were indexed as the (200) and (220) reflections of the γ-phase precipitates.

The lattice parameters were determined at room temperature by pattern matching refinements of the diffraction patterns indexed according to the cubic parent phase. The results are shown in Table 3.6.

Table 3.6: Alloy notation and room temperature lattice parameters of the non-modulated martensite phase for all the studied samples.

Alloy	Cell parameters (nm)		Errors	c/a	Errors
	a_{Mart}	c_{Mart}			
S0	0.549	0.647	0.001	1.179	0.004
A1	0.549	0.646	0.001	1.176	0.004
A2	0.550	0.641	0.001	1.165	0.004
A3	0.548	0.650	0.001	1.186	0.004
A4	0.547	0.650	0.001	1.188	0.004
B1	0.543	0.653	0.001	1.194	0.004
B2	0.545	0.651	0.001	1.202	0.004
B3	0.543	0.658	0.001	0.211	0.004

To evaluate the composition effect on the structure, the c/a ratio was plotted as a function of Cu addition in Figure 3.10. Two clearly distinct behaviors can be observed for the two series. In the case of the A series (See Figure 3.10) (a), an initial decrease from 1.179 to 1.165 occurs followed by an increase up to 1.188 for the 8 at.% of Cu. On a contrary, the results for the B series (See Figure 3.10) show a monotonous increase of the c/a in the full range of the compositions studied. These results suggest that the effects on the structure are strongly related on whether Cu substitutes Mn or Ga.

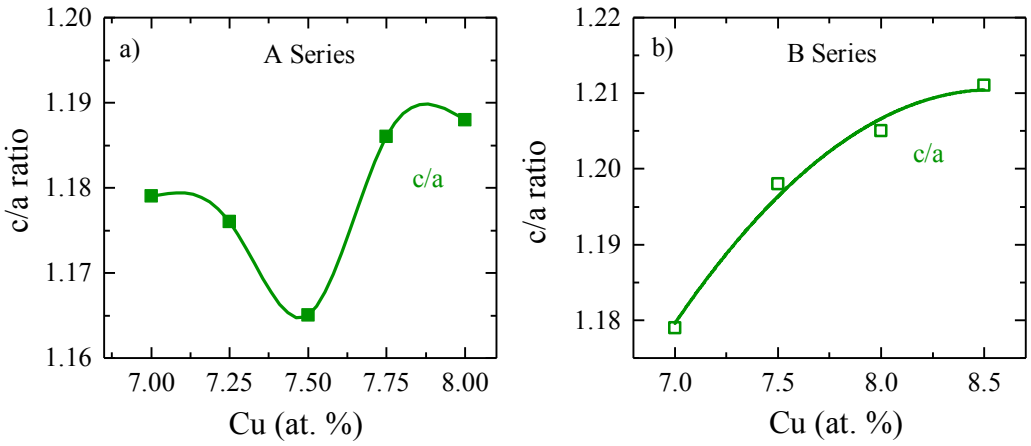

Figure 3.10: Composition dependence of the c/a ratio for the studied samples. The c/a values for the A series (a) are indicated by full circles, and for the B series (b) by open circles. The lines are just guides for the eye.

Incidentally, a qualitative behavior, similar to that observed for c/a in the series A, was also reported by Wei et al.[90] for $Ni_{46}Mn_{28-x}Ga_{22}Co_4Cu_x$ alloys. There, a minimum value of c/a = 1.145 was obtained for 4 at.% Cu. Here, the lowest c/a value at room temperature is 1.165, for the alloy A2. As MFIS has only been experimentally confirmed for the non-modulated martensite $Ni_{46}Mn_{24}Ga_{22}Co_4Cu_4$, with c/a ratio close to 1.15,[30] the alloy A2, should be suitable for MFIS at high temperature (near T_{as}), as we expect a decrease of c/a in the vicinity of the T_M.

3.4.2 Transformation behavior

Figure 3.11 shows the DSC thermograms for the two set of alloys. The T_{af} and T_{ms} values are summarized in Table 3.7.

Thermal hysteresis is around 15-20 K for all the samples except B3, where it reaches 40 K. Such a large hysteresis was also observed for Ni–Mn–Ga alloys with a Cu content over 8 at.%.[75,91] The latent heat increases as a function of Cu addition, being larger for the B series as seen in Table 3.7.

Figure 3.12 shows the magnetization as a function of temperature. For the A series, two distinct behaviors can be seen. Lower Cu content samples, S0, A1 and A2, show magnetization changes related to the martensitic and the Curie temperature of the austenite. On the contrary, A3 and A4, show the Curie temperature of the martensite, and, at higher temperatures, there is an overlap of the martensite

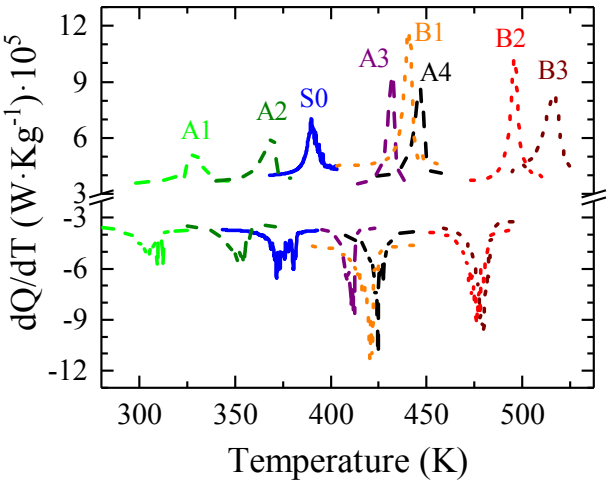

Figure 3.11: DSC thermograms on heating and cooling for the A series (dashed lines) B series (dot lines) and S0 (solid line) measured after heat-treatment.

Table 3.7: Alloy name, martensitic transformation temperatures T_{af} and T_{ms} determined by DSC, Curie temperatures, ${T_C}^M$ and ${T_C}^A$, determined by VSM, thermal hysteresis of the transformation and latent heat of the full sets of alloys.

Alloy	T_{ms} (K)	T_{af} (K)	${T_C}^M$ (K)	${T_C}^A$ (K)	Hysteresis (K)	Q (J/g)
S0	383	396	–	439	13	2.4
A1	359	372	–	439	13	2.6
A2	317	338	–	436	21	2
A3	413	435	393	433	22	3.3
A4	431	451	386	437	20	3.8
B1	424	443	387	433	19	4.8
B2	483	499	355	–	16	4.9
B3	484	523	349	–	39	5.1

transformation and the Curie temperature of the austenite, leading to the incomplete cycle observed.

In the case of the B series these two behaviors can be also distinguished, however, for the samples B1 and B2 only ${T_C}^M$ can be observed as the martensite transformation falls in the paramagnetic regime. These results are in agreement with the T_M temperatures determined by DSC.

To correlate the change of the transformation and Curie temperature with the effect of Cu addition, the results were plotted for both series in Figure 3.13.

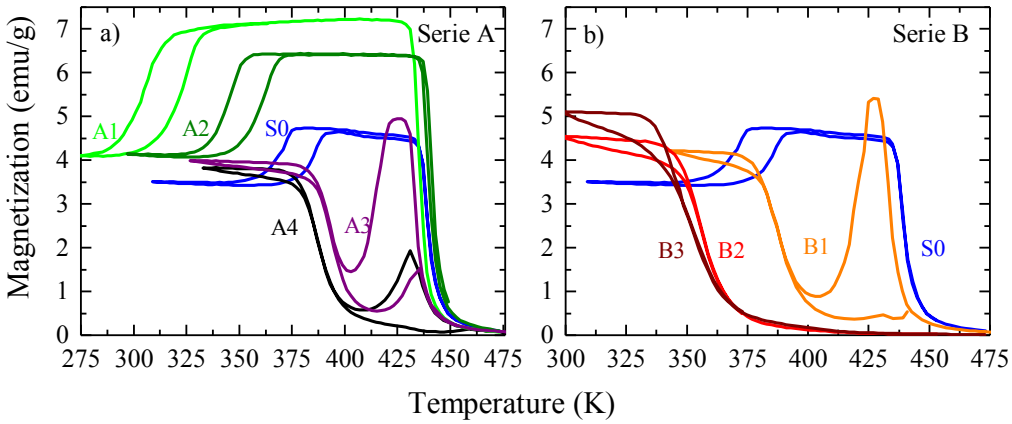

Figure 3.12: Temperature dependences of the magnetization in a magnetic field of 0.01 T for the A (a) and B series (b).

Figure 3.13 shows the strong influence of small amounts of Cu on the martensite and magnetic transformation temperatures. Especially, T_M depends dramatically on the Cu content and on whether it substitutes Mn or Ga. In the A series, when Cu substitutes Mn, Cu increase, from 7.0 to 7.5 at.%, leads to a drop of both T_{af} and T_{ms} by about 60 K, followed by an increment of 80 K during the further 0.5 at.% increase. Such a deep minimum is entirely replicated by the c/a ratio. In contrast, both ${T_C}^A$ and ${T_C}^M$, exhibit a slight linear decrease with Cu content. For the B series, as Cu substitute Ga, the dependence of T_M with Cu content shows a continuous and strong increase, e.g., T_{af} rises from 393 K (S0) to 523 K (B3). The tendency of the ${T_C}^A$ values is similar to that of A series, but ${T_C}^M$ exhibits a larger rate of nonlinear decrease.

Such strong and simultaneous changes in T_M and c/a ratio by the substitution of Cu by Mn or Ga can be explained in terms of the stabilization/destabilization of the tetragonal martensite phase through enhancing/decreasing the covalent-like bonding strength of the Ga–Ni and Ga–Mn pairs, tailored by the lattice distortion induced by Cu.[92–95] Moreover, in this case, the changes of the interatomic distances intensify the antiferromagnetic interactions in the martensite phase, which can lead to the significant change in ${T_C}^M$, as observed.

By plotting both series together it is possible to compare the influence of the Mn/Ga ratio variation on T_M and T_C. Figure 3.14 depicts the characteristic temperatures for all the samples as a function of Cu. Sample S0 is marked with cross,

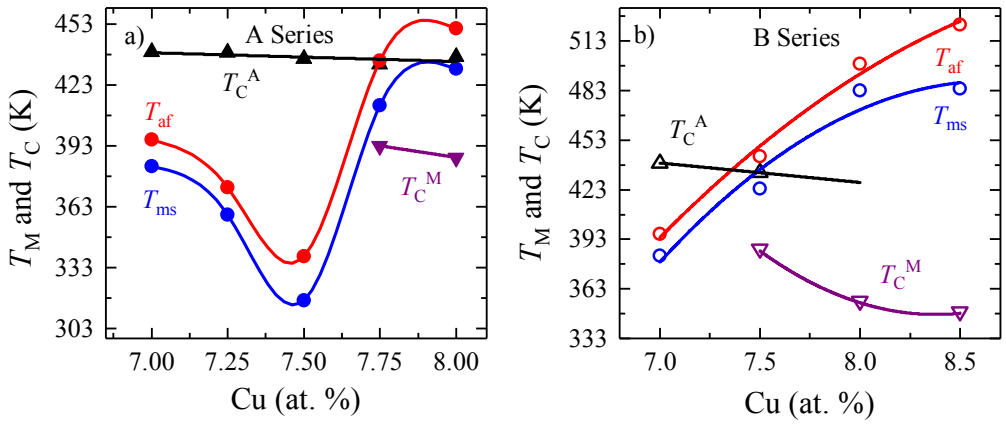

Figure 3.13: Concentration dependences of the transformation temperatures for the two series: (a) A series (solid symbols) and (b) B series (open symbols). The lines are guides for the eye.

while A and B series are marked with close and open symbols respectively. The black arrows indicate the Mn/Ga variation.

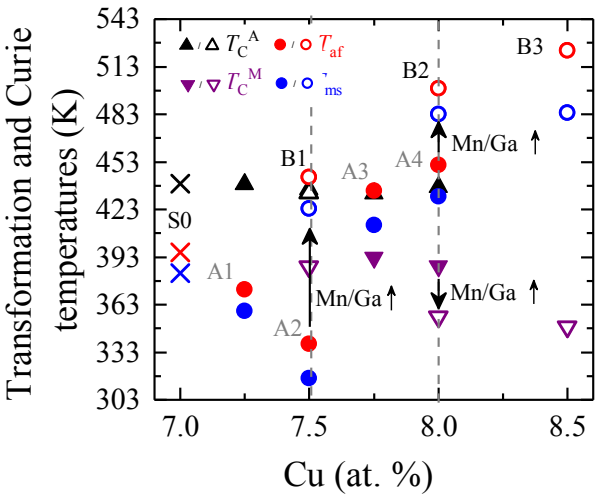

Figure 3.14: Transformation and Curie temperatures for A (solid symbols) and B series (open symbols). The black arrows indicate the Mn/Ga ratio variations for the samples with the same Cu content.

As seen in this Figure, the pairs of samples B1/A2 and B2/A4 with the same Cu content have, however, a variation on the Mn/Ga ratio with respect to each other. In both cases, the increase of the Mn/Ga ratio produces an increase on T_M and a

decrease on T_C.

3.4.3 Correlation between structure and properties

A similar behavior of c/a and T_M in A and B series have been observed, and thus, a correlation between both parameters must be analyzed.

The dependence of the tetragonal unit cell parameters, c and a, as well as c/a ratio, are plotted for both series in Figure 3.15 as a function of the T_M temperature $T_0 = (T_{ms} + T_{af})/2$. These plots show a considerable influence of T_0, particularly, on the c axis, which increases from 6.406 Å to 6.577 Å for alloys A2 and B3 respectively. The variation of c/a with T_0 shows a much lower curvature, and can be approximated as almost a linear increase.

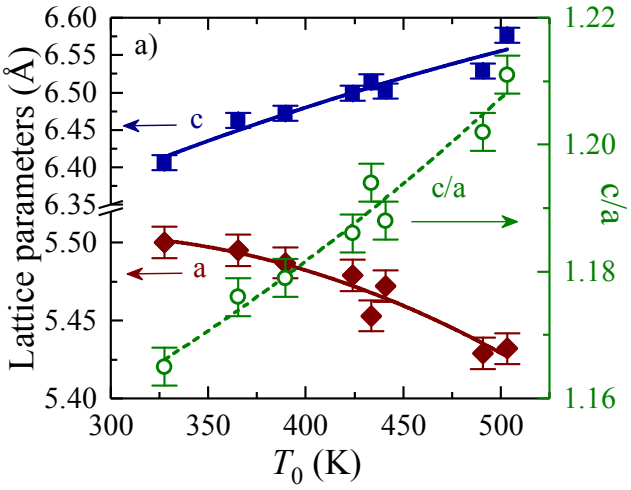

Figure 3.15: Room temperature tetragonal lattice parameters, c and a, as well as c/a ratio versus $T_0 = (T_{ms} + T_{af})/2$ for all the alloys.

As was already mentioned, in both series the c/a ratio at room temperature shows the same dependence on Cu content that the T_M temperatures do. The main results of the present study are found in Figure 3.16, which shows the T_M and Curie temperatures as a function of the c/a ratio for all alloys studied.

Two observations need to be highlighted. First, an intrinsic relation between c/a and the transformation behavior, reflected in the strong, almost linear increase of T_M temperature, and the quite marked linear decrease of ${T_C}^M$ with increasing c/a. ${T_C}^A$ however, remains unchanged. Second, the two series show a similar behavior as a function of c/a revealing no direct dependence of the parameters mentioned on

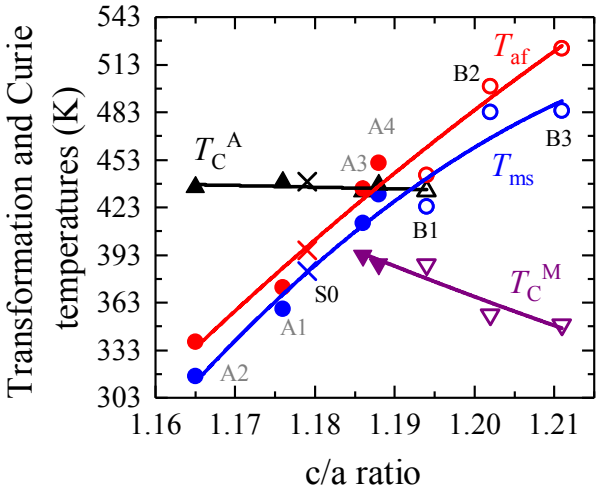

Figure 3.16: Martensitic transformation (T_{ms}, T_{af}) and Curie ($T_C{}^M$, $T_C{}^A$) temperatures as a function of the tetragonality ratio, c/a, for all the samples of A series (solid symbols) and B series (open symbols), as well as for alloy S0 (crosses). The lines are guides for the eye.

the amount of Cu or the species it substitutes. Similar relations have been obtained for the influence of the Fe doping in the $Ni_{45}Co_5Mn_{25-x}Fe_xGa_{20}Cu_5$ system.[96] The correlation between the evolution of the T_M temperature and c/a as a function of Cu, identified in the present work, suggest a strong influence of the unit cell distortion on the thermodynamic stability of the alloys as well as on their magnetism. This might be due to a high sensitivity of the latter to the interatomic distances. The influence of the c/a ratio on $T_C{}^M$, observed in the present work, is consistent with the explanations presented in References.[90,94,95,97–99]

3.5 Summary and Conclusions

We have studied the composition and temperature dependencies of the transformation, structural and magnetic properties of three Ni–Mn–Ga–(Co, Cu, Fe) polycrystalline series.

In the $Ni_{45}Co_5Mn_{25-x}Fe_xGa_{20}Cu_5$ series, the increase of Fe content dramatically increased the Curie point and decreased the martensite transformation temperatures. The Curie temperature of the martensite, $T_C{}^M = 458$ K, for the alloy Fe4 was estimated by using an alternative method based on Arrott plots.

Additionally, XRD structure analyses at room temperature have shown a non-

modulated (NM) tetragonal structure with c > a=b, without evidence a second phase precipitation for Fe content up to 6 at.%. A mixture of austenite and martensite phases was obtained for the Fe8 alloy.

The high values of ${T_C}^M$ and ${T_C}^A$ together with the increase of saturation magnetization as a function of Fe content suggest an appearence of enhanced magnetostress under magnetic field application, whereby reinforcing the feasibility of giant MFIS in these alloys.

We also analyzed the effect of replacing small amounts of Mn or Ga by Cu on the T_M, T_C and on the crystallographic structure for two multicomponent Ni-Mn-Ga-(Co, Fe, Cu) alloys series. The substitution of Ga by Cu leads to a rapid increase of the T_M and the c/a ratio, and a decrease of the ${T_C}^M$. On the other hand, the substitution of Mn is rather different, exhibiting a minimum in the T_M temperatures and the c/a at 7.5 at.% Cu. In this way, a universal relation between the crystal structure, T_M, and T_C for two different multicomponent systems has been presented, enabling a comparison between both series without considering the type or amount of Cu substitution in the range studied.

By comparing the relation between the structure and c/a for all the samples studied with published compositions for the Ni–Mn–Ga system an additional result was obtained. Figure 3.17 shows the evolution of c/a as a function of T_0 for the Ni–Mn–Ga compositions published by Lanska et al.[1] and our Fe and Cu series respectively. The two lines do not imply a linear relation and were drawn simply as a guide for eye. As it was mentioned before there is a strong relation between structure and martensite transformation, however, the composition also plays an important role. From this figure it can be seen that the simultaneous use of Fe, Co and Cu leads to a reduction of the c/a without a decrease in T_M, in contrast to the base ternary system. This fact demonstrate that the use of additional elements becomes an interesting and promising field of study for developing new high temperature ferromagnetic shape memory alloys.

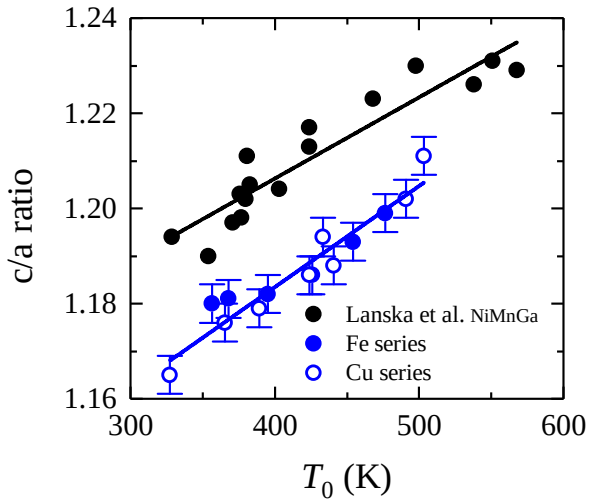

Figure 3.17: Tetragonality ratio dependence on the transformation temperature (T_0) for the studied series, Fe (solid blue circles) and Cu (open blue circles), and data from Lanska et al.[1] relative to the ternary compositions of NiMnGa alloys (black circles).

Finally, among the materials studied here, three alloys, S0, Fe4 and Fe5, are found to exhibit simultaneously high values of T_M and $T_C > 373$ K and 423 K respectively. Bearing in mind the expected reduction of c/a near the T_M, these three alloys are the best candidates for the observation of high temperature magnetostrain. Thus, the present work is an important step in the development of high temperature FSMA materials. The magnetic field induced strain in these materials will be possible after they are grown as single crystals.

Chapter 4

Neutron studies of the relation between structure and magnetism

4.1 Introduction

Since the discovery of the ferromagnetic shape memory alloy system based on Ni_2MnGa, a wide interest has arisen due to the strong coupling between the structure and the magnetic properties it exhibits. Several neutron studies have been performed to understand the structural changes that occur during the martensitic transformation and elucidate the chemical order in the off-stoichiometric compositions as well as its influence on the magnetic properties.[100–106]

The problem of determining the magnetic moments and exchange coupling in these materials and its relation with the atomic positions and interatomic distances has been engaged through theoretical calculations,[107,108] and experimentally by polarized neutrons.[109,110] However, this challenge has not been yet analyzed for a more complex multicomponent system as the ones described in this thesis.

The use of unpolarized and polarized neutrons comprises the main, and seemingly the sole, technique to determine the spin density distribution, and reveal the atomic order in these systems. In this chapter, the chemical order and its influence on the magnetic properties are analyzed for the polycrystalline samples of the Fe serie ($Ni_{45}Mn_{25-x}Ga_{20}Co_5Cu_5Fe_x$, where x = 0, 1, 2, 5, 6, 8) studied in the previous chapter. Additionally, a quantitative estimation of the site-specific magnetic moments has been done in a single crystal of Fe5, by polarized neutrons' scattering.

Before delving into the analysis of the neutron diffraction results, it is worth spending some time discussing some of the concepts related to the diffraction techniques. One of the main equations that mathematically describes the the phenomena of neutrons being scatterd by a crystalline solid is the structure factor, which is the Fourier transform of the unit cell scattering potential. The structure factor is described with the following expression:

$$F_{hkl} = \sum_j b_j e^{2\pi i(hx_j + ky_j + lz_j)} \tag{4.1}$$

where b_j is the scattering length, (equivalent to f, atomic form factor for X-rays), and x_j, y_j and z_j are the coordinates of the j atoms in the unit cell. Considering the rules of allowed reflections in a $L2_1$ structure and the atomic positions of a stoichiometric Ni–Mn–Ga structure, described in the Chapter 1, the structure factor of 3 different types of planes can be expressed by the scattering length (or nuclear form factor) of the different atoms involved. An example of the calculation for a (111) hkl is shown in equations 4.2, 4.3 and 4.4:

$$F_{111} = \sum_{Mn} b_{Mn} e^{2\pi i(x+y+z)} + \sum_{Ga} b_{Ga} e^{2\pi i(x+y+z)} + \sum_{Ni} b_{Ni} e^{2\pi i(x+y+z)} \tag{4.2}$$

$$F_{111} = 4b_{Mn} e^{2\pi i} + 4b_{Ga} e^{2\pi i(\frac{3}{2})} + 6b_{Ni} e^{2\pi i(\frac{7}{4}))} + b_{Ni} e^{2\pi i(\frac{9}{4}))} + b_{Ni} e^{2\pi i(\frac{3}{4}))} \tag{4.3}$$

$$F_{111} = 4b_{Mn} - 4b_{Ga} \tag{4.4}$$

The calculated structure factors for the different types of planes together with the order type are summarized in Table 4.1. As seen in this table, the intensity of the all odd Miller indices will be determined by the difference of the scattering length between Mn and Ga atoms. Therefore in a B2 structure in which Mn and Ga sites are interchangeable these reflections are absent. In the case of all even hkl, two different cases are observed depending on the sum of the hkl were a multiple of 2 or 4. In the first case, which corresponds to the B2 reflections, the intensity will be proportional to the difference between $4b_{Mn}$–$4b_{Ga}$ and $8b_{Ni}$, and, in the second case to the sum of all the atoms' scattering lengths.

Accordingly, the reflections that will have strongest intensity will be the fundamental ones, in comparison with the characteristic ones of the B2 and $L2_1$ structures.

Table 4.1: Miller indices, hkl, structure factors, F_{hkl}, and type of order for the different family of planes

Type	Miller Indices	Example	Fhkl	Order type
I	(hkl) all odd	(111)	$4b_{Mn}$ - $4b_{Ga}$	$L2_1$
II	(hkl) all even h+k+l=2n	(200)	$4b_{Mn}$ + $4b_{Ga}$ - $8b_{Ni}$	B2
III	(hkl) all even h+k+l=4n	(220)	$4b_{Mn}$ + $4b_{Ga}$ + $8b_{Ni}$	Fundamental

Another factor that distinguishes neutrons from X-ray is their type of interaction with the atoms in the mesh. X-rays interact with the electron clouds and consequently the scattering amplitude of X-rays increases with the atomic number, Z, of the atoms. As a result X-rays are not very sensitive to light atoms and have a weak contrast between elements with similar Z value, which is the case of the Ni–Mn–Ga system. Additionally, as X–rays interact with the electron clouds, the atomic form factor decays with the scattering vector. On the contrary, due to the neutron–nucleus interaction, the scattering amplitude of the neutrons is independent of Z, being different even for different isotopes, as was demonstrated by Shull et al.[111] in their early works that would later on earn them the Nobel price for neutron diffraction.

Taking into account that the chemical order is determined by the relation of the structure factors and the atomic species, the similarity between the atomic form factors of Ni, Co, Mn, Fe, Ga and Cu makes it extremely difficult to obtain information about the site occupancy using X–ray radiation. However, the coherent neutron scattering lengths of these atoms are very different, as shown in Table 4.2, making possible the study of the chemical order by neutron diffraction.

4.2 Experimental Part

In this section, two types of samples were used, namely powder samples made by crushing polycrystal alloys and a single crystals grown from the Fe5 alloy.

The powder samples were obtained from the master rods produced in the previous chapter. The powder was obtained by hand milling the master rods and subsequent

Table 4.2: Coherent scattering length (fm) for all the atoms presented in the samples studied according to NIST Center for Neutron Research (ncnr).

Atom	scattering length (fm)
Ni	10.3
Mn	-3.73
Ga	7.288
Fe	9.45
Co	2.49
Cu	7.718

heat treating at 923 K during 2h to relieve the stress caused by the milling process.

The single crystal was grown using a modified Bridgman-Stockbarger method under 0.2 bar pressure of 99.98% Ar, as described in appendix A. The crystal was heat-treated under argon at 1223 K for 24 h followed by cooling during 1 h to 723 K and holding for 4 h to promote a $L2_1$-type atomic order. Rectangular specimens ($\approx$ 3 x 3 x 4 mm^3) were cut by abrasive wire saw from the rods. The single crystal prisms were mechanically and electrochemically polished to remove the surface atomic layers stressed by the mechanical polishing.

In this chapter an in-depth characterization of the crystallographic structures and their influence on the magnetic properties will be carried out. The bulk magnetic properties of the alloys were determined using the in-house built VSM described in appendix B.4.1. The saturation magnetization was obtained from magnetization loops measured up to 2 T at different temperatures.

The crystallographic analysis was carried out using a combination of X-ray and neutron diffraction techniques. For the X-ray measurements the UPV/EHU's shared facility Philips X'Pert, MPD diffractometer with CuKα radiation was used. Neutron diffraction experiments were performed at the Institute Laue-Langevin (Grenoble, France). For the powder samples, the measurements were carried out on the D1B diffractometer. In the case of the single crystals two different instruments were used: the Hot neutron four-circle diffractometer (D9), using a wavelength of λ = 0.5 Å, to obtain the pure nuclear contribution and the Spin Polarised Hot Neutron Beam Facility (D3), with a wavelength of λ = 0.85 Å, to obtain the magnetic contribution of the atoms located at the different lattice positions.

4.3 Polycrystalline neutron diffraction

4.3.1 Structural analysis and chemical order

X-ray diffraction measurements were used for a preliminary characterization of the samples before and after heat treatment to ensure that stresses from the milling had been removed and that no drastic changes in the structure had occurred, because time for neutron measurements is quite limited and should be reserved for samples that could show good results.

The patterns of the alloys with an Fe content lower than 6% exhibit a peak width reduction which is related to the release of internal stresses. However, in the alloys with an Fe content higher than 6% the appearance of a second phase after the heat-treatment was observed. Sample Fe4 was contaminated during the powder production was removed from the analysis.

As a representative example of the results obtained from XRD, Figure 4.1 shows the room temperature diffraction patterns for sample Fe6 before (blue line) and after heat-treatment (red line). The phase obtained in both cases was indexed as a non-modulated tetragonal martensite with an I4/mmm symmetry group. The hkl indices were given according to the cubic coordinates. The extra reflection visible in the heat-treated sample corresponds to a second phase and is indicated with an asterisk.

Thus, in order to simplify the further analysis of the chemical order and avoid the appearance of second phases, the samples with an Fe content greater or equal to 6% were measured by neutrons in as-crushed condition, while the rest of the samples were measured in the heat-treated state.

Neutron powder diffraction measurements were performed in a temperature range from 250 to 540 K. Data was collected during the full temperature range, however, long time measurements were performed at the specific temperatures corresponding to the paramagnetic and ferromagnetic martensite and austenite phases. A wavelength of $\lambda = 1.28$ Å was selected to obtain a full spectrum instead of focusing on the low or high angles. The data were analyzed by pattern matching analysis and Rietveld refinement using the Fullprofsuite software.[112]

Figure 4.2 depicts X-ray and neutron diffraction patterns for sample Fe1 mea-

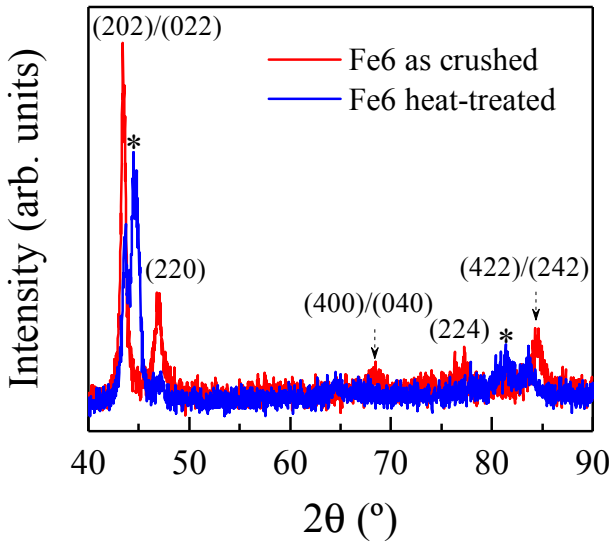

Figure 4.1: Room temperature X-ray powder diffraction measurements (CuK_α) of the sample Fe6 as-crushed and heat-treated. Intensities have been scaled. Miller indices are given in the cubic coordinates. The reflections indicated with an asterisk in the heat-treated sample correspond to a second phase.

sured at 393 K in the martensite phase. To compare both measurements, the 2θ scale, which is dependent on the wavelength of the radiation used, was converted to interplanar spacings, which is independent on it. All the reflections observed in the X-ray pattern correspond to fundamental hkl reflections. However, in the neutron diffraction patterns the intensities of the first two reflections, $L2_1(111)$ and B2(200), which are critical for the atomic order determination, are clearly observed. This fact is in agreement with the different structure factors calculated for the distinct types of Miller indices.

A preliminary refinement by pattern matching analysis was performed to determine the lattice parameters and crystallographic structure of the alloys. This analysis takes into account the position of the reflections but does not consider the atomic occupancies, and consequently the intensity of the reflections is ignored.

All the samples measured in the martensite phase show a non-modulated tetragonal structure with an I4/mmm symmetry group, in agreement with the previous X-ray results from Chapter 3. However, in the austenite phase some differences were observed.

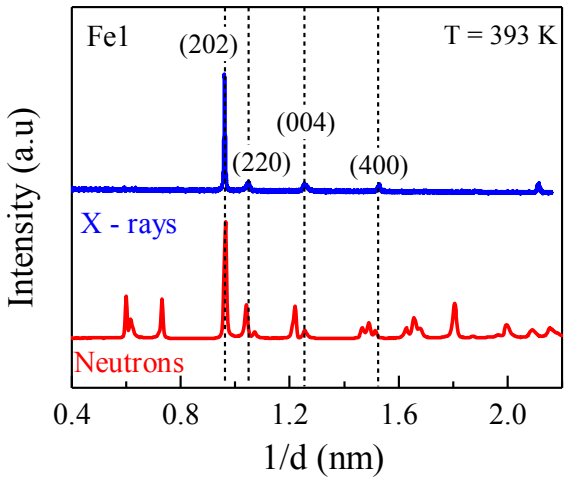

Figure 4.2: Diffractograms obtained for the sample Fe1 at 393 K by neutron and x-ray diffraction techniques. The intensities were normalized for an easy comparison between them. Indices are given according to the cubic coordinates.

Figure 4.3 shows the diffraction patterns of the samples Fe0 (heat-treated) and Fe6 (non heat-treated) measured at 540 K, chosen as representative examples. The Miller indices are placed above each peak. The heat-treated samples with Fe content below 6%, as observed in Figure 4.3 (a) show well defined austenite with sharp reflections, that correspond to a $L2_1$ structure. In the case of the samples with more than 6% Fe two different features were observed. On the one hand, the lack of heat treatment resulted in peak broadening, especially at higher angles. The broad shapes of the peaks are indicated in Figure 4.3 (b) by a red circle. And second, additional reflections appear as shoulders of the main ones. These reflections are marked with asterisks.

In order to identify the additional phase observed, the evolution of the diffraction patterns was followed by measuring continuously as the temperature was increased through the transformation. Figure 4.4 shows selected diffraction patterns measured at different temperatures for the sample Fe6. The dashed lines show the evolution of the martensite reflections with the temperature. By following the black dashed lines it is possible to see that the shoulders observed at the high temperature pattern belong to a non-transformed martensite with lattice parameters close to the ones of the cubic phase.

The lattice parameters of the samples studied in the ferromagnetic martensite

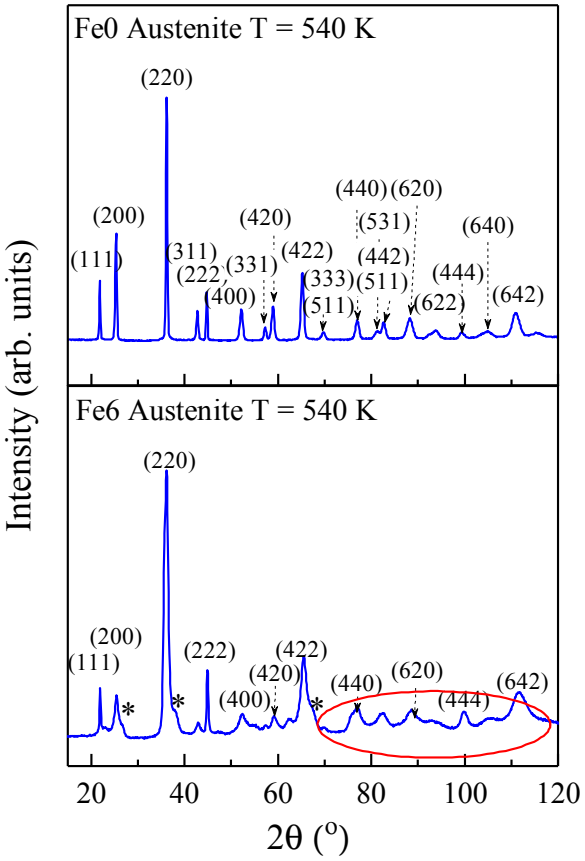

Figure 4.3: Powder neutron ($\lambda = 1.28$ Å) diffraction of the samples Fe0 (heat-treated) and Fe6 (non heat-treated) measured at 540 K. Intensities have been scaled. For an explanation of the asterisks and red circle see the text.

were obtained at 250 K, and the ones in the paramagnetic austenite at 540 K. The selection of these temperatures was motivated by the existence of ferromagnetic martensite and paramagnetic austenite phases at these exact temperatures for all the samples presented here. The results are shown in Table 4.3.

The lattice parameters obtained for the non heat-treated samples Fe6, and Fe8, indicated by asterisks, were obtained by considering a mixture of martensite and austenite phases. The presence of retained martensite at temperatures above T_M could be related to the presence of inhomogeneities in the samples due to the lack of heat treatment.

The errors obtained as a result of the fitting of the lattice parameters are one order

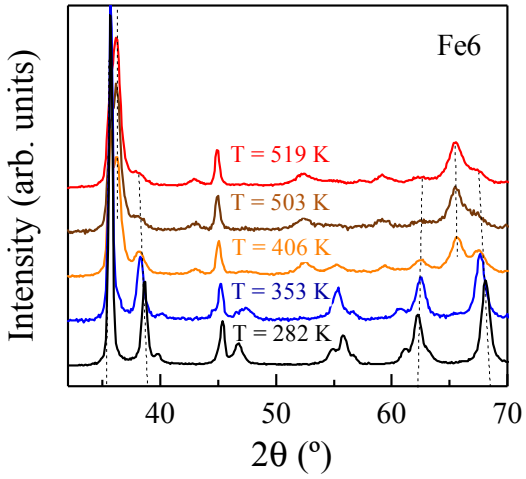

Figure 4.4: Selected powder neutron diffraction patterns of the samples Fe6. Intensities have been scaled. The dashed lines indicate the peak spliting due to the symmetry reduction from austenite to martensite phases during the transformation.

Table 4.3: Lattice parameters for the martensite (250 K) and austenite (540 K) phases together with the fitting errors. The asteriks indicate the values obtained by fitting a coexistance of martensite and austenite structures.

Sample	lattice parameters (Å)				
	Martensite (250 K)			Austenite (540 K)	Fitting Error
	a_{Mart}	c_{Mart}	c/a		
Fe0	3.847	6.531	1.200	5.809	0.0001
Fe1	3.852	6.506	1.194	5.807	0.0001
Fe2	3.854	6.486	1.190	5.802	0.0001
Fe5	3.857	6.455	1.183	5.796	0.0001
Fe6*	3.860	6.440	1.180	5.774*	0.001
Fe8*	3.869	6.399	1.170	5.753*	0.002

of magnitude higher for the non heat-treated samples. These errors are attributed to the peaks widening and the low quality of the diffraction patterns obtained.

Thus, the two sets of samples, heat-treated and non heat-treated cannot be directly compared, as the presence of inhomogeneities in the second case may lead to slight variation of the lattice parameters. However, similar trends are observed for both set of samples, in which an increase of the a_{Mart} (short axis) and a decrease of c_{Mart} (long axis) of the martensite phase are obtained with the addition of Fe.

Additionally, the lattice parameter for the austenite phase decreases with Fe content.

For all the samples studied, lattice parameters as a function of temperature were determined from the neutron diffraction patterns measured from 250 K to 540 K. Figure 4.5 (a) shows the temperature dependent evolution of the lattice parameters. The parameters of the martensite, c_{Mart} and a_{Mart}, are shown as half-opened and full-opened circles for the heat-treated and non heat-treated samples respectively; and the austenite ones, a_{Aus} as filled circles. From this figure a decrease of the c_{Mart} and an increase of the a_{Mart} as a funtion of the temperature can be observed. The variation is larger for the c_{Mart}. Additionally, the linear increase with the temperature observed for the a_{Aus} parameter, is related to the thermal expansion coefficient of the austenite phase. Another parameter which can be obtained from these measurements is the c/a ratio. As it was mentioned in previous chapters, c/a determines the maximum deformation achievable, ϵ_{max} for an alloy, according to the following expresion:

$$\epsilon_{max} = 1 - \frac{a}{c} \tag{4.5}$$

Thus, in order to get large magnetic field induce strain, MFIS, large value of c/a is desirable. It is also known that the twinning stress in Ni-Mn-Ga alloys increases with increasing c/a ratio.[24] Additionally, as mentioned in the previous section, large magnetostress values are also related to this parameter[113] by the equation 3.2.

Figure 4.5 (b) depicts the temperature dependence of the c/a ratio for all the samples studied. A reduction of the c/a can be observed as a function of both, the temperature and the addition of Fe. The decrease of c/a ratio with temperature can be explained by the convergence of the tetragonal structure to the cubic austenite phase (c/a = 1) near T_M, minimizing the distortion linked to the transformation.[114] The tendency observed with the addition of Fe and consequently with the T_M is in agreement with previous results reported for the Ni–Mn–Ga system.[1] The low values of c/a $\approx$ 1.16 obtained near the transformation temperatures for the samples with a high Fe content makes these samples promising candidates for exibiting MFIS.

With the aim of understanding the effect of Fe addition on the transformation temperatures, magnetic properties and crystallographic structure, a deep analysis of the chemical order is needed. Thus, Rietveld refinements of the austenite and martensite structures were performed for the heat-treated samples. The refinement

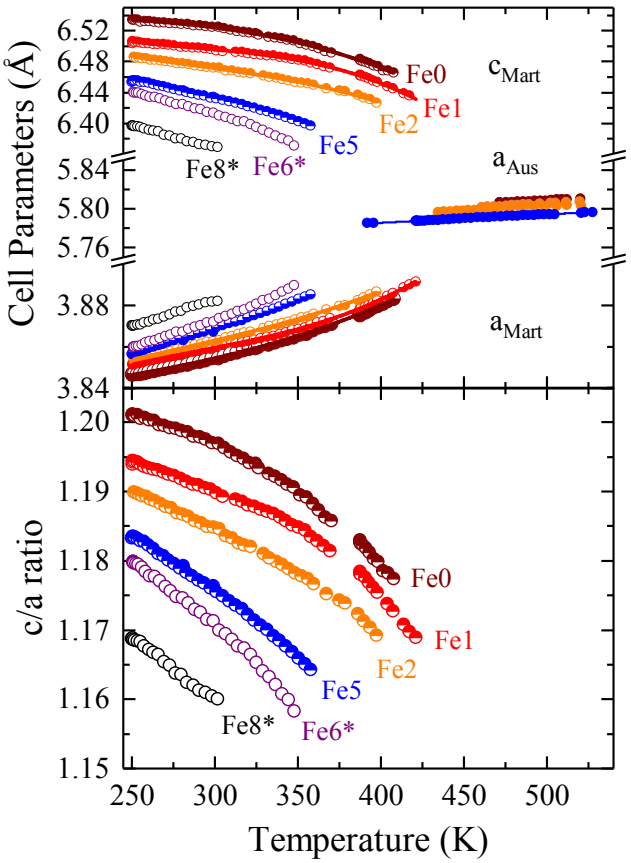

Figure 4.5: (a) Temperature evolution of the lattice parameters for the samples studied. The half-opened circles correspond to the c_{Mart} and a_{Mart} parameters of the martensite structure, and the full circles to the a_{Aus} of the austenite structure. (b) Evolution of the c/a ratio as a funtion of temperature for the studied samples.

for the non heat-treated ones was impossible due to the low quality of the neutron diffraction patterns obtained.

An initial analysis of the austenite phases above T_C was performed to obtain the pure nuclear contribution in absence of magnetic scattering peaks. Also, the preliminary analysis of the austenite phase facilitates further studies of the martensite one, because the transformation is diffusionless and the relative atomic positions are the same for both phases. The analyses were performed starting from the pattern matchings calculations mentioned before, and adjusting the site occupancies and thermal parameters of the different atoms according to the compositions measured by

EDX. The paramagnetic austenite and paramagnetic martensite refinements for the sample Fe1 can be seen in Figure 4.6 (a) and (b) respectively. The tetragonal splitting expected due to the symmetry reduction during the transformation is observed. No additional reflections indicating modulation appear in the martensite phase. The hkl indices are indicated above the peaks for both phases. Due to the complexity of the martensite structures higher fitting error were obtained for this phase in all cases.

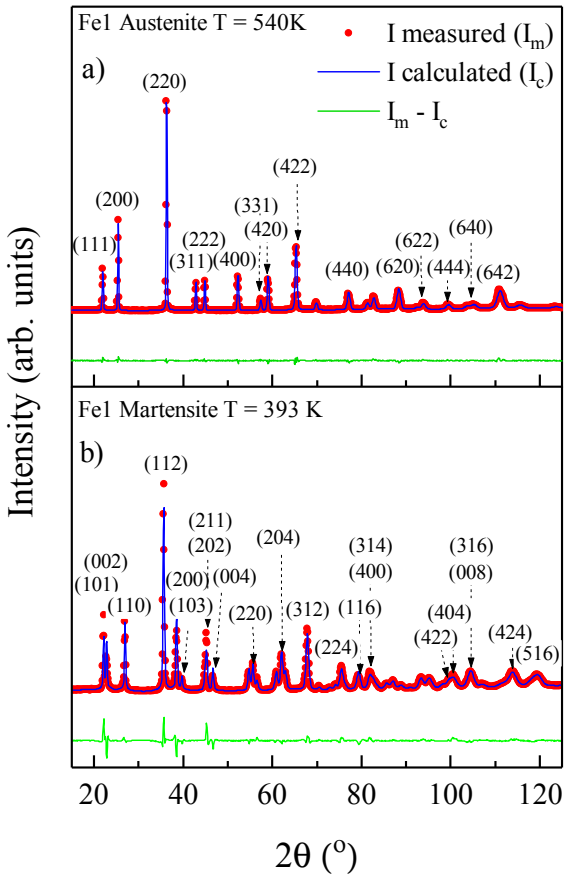

Figure 4.6: Diffraction patterns of the austenite (a) and martensite (b) phases for the sample Fe1. The measured intensity (red dots) and the calculated one using Rietveld refinement (blue line), together with the difference between both intensities (green line) are indicated.The agreement factors are Rp = 2.21%, Rwp = 3.15% (top) and Rp = 4%, Rwp = 6.52% (bottom)

As a first approximation, Ni and Ga atoms were kept in their own positions while Mn was placed also in Ni and Ga sites, in agreement with previous results

for Ni–Mn–Ga alloys.[102,115] In those works they studied the preferential atomic order for off-stoichiometric Ni–Mn–Ga alloys with a large range of Ni concentrations (44–52 at.%), obtaining for Ni-deficient alloys, that Mn atoms occupy both Ni and Ga sites. Regarding the additional elements, the site preference occupation of Co for Ni sites, Cu for Ga sites and Fe for Mn and Ni sites were considered based on literature review.[66,71] However, the errors obtained with these assumptions were not acceptable. In a second approach, the Ni, Mn and Ga atoms, were placed as in the previous case, but the additional elements were arranged in the three positions. The results of the final refinement based on the second approach are shown in Table 4.4.

Table 4.4: Site occupancies calculated for the heat-treated polycrystalline samples for the $L2_1$ structure obtained by Rietvelt method. Errors are indicated in brackets.

Alloy	Site (Wyckoff)	Ni	Mn	Ga	Fe	Co	Cu	Total
Fe0	Ni (8c)	1.80(4)	0.10(6)	0	0	0.09(0)	0	2
	Mn (4a)	0	0.79(2)	0	0	0	0.208	1
	Ga (4b)	0	0.11(4)	0.78(4)	0	0.10(2)	0	1
Fe1	Ni (8c)	1.78(8)	0.11(4)	0	0.05(6)	0.04(2)	0	2
	Mn (4a)	0	0.78(4)	0	0	0	0.21(6)	1
	Ga (4b)	0	0.07(0)	0.78(0)	0	0.15(0)	0	1
Fe2	Ni (8c)	1.79(2)	0.08(6)	0	0.1(0)	0.02(2)	0	2
	Mn (4a)	0	0.78(0)	0	0	0	0.22	1
	Ga (4b)	0	0.04(2)	0.78(8)	0	0.17(0)	0	1
Fe5	Ni (8c)	1.80(0)	0.02(4)	0	0.17(6)	0	0	2
	Mn (4a)	0	0.73(2)	0	0.04(8)	0	0.22(0)	1
	Ga (4b)	0	0.04(4)	0.76(8)	0	0.18(8)	0	1

These results show a clear tendency for Cu to occupy positions in the Mn lattice, while the preference of Co and Fe varies with the concentration of Fe. For the alloy Fe0, Co is distributed among Ni and Ga sites together with Mn atoms. As Fe content increase up to 2%, Fe tends to occupy sites on the Ni and Mn lattice and Co is displaced more to Ga sites. At a certain amount of Fe, namely 5%, Fe occupies both Ni and Mn sites while Co is mainly relegated to the Ga positions. The preference of Co for Ni and Ga sites together with the amount of Fe in Ni sites leads to an increase of the number of Mn atoms in their proper sites. Thus, the total amount of Mn out of its proper poition is reduced from 5.5% (0.22) for Fe0 to 1.7% (0.068) for Fe5.

4.3.2 Influence of the structure and chemical order on magnetism

In this section, the increase of the saturation magnetization with Fe addition observed in Section 3.3.3 is analyzed by means of the structure and chemical order.

In the Ni–Mn–Ga Heusler alloys, Mn is the main contributor to the alloy's magnetism. In previous studies it was reported that the magnetism is mainly dominated by the indirect exchange through a Ruderman, Kittel, Kasuya and Yoshida (RKKY) type of interactions between the Mn localized magnetic moments mediated by conductive electrons.[116,117]

In off-stoichiometric compositions with a deficit of Ni and/or Ga and an excess of Mn, Mn tends to occupy Ni and/or Ga sites,[102,115] becoming nearest neighbors and leading to variations in the interatomic Mn–Mn distances.[105,118] Recently, Lázpita et al.[119] systematically studied the influence of the variation of Mn–Mn interatomic distances on the exchange interaction. In this publication, a switch from a ferromagnetic to antiferromagnetic coupling in the Mn–Mn pairs was observed when changing the distance between them from 3.32 to 2.92 Å. This behavior was explained according to the Bethe-Slater curve which represents the direct exchange interaction as a function of the interatomic distance. Figure 4.7 shows an schematic of the Bethe-Slater and RKKY exchange interaction curves. In the case of Mn, the magnetic exchange interaction changes from ferromagnetic at large distances to antiferromagnetic at short ones. The behavior is similar in the case of an indirect RKKY exchange for this range of interatomic distances observed in the Heusler alloys.[115]

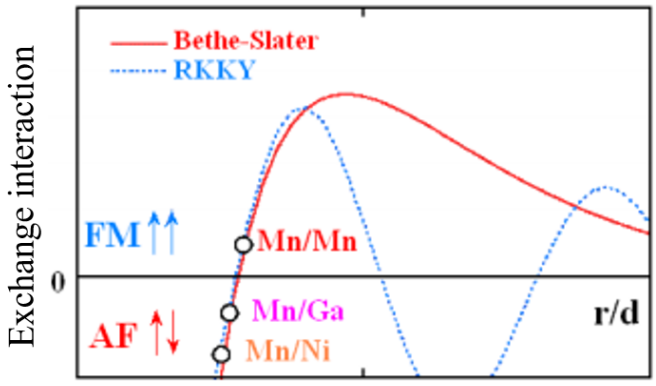

Figure 4.7: Schematic representation of the Bethe–Slater and Ruderman– Kittel–Kasuya–Yosida (RKKY) exchange interaction curves, showing the different types of magnetic coupling that arises as the distance between Mn atoms changes. Figure is taken from Lázpita et al.[115]

Our results for the Fe series shows an increase of up to 20% of the magnetic moment with Fe addition. These results can be analyzed by looking at the variation of the Mn–Mn distances. In the previous section the atomic site occupation of the alloys up to a 5% of Fe was discused. These results revealed that Mn atoms occupy the three different sites, however their proportion on each site depends on the amount of Fe.

Considering the cubic and martensite structures, all the posible Mn–Mn distances were calculated for the samples up to 5%. In the case of the cubic phase, the Mn_{Mn}-Mn_{Mn} nearest neighbors are separated by a value of $\frac{a\sqrt{2}}{2}$ equal to 4.11 and 4.10 Å for the Fe0 and Fe5 respectively. For the Mn_{Ga}-Mn_{Mn} the interatomic distance is $\frac{a}{2}$, being 2.91 (Fe0) and 2.90 (Fe1) Å, and for the Mn_{Ni}-Mn_{Mn} is $\frac{a\sqrt{3}}{4}$, which is 2.52 (Fe0) and 2.51 (Fe5).

Taking into account the distances reported by Lázpita et al.,[119] it is plausible to consider that the Mn_{Ga}-Mn_{Mn} and Mn_{Ni}-Mn_{Mn} may exhibit an antiferromagnetic coupling. The variation in the interatomic distance between the different alloys is consistent with the atomic order variation, however, this small change cannot explain the huge increase of the magnetism. As was discussed in the previous section, the addition of Fe and Co tends to retain the Mn into its proper site, reducing the amount of antiferromagnetic contributions, and leading to an increase of the magnetic properties.

In the case of the martensite phase, it is even more complex as four different interatomic distances can be distinguished, however the effect of the atomic order on the magnetic moment is similar. For the martensite the Mn_{Mn}-Mn_{Mn} are located at a distance of a', which is 3.85-3.86 Å, and should be ferromagnetically coupled; and for the Mn_{Ni}-Mn_{Mn} the distance is defined by $\sqrt{\frac{c^2}{16}+\frac{a'^2}{4}}$, being 2.52-2.51 Å, so the atoms should be coupled antiferromagnetically. However, in the case of Mn_{Ga}-Mn_{Mn} interaction the Mn_{Ga} atoms are surrounded by two Mn_{Mn} atoms at $\frac{c}{2}$ distance, with values of 3.27-3.23 Å and four Mn_{Mn} atoms at $\frac{a'\sqrt{2}}{2}$, which is equal to 2.72-2.73 Å. Taking into account these two distances it can be considered that when the distance between the Mn atoms is close to 2.72 Å, they present a negative magnetic exchange interaction, whereas at a distance of 3.27 Å it is positive.

This assumption implies that all the possible interactions between Mn and other magnetic atoms, Co, Ni or Fe are ferromagnetic. Additionally, the effect of Fe on improving the ferromagnetic effect or the influence of Co and Cu on the spin-orbit coupling should be also considered. However, in this complex system further inves-

tigations must be performed to fully understand the contribution of all the atoms in the magnetic moment of the unit cell.

4.4 Single crystal neutron diffraction

The single crystal neutron diffraction experiments were performed to complete the results from powder neutron diffraction and to obtain the magnetic moment at the specific crystallographic sites.

For these experiments, a small cube of approximately 3 x 3 x 3 mm with (100)-type faces was cut from a large single crystal grown from the polycrystalline sample Fe5. The crystal was named as Alloy 3. A detailed description of the growth process will be described in the next chapter. Table 4.5 summarized the composition and transformation and Curie temperatures of the Alloy 3.

Table 4.5: Composition as well as transformation and Curie temperatures determined for Alloy 3

Single crystal	Composition (at. %)	T_M (K)		T_C^A (K)
		T_{af}	T_{ms}	
Alloy 3	$Ni_{45.3}Co_{4.8}Mn_{19.9}Fe_{5.6}Ga_{19}Cu_{5.4}$	373	359	437

The single crystal was first measured in a single variant state of the ferromagnetic marteniste at 300 K at both, D9 and D3 diffractometers, and then heated up to 400 and 540 K for the ferromagnetic and paramagnetic austenite.

Before the measurements, neutron Laue patterns were collected in the Orient express, single crystal Laue diffractometer, at the ILL to verify the single variant state. Figure 4.8 shows the characteristic four fold-symmetry typical for the sample with c long axis along <001> direction. The lack of double or "twin" spots confirms that the crystal is in a mostly single variant state.

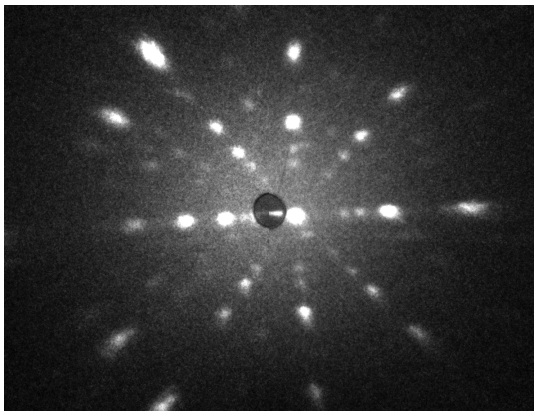

Figure 4.8: Laue diffraction pattern of the single crystal Fe5 oriented along the [001] direction.

4.4.1 Structure analysis and chemical order

The data from D9 were analyzed using the Fullprof suite by the Rietveld refinement method. The structure was refined from the measured integrated intensities, corrected for absorption, including extinction corrections and isotropic temperature factors.

The results for the paramagnetic and ferromagnetic austenite phases are shown in Figure 4.9. Both results show a good agreement between the observed and calculated intensities, with agreement factors of R_{bragg} = 2.88% (540 K) and 4.56% (400 K); and R_F = 4.35% (540 K) and 4.32% (400 K). The slightly larger error obtained for the measurement at 400 K is related to the presence of magnetic contributions which were not considered in the analysis.

The structures obtained have an Fm-3m space group with lattice parameters of 5.8406 Å (540 K) and 5.8036 Å (400 K). Moreover, the atomic distribution was obtained based on the composition measured by EDX. The results are summarized in Table 4.6. As was observed from the powder measurements, the additional elements' distribution follows the same behavior. Fe occupies mainly Ni and Mn sites, Co is located in the Ga positions, and Cu remains at the Mn sites.

In the case of the martensite phase, the results are shown in Figure 4.10. The occupancies are assumed to be the same as in the austenitic phase because of the diffusion-less character of the transformation. The phase was determined as an I4/mmm space symmetry group with lattice parameters of a = b = 3.887 and c = 6.486 Å, in agreement to the powder measurements. The agreement factors are

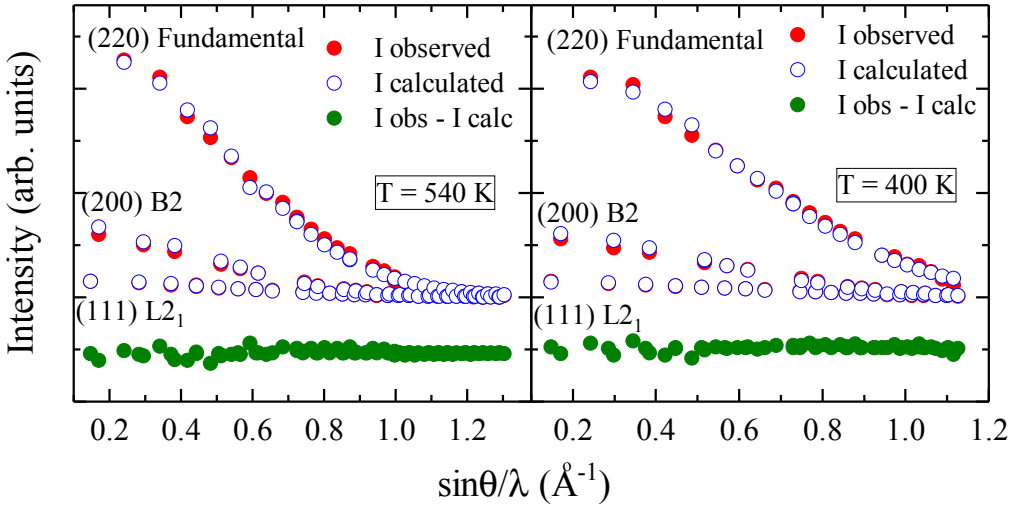

Figure 4.9: Integrated intensity for the calculated and observed reflections and their difference for Fe5 single crystal in the austenite phase at two different temperatures, 540 K (left) and 400 K (right)

Table 4.6: Site occupancies for Alloy 3 with the $L2_1$ structure obtained by Rietveld method. Errors are indicated in brackets.

Alloy	Site (Wyckoff)	Ni	Mn	Ga	Fe	Co	Cu	Total
Alloy 3	Ni (8c)	1.81(2)	0.12(0)	0	0.06(8)	0	0	2
	Mn (4a)	0	0.64(9)	0	0.13(5)	0	0.21(6)	1
	Ga (4b)	0	0.02(7)	0.76(0)	0.02(1)	0.19(2)	0	1

$R_{bragg} = 51.9\%$ and $R_F = 5.53\%$. The substantial increase of the agreement factors is related to the presence of residual variants and the strong magnetic contribution exhibited in this phase, which was not considered in the analysis.

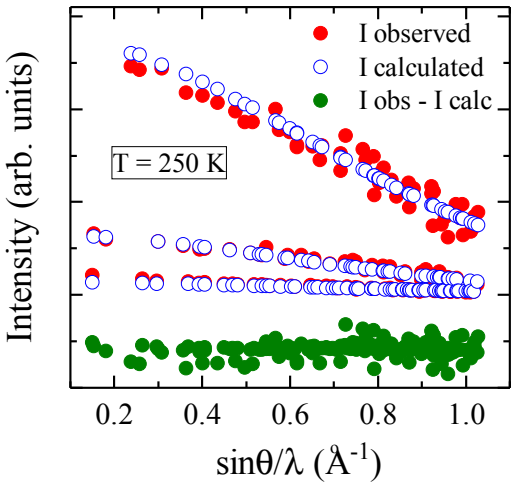

Figure 4.10: Integrated intensity for the calculated and observed reflections and their difference for Fe5 single crystal in the martensite phase (250 K).

4.4.2 Magnetic moment distribution

Polarized neutrons allow for the measuring of magnetic spin density distribution with a high accuracy in comparison with standard neutron diffraction techniques. For a ferromagnetic sample aligned in a field perpendicular to the scattering vector, so that the spin-flip is zero, the cross sections are expressed as:

$$\begin{aligned} I_- = \frac{d\sigma}{d\Omega} = [F_N(Q) - F_M(Q)]^2 \text{ polarized parallel to the field} \\ I_+ = \frac{d\sigma}{d\Omega} = [F_N(Q) + F_M(Q)]^2 \text{ polarized antiparallel to the field} \end{aligned} \tag{4.6}$$

where $F_N(Q)$ is the nuclear structure factor and $F_M(Q)$ is the magnetic structure factor. Using a spin flipper to obtained both cross sections we are able to measure the flipping ratio $R(Q)$ of the different Bragg reflections.

$$R(Q) = \frac{I_+}{I_-} = \frac{[F_N(Q) + F_M(Q)]^2}{[F_N(Q) - F_M(Q)]^2} \tag{4.7}$$

which for a centrosymmetric structure can be simplified to:

$$R(Q) = (\frac{1+\gamma}{1-\gamma})^2 \text{ where } \gamma = \frac{F_M(Q)}{F_N(Q)} \tag{4.8}$$

Thus, by measuring the flipping ratios from the different Bragg reflections to-

gether with an accurate knowledge of the nuclear structure, $F_N(Q)$, determined from unpolarized neutron diffraction, we are able to obtain the F_M(Q). The treatment of the polarized data will be analyzed both, by maximum entropy calculations using Dysnomia[120] (which uses a Limited-memory Broyden–Fletcher–Goldfarb–Shanno (L-BFGS) algorithm[121]) and by the direct fitting of the flipping ratios, performed with the Fullprof suite software.[122]

Direct fitting of the flipping ratios (Fullprof)

The FullProf program calculates the nuclear form factor $F_N(Q)$ from the structural model provided by the user. Afterwards, the scalar magnetic structure factor is calculated as the sum of the contributions of each atom multiplied by the appropriate phase factor. The structural models used were the ones described in the previous section.

The results for the ferromagnetic austenite and martensite phases determined at 400 and 300 K, respectively, are shown in Figure 4.11. The agreement factors associated with the fittings are $R_F = 1.872\%$ $R_{Fw} = 1.714\%$ for the austenite and $R_F = 2.789\%$ $R_{Fw} = 6.417\%$ for the martensite.

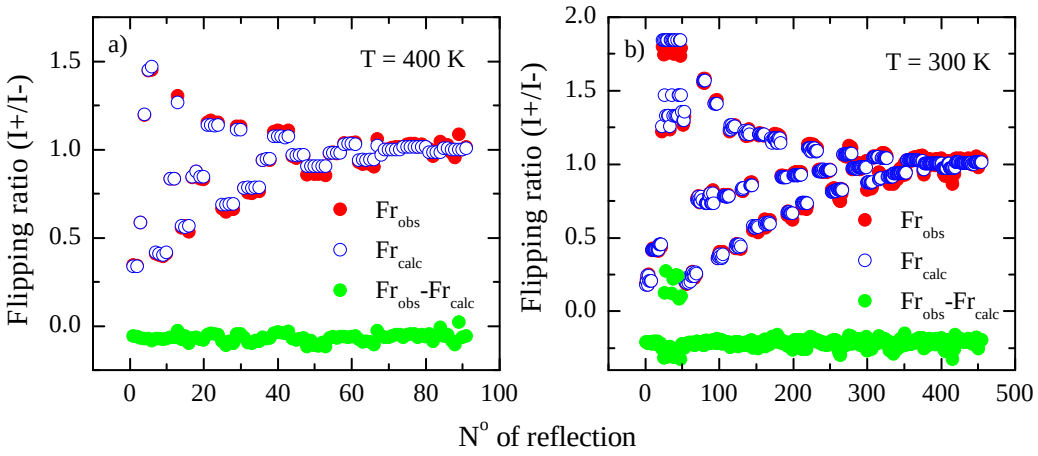

Figure 4.11: Flipping ratios measured at 400 K (a) and 300 K (b) at 7 T compared with the calculated ones together with the difference between them.

The magnetic moments determined are summarized in Table 4.7. The values obtained are an average of the magnetic moments per atom with which the magnetic atoms contribute to each site. The total magnetic moment per formula unit was

calculated using the following equation:

$$\mu_{total} = \mu_{Ni} \cdot n_{mag(Ni)} + \mu_{Mn} \cdot n_{mag(Mn)} + \mu_{Ga} \cdot n_{mag(Ga)} \tag{4.9}$$

where n_{mag} is the magnetic atoms occupation in each site, and μ_x is the weighted average magnetic moment of all magnetic elements occupying the site; for example μ_{Mn} refers to Fe and Mn. This nomenclature will be used throughout the analysis.

The results show that the main contribution to the magnetism is localized at Mn sites. Additional ferromagnetic contributions are also observed in Ni sites and, to a much lesser degree, in the Ga sites. Therefore, the suggested antiferromagnetic Mn_{Mn}-Mn_{Ga} and Mn_{Mn}-Mn_{Ni} interactions must be compensated by the ferromagnetic contribution of the additional magnetic atoms.

Further analysis with techniques such as X-ray magnetic circular dichroism, XMCD, which is element sensitive, will be need to distinguish the contribution between the different elements to the magnetic moment.

Table 4.7: Magnetic moment determined from the direct fitting of the flipping ratios for the different atomic sites at 300 and 400 K and a field of 9 T, and total magnetic moment per formula unit (μ_{total}). The errors are indicated in brackets

Phase	μ (μ_B/magnetic atom)			μ_{Total} (μ_B/FU)
	Ni site	Mn site	Ga site	
400 K	0.188(1)	1.6(3)	0.08(3)	1.6(8)
300 K	0.30(5)	2.5(7)	0.08(7)	2.6(4)

Maximum Entropy Calculations (Dysnomia)

The maximum entropy approach is not affected by any prior assumption of the magnetic density distribution, as it just considers the symmetry group and dimensions of the unit cell and the magnetic structure factors obtained from the measured flipping ratios.[120,123]

For the analysis the unit cell was divided into 233 x 233 x 233 voxels, in the case of the austenite, and 157 x 157 x 257 voxels for the martensite. The Dysnomia software was used to calculate the most probable spin density map. The three-dimensional spin density maps obtained for both phases are shown in Figures 4.13a and 4.13b. As was obtained by the direct analysis of the flipping ratios the main contribution to the

magnetic moment is localized in the Mn sites. No antiferromagnetic contributions are observed.

In order to obtain the total magnetic moment per site, the magnetic moment density obtained from the analysis has to be integrated over a sphere of the appropriate radius. In order to do this, a line profile of the magnetic moment density versus distance was obtained for each unique atomic site in the structure (see figure 4.12(a)). The line along which the plot is drawn is chosen so that the origin of the plot corresponds to the coordinates of the site chosen. The magnetic moment density plot was then fitted to a Gaussian distribution in order to obtain an analytic expression that describes the magnetic moment density around the atomic site. As can be see from the R^2 value in figure 4.12 (a), the magnetic moment distribution can be described very accurately by this type of distribution. The magnetic moment distribution $f(r)$ is integrated over a sphere to obtain the total moment (see equation 4.10).

$$y = \int_0^{2\pi} \int_0^{\pi} \int_0^{R} f(r)\ r^2 sin(\phi)\ dr\ d\phi\ d\theta \tag{4.10}$$

$$f(r) = \frac{A}{w\sqrt{\frac{\pi}{2}}} e^{-2(\frac{x}{w})^2}$$

where $f(r)$ is the gaussian function.

As can be seen in figure 4.12(b), where the integral is plotted vs. radius, as the radius increases the moment contained by that sphere increases at first but then reaches a saturation value. This saturation value is the total moment of the site. In order to obtain the radius of the sphere that contains the total moment for the site the first derivative of the plot is taken, the radius is the one where the derivative becomes zero. The site magnetic moments calculated with these radii are shown in Table 4.8.

As mentioned before, the spin density maps show the most probably spin density distribution which is an average of all the possible existing unit cells. If we consider that the different sites are not fully occupied by magnetic atoms, not all the possible cells will exhibit the same magnetic moment. Considering for example the Mn site, it could be occupied by Mn, Fe, or Cu; in the case of a cell with Cu atoms, the magnetic moment will be less than a cell fully occupied by magnetic atoms. Thus, to estimate the contribution of the magnetic atoms and compare it with the results of the direct

analysis of the flipping ratio, the site magnetic moments must be divided by the magnetic atoms' occupation in each site. The magnetic moments per atom obtained for the three sites are also shown in Table 4.8. Qualitatively comparable results were obtained for both measurements with flipping ratio analysis and maximum entropy method.

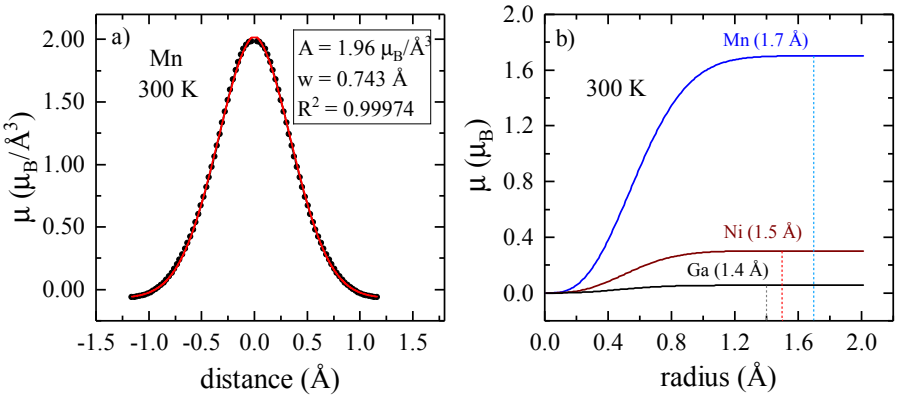

Figure 4.12: (a) Gaussian fitting of the spin density profile at a Mn site. (b) Integrated magnetic moment as a function of the radius for the three different sites.

Table 4.8: Magnetic moment per site and magnetic moment per magnetic atom calculated from the maximum entropy analysis for the two different temperatures at a field of 9 T. The errors are indicated in brackets

Phase	Magnetic moment (μ_B/site)			Magnetic moment (μ_B/atom)		
	μ_{Ni}	μ_{Mn}	μ_{Ga}	μ_{Ni}	μ_{Mn}	μ_{Ga}
400 K	0.2(4)	1.3(3)	0.0(4)	0.2(4)	1.7(0)	0.1(8)
300 K	0.3(0)	1.7(0)	0.0(2)	0.3(0)	2.1(7)	0.0(9)

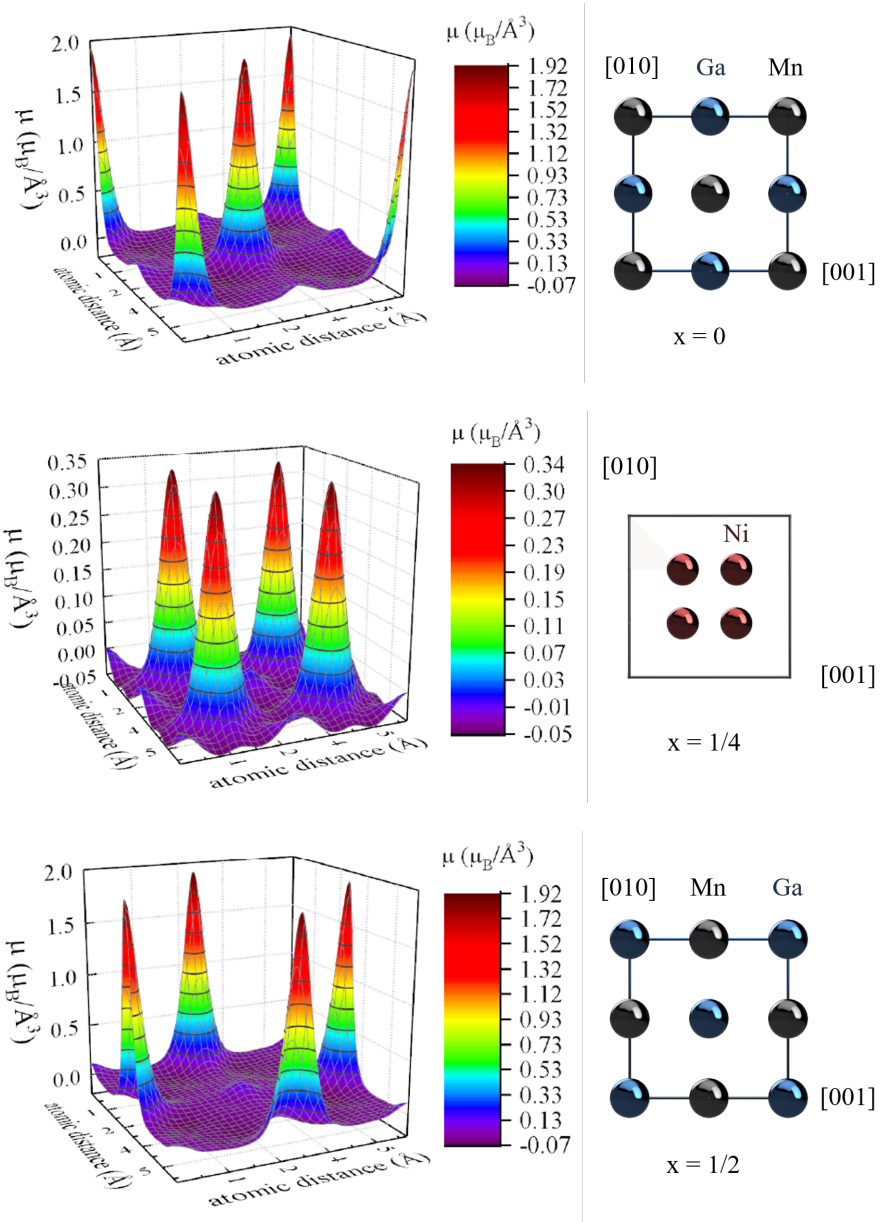

Figure 4.13: Spin density map in the (100) plane at x = 0, 1/2 and 1/4 of the $L2_1$ structure measured in the ferromagnetic austenite phase at 400 K under 7 T, together with the atomic distribution in these planes. The maps were obtained by Maximum Entropy method using Dysnomia software[120] and plotting with VESTA software.[124]

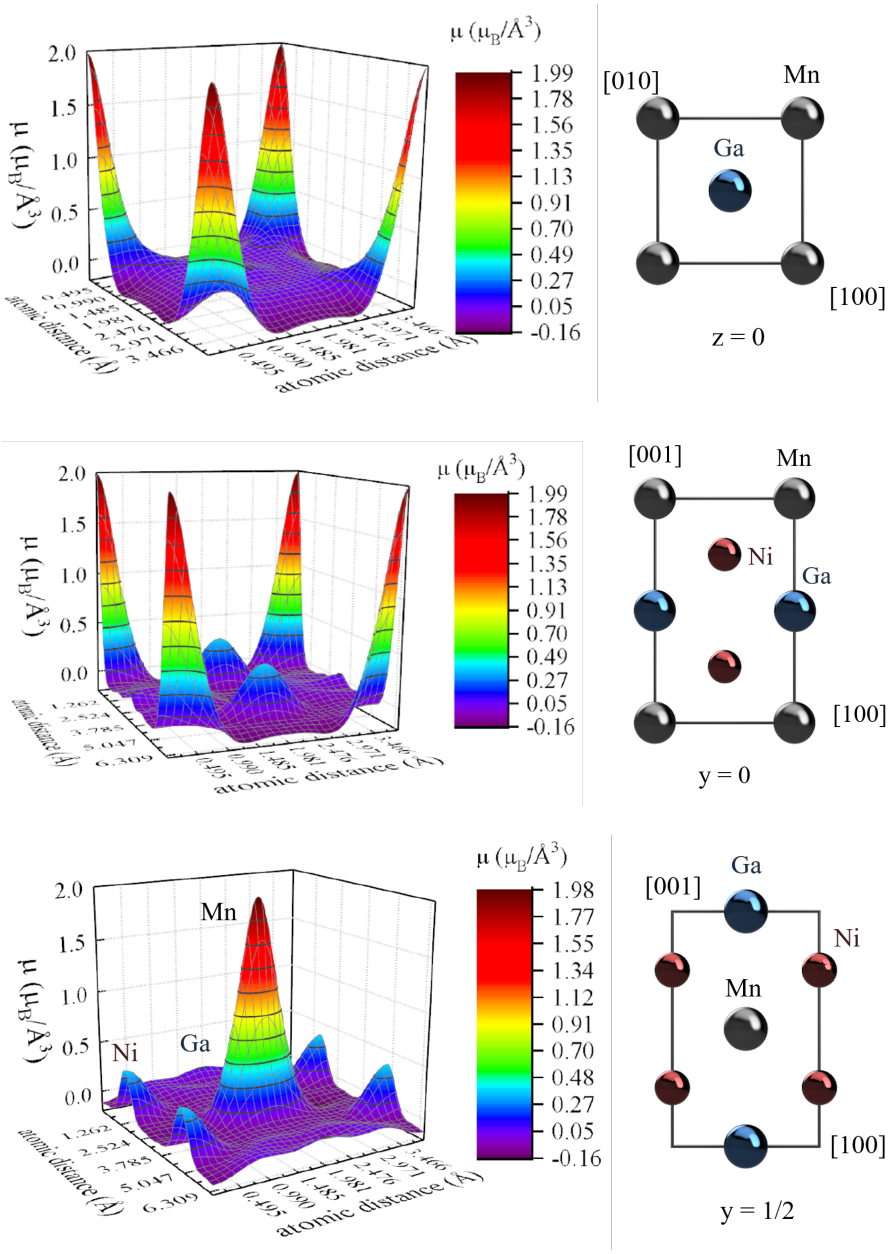

Figure 4.14: Spin density map in the (100) plane at x = 0, 1/2 and 1/4 of the martensite structure measured in the ferromagnetic austenite phase at 400 K under 7 T, together with the atomic distribution in these planes. The maps were obtained by Maximum Entropy method using Dysnomia software[120] and plotting with VESTA software.[124]

Experimental determination of the saturation magnetization

To determine the saturation magnetization and compare it with the ones obtained by polarized neutrons, hysteresis loops up to 2 T were measured at the same temperatures (300, 400 and 540 K). Figure 4.15 shows the typical ferromagnetic behaviour for the measurements at 300 and 400 K and the paramagnetic one for the high temperature measurement at 540 K.

The values of saturation magnetization were determined for the ferromagnetic austenite and martensite phases by the Arrott plot method,[86] as shown in the inset to Figure 4.15.

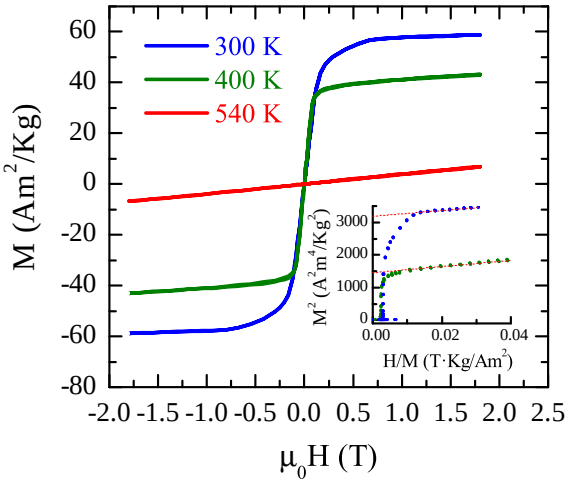

Figure 4.15: Hysteresis loops measured at 300, 400 and 540 K.

A comparation between the magnetic moment per formula unit obtained by the three methods is shown in Table 4.9.

Table 4.9: Total magnetic moments per formula unit determined from the different methods for ferromagnetic austenitic and martensitic phases.

Phase	μ_{total} (μ_B/FU)		
	μ_{fit}	μ_{dys}	μ_{exp}
400 K	1.6(8)	1.8(5)	1.6(4)
300 K	2.6(4)	2.3(2)	2.4(3)

Some variations obtained between the two methods based on neutron results

could be related to inaccuracies in the a priori assumptions, that is, in the structural model introduced for the flipping ratio analysis, or in the simplification to a spherical symmetry in the case of the maximum entropy. In fact, the values obtained are in the range of the experimental ones, being the flipping ratio method the best one for the austenite phase and the maximum entropy for the martensite one.

These results can serve as a fairly good approximation, however, further studies must be performed to determine the magnetic distribution in this complex system and distinguish the magnetic contribution between the different atoms.

4.5 Summary and conclusions

We have solved the structure, chemical order and magnetic moment distribution of a multicomponent series of $Ni_{45}Mn_{25-x}Ga_{20}Co_5Cu_5Fe_x$ in powder and single crystal form by performing neutron diffraction and analyzing the results by different methods.

Two different structures were identified, an I4/mmm tetragonal structure for the martensite phase and a Fm-3m cubic structure for the austenite one. The addition of Fe resulted on a variation of the lattice parameters: In the case of the martensite, a decrease of the c_{Mart} and an increase of the a_{Mart}, and consequently, a reduction of c/a, was obtained. The c/a reduction was also observed as a function of temperature, due to the convergence of the tetragonal structure to the cubic one. For the austenite phase the a_{Aus} parameter decreases as a function of Fe addition.

In this chapter we have also disclosed the atomic site occupation of the alloys with an Fe content from 0 to 5%. The results show a clear tendency for Cu to occupy Mn sites, while the preference of Co and Fe varies with the concentration of Fe. With a low Fe content, Co is distributed among Ni and Ga sites; however, as Fe content increases, Co is further displaced to the Ga sites and Fe tends to occupy Ni and Mn sites. Mn atoms are distributed among the three different unique sites.

This atomic distribution has a huge influence on the magnetic properties due to the different Mn–Mn interatomic distances that this system exhibits. The Mn_{Mn}-Mn_{Ni} and Mn_{Mn}-Mn_{Ga} distances in the austenite phase suggest antiferromagnetic contributions, while in the martensite just the Mn_{Mn}-Mn_{Ni} and half of the Mn_{Mn}-Mn_{Ga} ones may correspond to antiferromagnetics couplings.

The preference of Co for Ni and Ga sites together with the amount of Fe in Ni sites leads to a reduction of the number of Mn atoms out of their proper sites, and

consequently reduces the amount of antiferromagnetic contributions. This effect, together with the addition of ferromagnetic atoms such as Co and Fe, leads to an increase of the saturation magnetization.

Unpolarized and polarized neutron diffraction techniques were used to determine the chemical order and site-specific magnetic moment distribution in a single crystal grown from Fe5. The results obtained for the chemical order are consistent with the ones of the polycrystalline series. The site-specific magnetic moment distribution, was analyzed by two different methods: a direct fitting of the flipping ratio, which uses a defined structural model obtained from unpolarized neutrons; and the maximum entropy analysis, which does not consider any a priori assumption and only takes into acount the symmetry and lattice parameters. The magnetic moments obtained are an average of the contribution of all the magnetic atoms located at each site.

The results for both methods show that the main contribution to the magnetic moment is associated to the Mn sites. Additional ferromagnetic contributions are also obtained for the Ni sites and to a much lesser degree for the Ga sites. The total magnetic moment per formula unit, determined from the two methods, agreed with the experimental value.

Some differences observed between the two methods could be related to the simplified a priori assumptions. Nevertheless, these results can be used as a fairly good approximation to the magnetic moment distribution of a complex six-component Ni–Mn–Ga–Fe–Co–Cu system.

Further investigations will be performed to distinguish the specific magnetic contribution of each magnetic atom and improve the models used in this chapter.

Chapter 5

High Temperature Ferromagnetic Shape Memory Ni–Mn–Ga (Co, Cu, Fe) alloys: Functional properties

5.1 Introduction

Interest in Ni–Mn–Ga alloys comes from the giant magnetic field-induced strain (MFIS) they exhibit (up to 12%, for non-modulated martensite[30]). MFIS originates from the field-induced rearrangement of twin variants in the martensitic state[20] and occurs only in the ferromagnetic martensite. The maximum deformation achievable is related to the spontaneous tetragonal distortion of the martensite $\epsilon = 1\text{-}\frac{a}{c}$. Therefore, in order to get large MFIS, large value of c/a is desirable. However, large c/a values are associated with large twinning stresses (σ_{tw}), as discussed in previous chapters. To exhibit giant MFIS, the twinning stress must be smaller than the stress produced by the magnetic field, i.e., magnetostress, σ_{mag}, and therefore, a compromise between σ_{tw} and σ_{mag} must be found. Several studies have been focused on lowering σ_{tw} by doping,[30,65] mechanical treatments[125] or by modifying the microstructure.[126] On the other hand, the value of magnetostress, reached in the magnetically saturated state, is also related to the tetragonality ratio, c/a[1,25,127] and the uniaxial magnetic anisotropy constant, K_u,[26–28,128] of the martensite as $\sigma_{mag} = (1\text{-}\frac{a}{c})^{-1}K_u$. Therefore, the crystal structure of the martensite affects both the twinning and the magnetic

stresses, and determines the maximum strain attainable.[113,125] Tailoring the aforementioned parameters to satisfy MFIS existence condition plays the key role in the development of high temperature MSM alloys (HTMSMAs).

In Chapter 3, the simultaneous alloying of Ni-Mn-Ga alloys with Co, Fe, and Cu allowed to select[96] three compositions:

- (S0) $Ni_{43}Co_7Mn_{20}Fe_2Ga_{21}Cu_7$ named Alloy 1
- (Fe4) $Ni_{45}Co_5Mn_{21}Fe_4Ga_{20}Cu_5$ named Alloy 2
- (Fe5) $Ni_{45}Co_5Mn_{20}Fe_4Ga_{20}Cu_5$ named Alloy 3

with high T_M, T_C and low c/a as feasible candidates for high temperature MSM actuators. Single crystals of such compositions are studied now to obtain the relevant parameters for MFIS, such as twinning stress, magnetic anisotropy, and magnetostress.

5.2 Experimental section

The single crystals studied in this chapter were grown at the Lappenranta University of Technology (LUT) in Finland. The master alloys used for the growth (6 mm in diameter) were produced by induction furnace as decribed in previous chapters. The masters were hand-milled for the single crystal growth. The growth method was a modified Bridgman-Stockbarger. The equipment utilized is an in-house made furnace located at the Lappenranta University of Technology (LUT). During the growth, the crystal was subjected to a 0.2 bar pressure of 99.98 % Ar. Each single crystal is grown from an oriented seed at a speed of 0.5 mm/min. The vertical temperature gradient was calculated to be 50 K/mm near the solidification interface. The obtained single crystals were heat-treated under argon at 1223 K for 24 hours followed by cooling during 1 hour to 723 K and holding for 4 hours to promote a $L2_1$-type atomic order. Rectangular specimens (≈11 x 4 x 4 mm^3) were cut by a high precision wire saw (Princeton Scientific Corp., WS-22) from the rods. Specimens' surfaces were mechanically and electrochemically polished.

The nominal compositions were confirmed with an accuracy of 0.5 at.% by energy dispersive X-ray spectrometry (EDX) performed by Bruker Quantax 70 detector in

a Hitachi TM3000 Scanning Electron Microscope. Low-field susceptibility measurements under a magnetic field of 0.01 T were performed to obtain the transformation (T_{af}, T_{as}, T_{mf} and T_{ms}) and Curie temperatures.

The characterization of the single crystals presented in this chapter was performed at the Lappenranta University of Technology during several research stays.

Crystal structure and temperature dependences of lattice parameters were determined by XRD using PANalytical Empyrean diffractometer with CoK_{α} radiation. The measurements were performed in collaboration with Dennys Musiienko.

Mechanical tests were performed by a MTS Criterion C43.104 mechanical testing machine. A climatic chamber was developed to study the stress-strain behavior of MSM single crystals at different temperatures. Special care was undertaken to thermally isolate the machine's mechanical and electrical components from the chamber. The sample was placed between two polished brass plates, one on the top and the other one on the bottom. The maximum stress applied was fixed up to 20 MPa. The temperature chamber with the sample inside was filled with water to provide more uniform temperature distribution.

The magnetization measurements at different temperatures were performed by Andrey Saren at the Lappenranta University of Technology (LUT) in Finland. For magnetization measurements, the sample was placed between the poles of an electromagnet (LakeShore EM4-HVA). The magnetic field was swept in the range of $\pm$ 1000 kA/m at a frequency of 1 Hz. The external field was measured using standard search probe coil located close to the sample's surface. The sample's internal field was measured with a coil wound around the central part of the sample. Both coil voltages were integrated using a flux meter (M-Pulse, M-Flux 3000), to obtain the flux values, that were recorded with a data acquisition board (NI USB-6361) and recalculated to the correspondent field values. A special holder made from a high thermal conductivity material, encasing the sample, was used to exclude temperature gradient along the sample, and thin thermal insulators were used to isolate the sample from the magnet poles. A thermocouple was placed inside the sample holder, touching the sample. The temperature variation was realized using an air-heating device.

5.3 Structural and functional properties of the single crystals

Single crystal rods with a size of 6 mm in diameter and 30 mm in length were grown for each of the mentioned alloys. After the heat treatment, the crystals were cut into three pieces, each one of ≈ 10 mm, and named as up, middle and bottom part (close to the seed).

Prior to any measurement a slice of the bottom part of the crystals was cut for metallographical observation by optical microscopy to reveal the possible presence of multiple crystals. Figure 5.1 shows two optical micrographies at different magnifications for the Alloy 3. Figure 5.1 clearly shows a multi-variant state on the polished surface of the single crystal. Except of a small residual grain observed in the right micrograph, the sample is a single crystal. The results for Alloy 1 and 2 are similar to the ones obtained for Alloy 3.

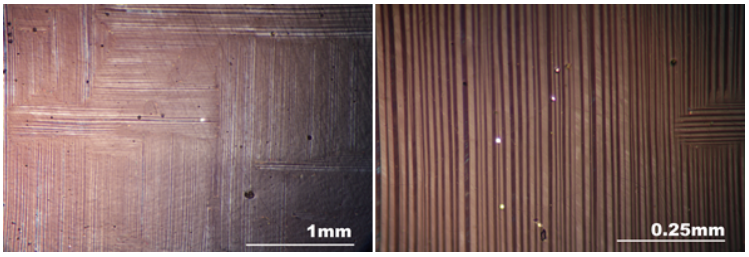

Figure 5.1: Optical micrographs of Alloy 3 at two different magnifications.

5.3.1 Transformation behavior

Low-field magnetic susceptibility measurements as a function of temperature were performed to determine the transformation and Curie temperatures for each piece of the three crystals after heat treatment. Figure 5.2 shows an example of the magnetization curves of the up (black), middle (blue) and bottom (red) part of the Alloy 2. As it can be seen, there is an increase of the transformation temperatures from the bottom to the upper part of the crystal. A slight decrease on the Curie temperature is also obtained, however the effect is considerably smaller. T_{af}, T_{as}, T_{mf}, T_{ms}, and ${T_C}^A$ values are summarized in Table 5.1.

An increase of T_M of ≈ 15 - 40 K from the bottom to the top part of the crystals is obtained for the three samples. However, ${T_C}^A$ values are not essentially modified.

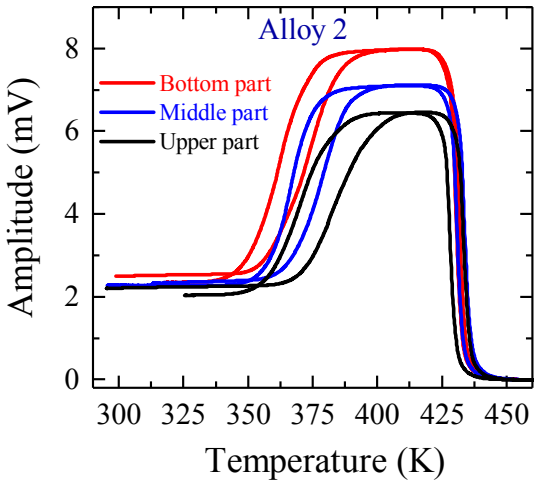

Figure 5.2: Low-field magnetic susceptibility measurements as a function of temperature for the bottom (red), middle (blue), and upper (black) part of the Alloy 2 ingot. A magnetic field of 0.01T was applied.

Table 5.1: Alloy notation and transformation temperatures determined from susceptibility measurements by tangent method.

Alloy	Crystal part	Temperatures (K)				
		T_{af}	T_{as}	T_{ms}	T_{mf}	T_C^A
Alloy 1	Upper	390	377	374	367	423
	Middle	379	369	363	355	423
	Bottom	376	365	362	347	424
Alloy 2	Upper	399	372	383	358	428
	Middle	389	368	375	357	430
	Bottom	387	357	374	347	431
Alloy 3	Upper	405	365	395	365	433
	Middle	373	359	359	357	437
	Bottom	350	335	343	341	435

All the parts of the crystals grown exhibited $T_M > 373$ K and $T_C > 423$ K as defined for high temperature applications.

The variation of the transformation temperatures observed is related to a composition gradient produced during growth. As discussed in Chapter 2, the higher solubility of Mn in the liquid than in the solid, results in an enrichment of the crystal with Mn as the growth progresses.

In contrast to the floating zone method described in Chapter 2, the modified Bridgman-Stockbarger does not allow good convection in the liquid and the temperature gradient of the melted zone is larger. Thus, there is a larger composition gradient and, therefore, the variation of the properties from one end to the other of the crystal.

The main advantage of the modified Bridgman-Stockbarger method is the better control of the orientation and the larger size of the crystals obtained. In this case, to have a preferential orientation is a critical task, as all the properties to be determined in the current study are strongly dependent on it.

For further characterization experiments, the middle part of the crystals was selected as the one with the composition closest to the nominal one. Composition of the selected parts are indicated in Table 5.2.

Table 5.2: Nominal and measured compositons of the Alloys 1, 2 and 3.

Alloy	Nominal Composition (at. %)	Measured composition (at. %)
Alloy 1	$Ni_{43}Co_7Mn_{20}Fe_2Ga_{21}Cu_7$	$Ni_{43.1}Co_{6.7}Mn_{19.5}Fe_{2.2}Ga_{20.8}Cu_{7.7}$
Alloy 2	$Ni_{45}Co_5Mn_{21}Fe_4Ga_{20}Cu_5$	$Ni_{45.1}Co_{4.9}Mn_{21.1}Fe_{4.5}Ga_{19.1}Cu_{5.3}$
Alloy 3	$Ni_{45}Co_5Mn_{20}Fe_4Ga_{20}Cu_5$	$Ni_{45.3}Co_{4.8}Mn_{19.9}Fe_{5.6}Ga_{19}Cu_{5.4}$

5.3.2 Structural analysis

The single crystal rods were oriented in the martensite phase. Rectangular prisms of 4 x 4 x 10 mm^3 were cut by abrasive wire saw with the face normals corresponding to the [001]– and [100]– directions. After cutting the surfaces were mechanically and electrochemically polished.

A heating stage is used in the diffractometer, which allows the determination of the cell parameters as a function of the temperature. The temperature scan was performed using the (400)M and (004)M reflections, according to the cubic cordinates, in the martensite phase, and the (004)A in the austenite one. The cell parameters were determined based on these reflections.

The results show that all the crystals studied exhibited a non-modulated (NM) tetragonal martensite with c/a $>$ 1. The dependencies of the lattice parameters, c_{NM} and a_{NM}, as well as c/a ratio, are plotted in Figure 5.3 as a function of the relative temperature (T-T_{as}) for ease of comparison.

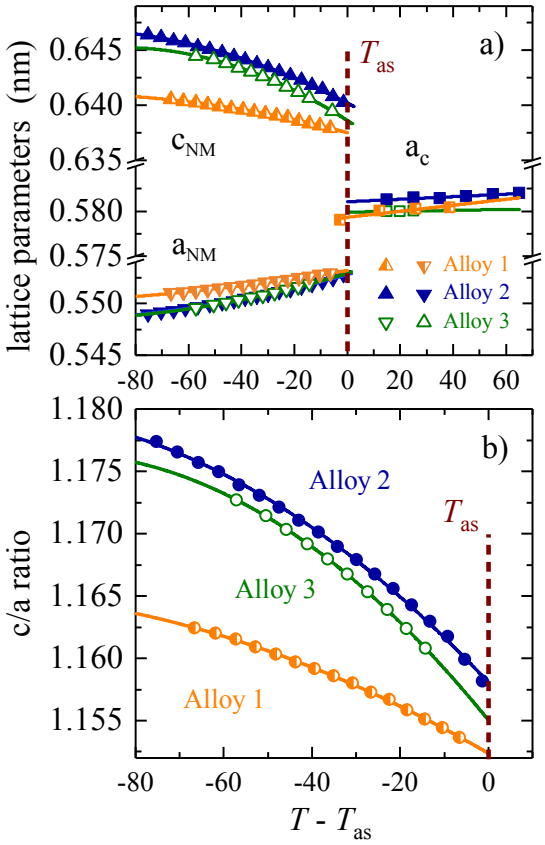

Figure 5.3: Temperature dependences of the lattice parameters of tetragonal non-modulated martensite, a_{NM} and c_{NM}, and cubic austenite, a_c (a); as well as tetragonality ratio, c/a (b) for the three single crystals. The solid lines are guides for the eye. The dashed line marks the austenitic start temperature, T_{as}.

The curves in Figure 5.3 show that near the transformation temperature the lattice parameters of the martensite have a nonlinear temperature dependence, while the lattice parameter of the cubic austenite, a_c, exhibits a conventional linear thermal expansion. As expected, a reduction of the c/a ratio with T_M is observed.[129] This reduction is much less pronounced for Alloy 1, evidencing a significant composition dependence of the unit cell parameters and their temperature evolution.

As observed in the previous stuidy from Lanska et al.,[1] Ni-Mn-Ga NM martensites exhibit an increasing c/a with the increase of T_M. According to that study, it could be expected that an alloy with T_M around 370 K should present a c/a $\approx$ 1.20 at room temperature, T_R. However, the addition of Cu, Co, and Fe resulted in a decrease of c/a at T_R down to 1.163, 1.177, 1.173 for Alloys 1, 2 and 3 respectively. Evidence

of the influence of additional elements on the structure were already demonstrated and discussed in Chapter 3. As there is an experimental relation between c/a and σ_{tw}, the reduced c/a values obtained for these alloys suggest that their twinning stress, σ_{tw}, should be smaller than that for NM Ni-Mn-Ga alloys with similar T_M temperatures.[30,72] Additionally, the low c/a values obtained near T_{as}, of 1.153, 1.158, 1.155 for the Alloys 1, 2 and 3 respectively, are close to the ones reported by Sozinov et al.[30] for a NiMnGaCoCu single crystal exhibiting MFIS at room temperature.

5.3.3 Mechanical Properties

To determine the values of σ_{tw}, single variant samples were prepared. As a first step, the samples were cooled down from austenite under compression to induce the nucleation of preferential variants with the [001] axis in the direction of stress. The second step consists on a training procedure under successive compressions along [001] and [100]/[010] directions, which is called detwinning process.

Figure 5.4 shows a schematic representation of a compression along the [001] direction, indicated by a red arrow, and the variants reorientation process occurred in Alloy 3. The optical images correspond to two different faces of the rectangular prism taken before (a), in the middle (b) and at the end (c) of the compression test. The orientation of each face is indicated in the images and the scheme.

A rotation of the c axis (001) from one to the other side face of the prism is observed. The longest side of the prism, which corresponds to a short a/b axis (100)/(010), remains unchanged during the process.

It is worth noting that the training procedure is decisive to minimize σ_{tw} and obtain the MFIS effect (see, e.g., Refs.[130,131]). The use of compression as a training procedure has been commonly used for modulated tetragonal and orthorhombic martensites, with one short axis.[132] In those cases, the compression induces the formation of the variants with short axis close to last compression axis.

In the case of NM martensites with c/a $>$ 1, the compression method is not well suited as it favours the formation of two variants with equivalent short axes (a = b).[131] However, the training procedure was selected due to the experimental limitations of the mechanical test machine.

In order to corroborate the single variant state after the trainning procedure, polarized light images were taken. The results for the Alloys 2 (a) and 3 (b) are

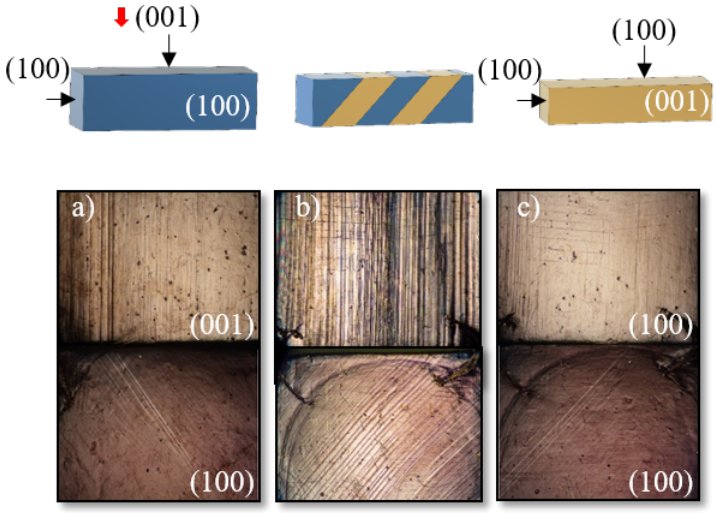

Figure 5.4: (Top) Schematic representation of variant reorientation during a compression along the <001>. The blue and yellow colors correspond to two different twin variants. (Bottom) Optical micrographs during a compression test for Alloy 3, at different stages of the process: (a) Before compression, (b) in an intermediate state and (c) fully reoriented

shown in Figure 5.5 as an example. In the Figure 5.5 (a) a nearly single variant state, with a small volume fraction of other twin variants, which appear as dark lines, is presented. In the case of Alloy 2 (b) the volume fraction of the residual variants is larger than for Alloy 3. Alloy 1 is very similar to Alloy 2. Therefore, a single variant of Alloy 3 is the best quality one.

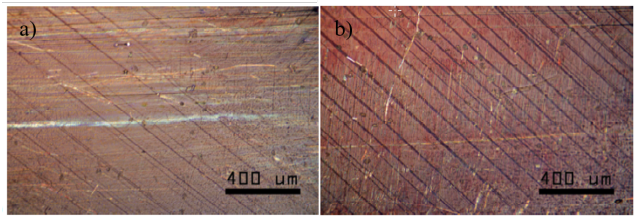

Figure 5.5: Optical images of the Alloys 2 (b) and 3 (a) samples taken with polarized light contrast, revealing presence of the residual variants.

Stress-strain measurements under compression were performed at different temperatures for the three alloys. These measurements allow to determine the σ_{tw} and the maximum achievable strain in the full temperature range of actuation.

Representative curves at different temperatures obtained for Alloy 3 are shown in

Figure 5.6. The curves can be divided into three different regions: Two elastic parts and a pseudoplastic plateau. The initial linear increase of the curve is related to the elastic deformation of the single variant martensitic structure. At a certain stress, the variant reorientation occurs, reaching the pseudoplastic plateau and at the end of the plateau, the elastic part of the reoriented single variant state is reached. When the stress is released, the elastic strain is recovered but the maximum deformation obtained due to variant reorientation is retained. The σ_{tw} value was determined from the stress-strain curves at different temperatures, as the stress in the middle part of the pseudoplastic plateau, as seen in Figure 5.6.

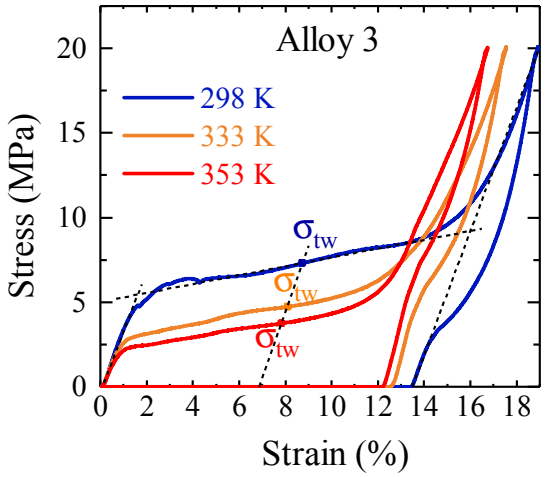

Figure 5.6: Representative stress-strain curves under compression at different temperatures for Alloy 3

The relative temperature dependencies of σ_{tw} for all the alloys are plotted in Figure 5.7, alongside data for a NM Ni-Mn-Ga martensite with similar T_{as}, taken from Ref.[133] for comparison.

The temperature evolution of σ_{tw} shows a rapid and linear decrease in all cases, with a slope between -0.04 and -0.05 MPa/K. This agrees with the previous results for both NM[133] and 10M modulated Ni-Mn-Ga alloys with type I twin boundaries.[24,134]

The experimental value of ϵ_{max}, determined at room temperature from the stress-strain curves, is equal to 13.0, 14.0 and 13.5% for Alloy 1, 2 and 3, respectively. These values are close to the theoretical ones, determined from $\epsilon = (1 - a/c)$, which means that single variant specimens were almost fully reoriented by compression. The decrease of ϵ_{max} with the temperature is related to the reduction of c/a on

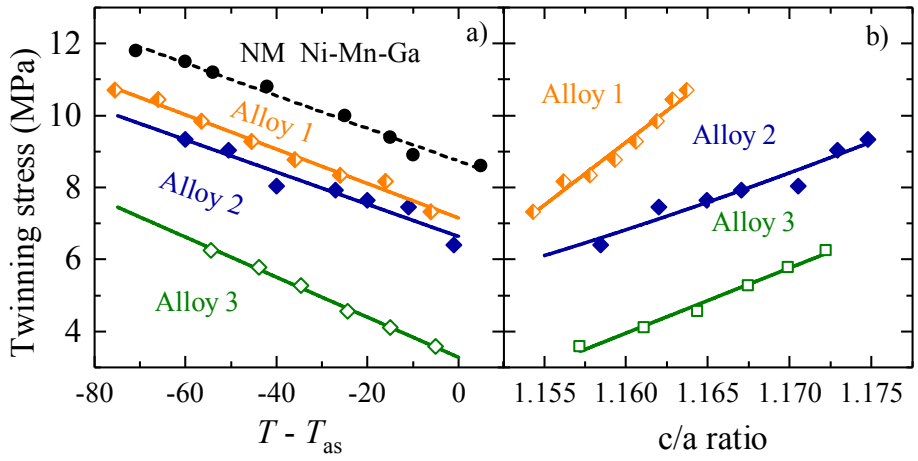

Figure 5.7: (a) Relative temperature dependences of the twinning stress for the three studied alloys and for a Ni-Mn-Ga NM sample from Ref.[133] The solid lines are linear fits. (b) Twinning stress as a function of the c/a ratio. The solid lines are guides for the eye.

approaching T_M.

The dependencies of the twinning stresses on the c/a ratio are plotted in Figure 5.7(b). These results confirm a correlation between both two parameters. The different dependencies observed in Figure 5.7(b) reflect a significant composition dependence. The effect of additional elements in the alloy is also evidenced by comparing the measured values of σ_{tw} with the ones observed for conventional NM Ni-Mn-Ga alloys from Ref.[133] (See Figure 5.7). The reduced σ_{tw} values obtained for the studied alloys can be understood as a result of the c/a reduction. However, they are still high comparing with the average values reported in the literature for NM Ni–Mn–Ga (6-18 MPa).[135]

The differently oriented residual variants observed by optical microscopy is one of the possible reasons of the elevated σ_{tw} obtained. By improving the training procedure and reducing the influence of additional factors, such as impurities, composition inhomogeneities or surface roughness[125,136–138] the σ_{tw} could be further reduced.

Recently, Soroka et al.[72] suggested that σ_{tw} is proportional, with some universal proportionality constant, to c/a, when both parameters are measured just below T_{as}. According to this prediction, Alloys 1, 2, and 3 should show $\sigma_{tw} \approx 0.8$ MPa, which is much lower than shown in Figure 5.7. Therefore, further efforts to improve the quality of the crystals and the training procedure are needed to minimize σ_{tw} and

confirm the viability of these alloys as HTMSMAs. Considering $\sigma_{tw} \approx 0.8$ MPa as the lowest attainable value for these alloys, the condition for MFIS would be $\sigma_{mag} > 0.8$ MPa at T_{as}. It is worth remembering that the maximum achievable σ_{mag} value is limited by K_u. Therefore, in the present work, the critical magnetic parameters, such as K_u and σ_{mag}, were examined by the magnetic measurements.

5.3.4 Magnetic Properties

Large magnetic anisotropy, K_u, is a precondition for this kind of materials to exhibit MFIS. K_u represents the maximum energy density which can be supplied to the material by an external magnetic field.[139] It is known that the non modulated Ni-Mn-Ga martensites with c/a > 1 exhibit a uniaxial anisotropy with easy plane and hard magnetization direction along the long crystallographic axis.[1,126,133,134,140,141]

The magnetocrystalline anisotropy energy $E_{anisotropy}$ of a tetragonal crystal can be written as:[26,142]

$$E_{anisotropy} = K_1 sin^2\theta + K_2 sin^4\theta + K_3 sin^4\theta cos4\phi \tag{5.1}$$

where K_1, K_2, and K_3 are anisotropy constants, θ is an angle between magnetization and the crystal hard axis (c-axis) and ϕ is a polar angle in the plane perpendicular to the c-axis. In the case of a single axis of magnetization $K_2 \ll K_1$ and this expression can be simplified as:

$$E_{anisotropy} = K_1 sin^2\theta \tag{5.2}$$

which allows to determine the uniaxial magnetic anisotropy constant $K_1 = K_u$ directly from the magnetization curves by the equation 3.1.

To properly determine the magnetic anisotropy the samples must be in a single variant state. First of all the samples were oriented with the longest and magnetically hard c-axis along the samples' length, by means of a mechanical stress. In order to measure the easy axis the samples were again mechanically compressed to orient the c-axis perpendicular to the longest direction.

During the mechanical testing, Alloy 1 was cracked and the sample was reduced and polished up to a final size of 1.33(a) x 1.37(a) x 4.35(c) mm^3. The sample sizes of Alloy 2 and 3 were 3.6 x 3.46 x 11.7 mm^3 and 3.53 x 3.73 x 12.43 mm^3 respectively. Magnetization measurements for Alloys 2 and 3 were performed from room temperature up to T_{as}. Due to size restrictions the measurements for Alloy 1

were performed only at room temperature.

Room temperature magnetization curves for Alloy 2 measured along the <100> (red) with a-axis oriented along the field and <001> (blue) directions with c-axis aligned along the field are plotted in Figure 5.8(a). As seen in the Figure the magnetization in <100> plane saturates instantly, while in the case of the <001> direction the saturation occurs at higher fields.

The initial different slopes in the hard magnetization curve indicate the presence of some residual variants in which the easy magnetization direction is oriented along the applied field. This fact is in agreement with the optical image in Figure 5.1.

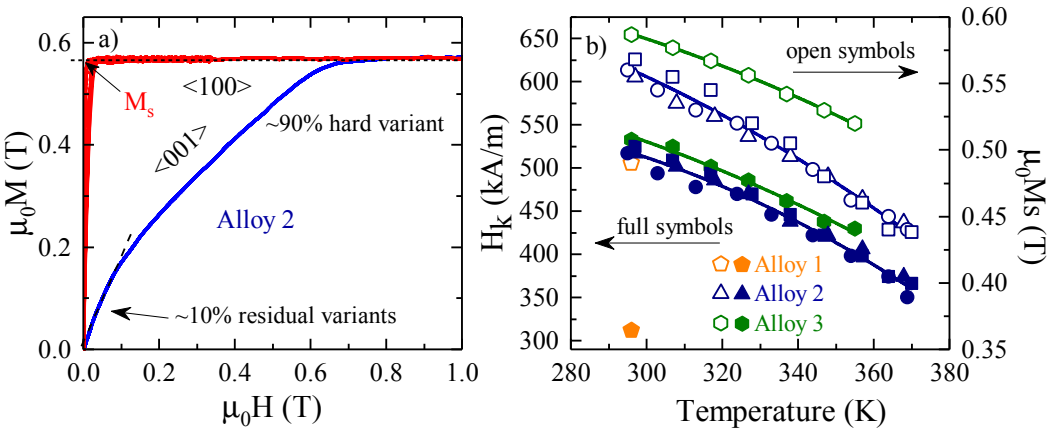

Figure 5.8: (a) Magnetization curves for easy (red) and hard magnetization (blue) directions measured for Alloy 2 at room temperature. (b) Saturation magnetization (open symbols) and anisotropy field (full symbols) values as a function of temperature determined from the magnetization curves.

From the magnetization curves, it is possible to obtain the saturation magnetization, M_s, and anisotropy field, H_k, values. M_s values were obtained from M(H) curves by a linear extrapolation of high field values to μ_0H=0. The H_k is obtained by the extrapolation of the linear part of M(H) curve along the hard axis to the saturation magnetization, M_s. The temperature dependencies of the parameters M_s and H_k are presented in Figure 5.8(b).

A decrease of M_s and H_k with the temperature is observed for Alloys 2 and 3. Similar trends are obtained for the H_k, however, the decrease of M_s is faster for Alloy 2. This fact is related to the lower T_C exhibited by Alloy 2 in comparison with Alloy 3.

The room temperature values obtained are, $\mu_0 M_s = 0.49$ T and $\mu_0 H_k = 0.39$ T

for Alloy 1, $\mu_0 M_s$ = 0.56 T and $\mu_0 H_k$ = 0.65 T for Alloy 2, and $\mu_0 M_s$ = 0.59 T and $\mu_0 H_k$ = 0.67 T for Alloy 3. The highest M_s observed for Alloy 3 is related to the effect of Fe addition, which promotes ferromagnetic exchange, as discussed in Chapter 3. The substantially reduced values of H_k and M_s for Alloy 1 are due to the increased content of Co and Cu (Table 5.2). Thus, the simultaneous addition of Co and Cu produces a weakening of the magnetic properties, as was also observed, e.g., by Rame et al.[26]

The magnetic anisotropy constant, described by equation 3.1,[142] was calculated from the numerical data at T_R. The values obtained were -76 kJ/m^3, -146 kJ/m^3, and -157 kJ/m^3 for Alloys 1, 2, and 3, respectively. The negative sign indicates that in these alloys the tetragonal axis is a hard axis of magnetization.

Figure 5.9(a) shows the (T-T_{as}) dependence of K_u for Alloys 2 and 3. Similarly to the behavior of σ_{tw}, the trend of K_u with temperature is a linear decrease, with slopes of -0.8 and -0.9 kJ·m^{-3}/K, for Alloys 2 and 3, respectively.

Differences in anisotropy are produced by both the composition[26,143] and the tetragonal distortion,[144] since they affect the spin-orbit coupling and magnetoelastic properties.[47,113,145,146]

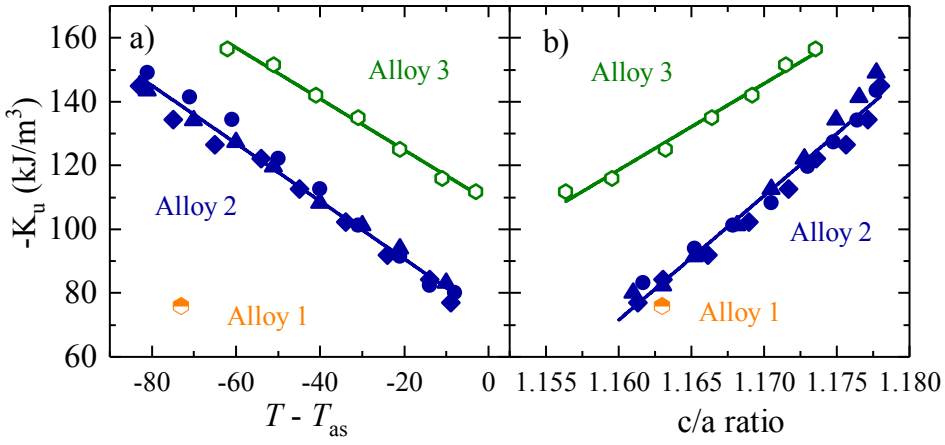

Figure 5.9: Magnetic anisotropy constant as a function of the relative temperature (a) and the c/a (b) for the alloys studied.

To assume that K_u depends on a single parameter in these complex systems is a very rough simplification. Even if there is a dependence of the K_u with the c/a, as seen in Figure 5.9(b), the values obtained for different alloys with the same c/a can show the same relative change with composition as is observed for alloys in the same

series with c/a. This is a clear indication that the enhancement of K_u is primarily affected by composition changes. In fact, both the K_u and c/a and their correlation are affected by the alloy compositions.

5.3.5 Magneto-mechanical Properties

Magnetostress can be determined in two different ways:

(i) By direct measurement of the stress-strain curves' shift produced by magnetic field.[24]

(ii) By the following relation $\sigma_{mag} = (1\text{-}\frac{a}{c})^{-1}K_u$ using the measured magnetic and structural data..

The direct measurement of σ_{mag} at T_R was done by stress-strain curves recorded during continuous mechanical uniaxial compression and orthogonal saturating magnetic field of 1.5 T being switched on and off during short parts of the deformation cycle. The jump of stress value in stress-strain curve resulting from switching on the magnetic field provides the direct value of the magnetostress. For this study, the single crystal sizes were reduced to approximately 4 x 4 x 3 mm^3.

Figure 5.10(a) shows a schematic representation of the method used together with the experimental curve obtained for Alloy 3. The values obtained at T_R by the two methods are summarized in Table 5.3. As can be seen from this table both methods show a good agreement, being the experimental values slightly lower than the calculated ones.

Table 5.3: Calculated and experimentally measured values of σ_{mag} (MPa) at room temperature for the three single crystals

Alloy	σ_{mag}^{exp} at T_R (MPa)	σ_{mag}^{calc} at T_R (MPa)
Alloy 1	0.44	0.54
Alloy 2	0.89	0.95
Alloy 3	1.03	1.07

The σ_{mag} obtained from Figure 5.10(a) and the calculated ones were plotted as a function of the relative temperature in Figure 5.10(b). Measured σ_{mag} values are indicated by solid symbols and calculated ones by open symbols.

A linear decrease of σ_{mag}(T) is observed for Alloys 2 and 3, with slopes about ten times smaller than those of σ_{tw} versus (T-T_{as}) (see Figure 5.7). A $\sigma_{mag} > 0.8$

MPa just below T_{as} is only observed for Alloy 3. The higher σ_{mag} obtained for Alloy 3 is related to the addition of Fe, that resulted in a large increase of K_u. Alloy 1, in turn, shows the lowest magnetic properties due to the low Fe content and the highest addition of Co and Cu. The latter one, as seen in Chapter 4, displace the Mn out of its proper position leading to an increase of antiferromagnetic contributions.

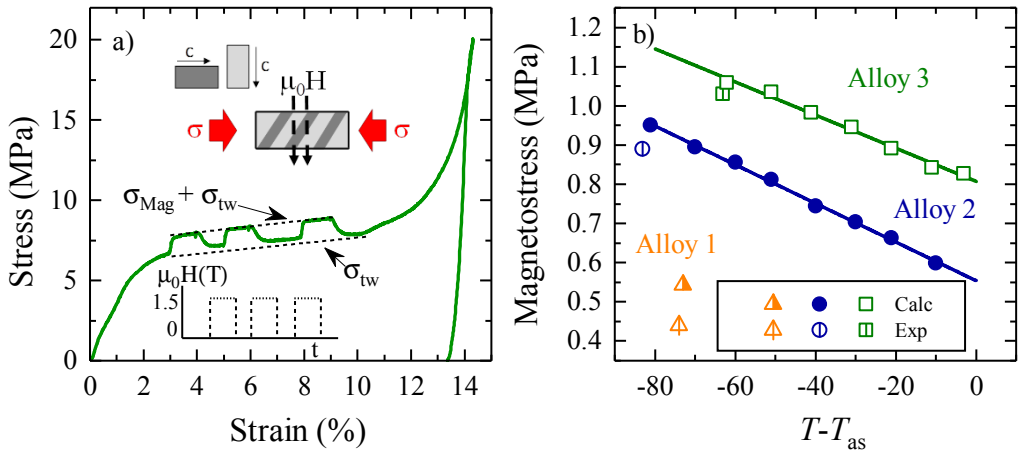

Figure 5.10: (a) Representative parts of stress-strain curves measured at room temperature under a periodical application of saturating magnetic field. The humps in the plateau-like region, corresponding to the twin-rearrangement, are produced by switching-on and switching-off the magnetic field. The height of the humps directly provides the value of magnetostress, σ_{mag}. The top inset describes the orientation of the long c axis towards the directions of applied stress σ and magnetic field μ_0H during the experiment. The bottom inset shows schematically the periodic application of the magnetic field. (b) Calculated and measured magnetostress dependencies as function of the relative temperature.

5.4 Summary and Conclusions

In summary, three single crystals from a novel six-components Ni(Co)–Mn(Fe)–Ga(Cu) alloy system were grown to explore the possibility of magnetic actuation in non-modulated tetragonal FSMAs at high temperatures. A systematic study of the temperature and composition dependencies of the key parameters responsible for magnetic field induced twin boundary motion, such as magnetocrystalline anisotropy (K_u), twinning stress (σ_{tw}), magnetostress (σ_{mag}) and tetragonality ratio (c/a), was performed.

It was found that the values of σ_{tw}, K_u, and σ_{mag} decrease almost linearly when approaching T_M, showing similar slopes for the different alloys. Such a behavior is indicative of their universal character. The values and evolution of these parameters with the tetragonality ratio are highly dependent on composition, reflecting its influence on the elastic and magnetoelastic constants. Fe plays an important role reinforcing ferromagnetism and leading to a considerable increase of K_u and the corresponding σ_{mag}. Further analysis should be performed to disclose the individual effect of Co and Cu addition in the weakening of the ferromagnetic properties of martensite phase.

Reduction of σ_{tw} is necessary to achieve the condition $\sigma_{mag} > \sigma_{tw}$ at high temperatures. To further reduce σ_{tw}, the use of the ultra-pure base elements for the master alloys fabrications and the elaboration of more efficient magneto-mechanical training protocols are needed. Numerical parameters for Alloy 3 at about 370 K are very close to fulfilling the conditions for large magnetostrains in non-modulated martensite. A fine tailoring of σ_{mag} and σ_{tw} by the aforementioned procedures is a realistic path to obtaining magnetically activated HTFSMAs for novel applications.

Chapter 6

Conclusions and Future work

6.1 Conclusions

The main purpose of this work was to design and study of new conventional and ferromagnetic shape memory alloys with high temperature actuation ranges with the ultimate goal to be used as high temperature sensors and actuators in a near future. A deep study of the influence of the composition on the structural and magnetic properties in SMAs together with the evaluation of the critical parameters to obtain the magnetic field induced effect comprise an essential task for the real implementation of these materials. The general conclusions of the work are summarized as follows.

Different compositions of Ni–Mn–Ga exhibiting the conventional shape memory effect for high temperature applications and their thermal and thermomechanical stability are studied. The analysis of the results enabled the following deductions:

- The transformation behavior of Ni–Mn–Ga SMAs obtained from the β and $\beta + \gamma$ regions show two very distinct behaviors: (i) The simple thermal cycling induces the degradation of the material's properties in the two phase region, due to the precipitation of a second phase, while, for the single phase region the material remains stable. (ii) On the other hand, the combination of temperature and stress during the thermo-mechanical cycling induces the precipitation of a second phase in both regions.
- The heat treatments have a considerable influence on the thermo-mechanical behaviour of the alloys by acting as a pre-nucleation of the second phase and

giving rise to different stabilization dynamics; as well as leading to different precipitation processes due to stress release.

- The thermo-mechanical cycling elaborated is a adequate training procedure leading to a stable actuation at high temperatures. With this training we have achieved for the heat-treated sample SC3 a T_{af} of 673 K with a stable recovery strain of 3%.

The study of the composition effect on the transformation, structural and magnetic properties of three Ni–Mn–Ga–(Co, Cu, Fe) polycrystalline FSMA series results in the following conclusions:

- The increase of Fe content resulted in an increase of T_C and a decrease of T_M. The increase of the saturation magnetization can be related to the ferromagnetic contribution of Fe atoms that increase the exchange interactions.

- The substitution of Ga by Cu led to an increase of T_M and c/a ratio, and a decrease of ${T_C}^M$, while the substitution of Mn by Cu resulted in a minimum in the T_M and c/a at 7.5 at.% Cu.

- A universal relation between the crystal structure and the transformation temperatures was found. However, the composition also plays an important role in the reduction of the c/a for the multicomponent series if compared to Ni–Mn–Ga compositions exhibiting similar T_M.

- Among the compositions studied, three alloys, $Ni_{43}Co_7Mn_{20}Fe_2Ga_{21}Cu_7$ (S0), $Ni_{45}Co_5Mn_{21}Fe_4Ga_{20}Cu_5$ (Fe4) and $Ni_{45}Co_5Mn_{20}Fe_5Ga_{20}Cu_5$ (Fe5), exhibit simultaneously high values of T_M and T_C over 373 K and 423 K respectively.

From the structural, atomic order and magnetic neutron studies carried out on the Fe serie, the following results have been obtained:

- All the samples studied exhibit I4/mmm martensite and Fm-3m austenite structures.

- A reduction of the c/a is obtained as a function of the increasing temperature and the Fe addition.

- The atomic site occupancy of the multicomponent Ni–Mn–Ga–Fe–Co–Cu alloys with an Fe content from 0 to 5% was determined for the first time. A clear tendency for Cu to occupy Mn sites is seen, while the Co and Fe preference varies with the concentration of Fe. For low Fe content, Co is distributed among Ni and Ga sites; however, as Fe content increases, Co is displaced to the Ga sites and Fe tends to occupy Ni and Mn sites. Mn atoms are distributed among the three different unique sites.

- The magnetic properties strongly depend on the atomic order, due to the different Mn–Mn interatomic distances presented in the alloy system. The addition of Co and Fe reduces the amount of Mn out of its proper site and consequently reduces the antiferromagnetic contributions.

- The spin density maps and the magnetic moments obtained indicate that the main magnetic contribution is located at Mn sites. Additional ferromagnetic contributions are also obtained for the Ni sites and to a much lesser degree for the Ga sites.

Finally, the critical parameters for obtaining MFIS were analyzed for the selected compositions S0, Fe4 and Fe5 in a single crystal form, named Alloys 1, 2 and 3. In this case, the following conclusions are made:

- A linear temperature dependence of the σ_{tw}, K_u, and σ_{mag} was obtained for all the three alloys. The structural dependence (c/a) of these parameters is more complex, being highly dependent on composition.

- The addition of Fe resulted in a considerable increase of K_u and the corresponding σ_{mag}, and in a reduction of the c/a, leading to promising high temperature FSMAs.

- Further reduction of σ_{tw} is necessary to achieve the condition $\sigma_{mag} > \sigma_{tw}$ at high temperatures for a real implementation of these alloys.

6.2 Future work

During the progress of the thesis some works have been already started and can be of interest in furthering the research done so far.

On the one hand, it is worth exploring the addition of other elements such as Ag and Zn, and analyzing their influence on the material's properties. Until now, we have observed that the solubility of Ag on this system is very low, being even less than 1%, which hinders its use as dopant. In the case of Zn, successful results have been obtained with additions up to 1.5%, which lead to a drastic increase of T_M. However, its high reactivity during the induction melting, limited us to use brass instead of pure Zn, and consequently, introduced a considerable amount of impurities, which would have strong influence on the single crystal properties. An optimization of the melting process for pure Zn is under development.

The single crystal growth method has to be optimized in order to improve the quality of the crystals and reduce the σ_{tw} values in the Alloy 3. This work is going to demonstrate magnetic field induced strain at high temperatures, which is a crucial task to achieve a real implementation.

Finally, to complete the results obtained by polarized neutrons, it will be very useful to perform X-ray magnetic circular dichroism (XMCD) measurements. These measurements will provide the average magnetic moment contribution for each type of atom. The combination of this technique and the results from polarized neutrons presented in this thesis will give us the precise contribution of each atom at each specific site for the first time in such a complex system.

Appendix A

Preparation Techniques

A.1 Induction Furnace

An induction furnace was used for the preparation of the master alloys during the thesis. The equipment used was a commercial induction furnace model Induret Compact made by REITEL Feinwerktechnik GmbH (Bad Essen, Germany), identical units were available, at the University of Basque Country (UPV/EHU) and at the Lappeenranta University of Technology (LUT) in Finland.

An induction heater consists of a coil, and an electronic oscillator that passes a high-frequency alternating current (AC) through the coil. The rapidly alternating magnetic field penetrates the object, generating electric currents inside the conductor called eddy currents. The eddy currents flowing through the resistance of the material heat it by the Joule effect.[147] This fenomenon was firstly discovered by Michael Faraday in 1831. The special feature of the induction heating is that the heat is generated inside the material by the currents flowing in it. Thus, melting occurs very rapidly. Additionally, the use of a high-frequency magnetic field serves as stirring, allowing an homogenization of the melt during the process.

The furnace utilized (See Figure A.1) consists of a thick helicoidal coil, which is refrigerated by water and surrounds a ceramic crucible. The ceramic crucible has an opening below, which will keep closed with a stopper during the melting process. A thermocouple is introduced into the stopper to control the temperature. The vacuum in this particular furnace is generated using a Venturi pump limiting the vacuum achievable to the single mbar range in absolute pressure. Because of the relatively low vacuum pressure, several purges with gas mixture, consisting in Ar

with 5% by volume H, had to be done to improve the quality of the atmosphere and ensure that a reducing atmosphere would be present during casting. The melt is then cast into a copper or steel mold of the final desired shape by pressurizing the crucible with the Ar/H gas and lifting the stopper at the bottom of the crucible.

Figure A.1: (Left) Reitel Induret Compact induction furnace used for master alloys production (Right) Crucible and copper mold are utilized for melting and casting.

A.2 Optical floating zone single crystal growth method

The float Zone (FZ) method is based on the zone-melting principle and was invented by Theuerer in 1962. The growth takes place under vacuum or in an inert gaseous atmosphere. The process starts with a high-purity polycrystalline rod placed vertically in the growth chamber and a single crystal seed with known orientation held face to face in a vertical position and rotated.

The optical furnace utilized was a FZ-T-P1200-H-I-S from Crystal Systems Inc., Japan, located at the Basque Center of Materials, Applications and Nanostructures. In this furnace the heat is produced by four ellipsoidal mirrors focusing the light from halogen lamps onto a vertically held feed rod. The use of light heating makes the technique suitable for both conducting and non-conducting materials.[148,149] Due to the heat, a molten zone is formed and held between the seed and feed rods by its own surface tension. When the molten zone is stable, the lamps are swept at a constant rate along the sample to melt the polycrystal seed at the top and re-solidifying as a single crystal at the bottom of the melt bone. The growth rate was set to 10 mm/h and the power supply was kept during the growth at $\approx$ 40-50% of the maximum one.

A controlled heating ramp was fixed to avoid instabilities in the molten zone. The upper and lower parts can rotate in opposing directions with speeds between 5-100 rpm. The stability of the molten zone can be monitored by visualizing the growth through a CCD camera. An Ar + H(5%) flow was supplied keeping a maximum pressure of 0.35 bar inside the chamber.

Figure A.2 shows an image of the growth chamber and the four ellipsoidal lamps. The quartz tube isolates the growth process from the rest of the chamber. On the right side, a molten zone formed between the feed rod and the seed is observed.

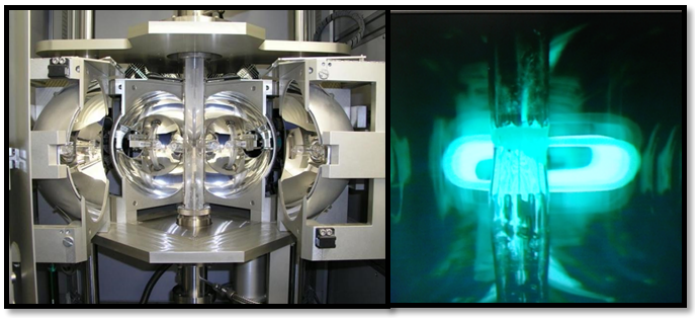

Figure A.2: (Left) Single crystal growth chamber surronded by the four ellipsoidal halogen lamps. (Right) In situ visualization of the molten zone during the growth by the CCD camera.

A.3 Modified Bridgman-Stockbarger single crystal growth method

The modified Bridgman-Stockbarger method consists on the crystallization of the melt starting from a half-way molten oriented single crystal seed. The crystallization is produced by displacing the heater along the porous alumina crucible containing the sample.

The furnace used was designed and in-house built at the Lappeenranta University of Technology by Prof. Kari Ullakko's group. Figure A.3 shows an schematic representation of the furnace used. The master material (powder or bulk) is introduced in the porous alumina crucible placed in a vertical position. The oriented seed is located in the bottom part of the alumina crucible, which ensures a contact angle of 45° between the seed and the master.

A pre-melting of the master is done by moving down the furnace down to a

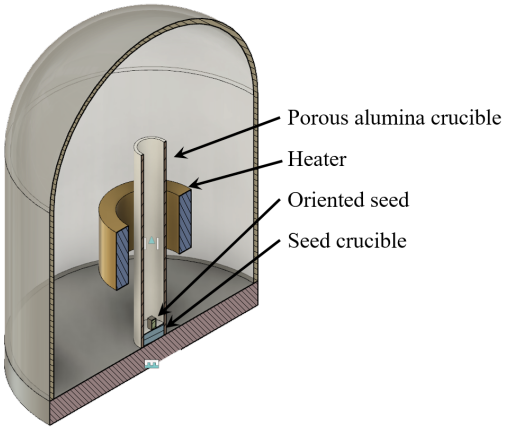

Figure A.3: Schematic representation of the single crystal growth furnace used for the Bridgman-Stockbarger method.

specific distance in which half of the seed is melted. The furnace moved at 1.5 mm/min speed. From this point the furnace is moved up again at a constant speed of 0.5 mm/min allowing the crystal growth. Two thermocouples are used to allow a better control over the temperature gradient at the melt/crystal interface. The first thermocouple is located near the bottom part of the seed and the second one inside the furnace. Vertical temperature gradient reaches 50 K/mm around the hot zone.

A.4 Development of a Heat Treatment Furnace

In this work, the heat treatment of the samples, either in bulk or powder form, constitutes an important step of the sample preparation. The composition change or the oxidation of the samples when treating at high temperatures are the main issues to deal with.

In order to facilitate a proper high temperature treatment of Ni-Mn-Ga based alloys a high temperature heat treatment furnace has been designed and built in collaboration with Iraultza Unzueta at the UPV/EHU.

A.4.1 Furnace Requirements

A heat treatment furnace must consist of: An annealing chamber, a furnace, a cooling system, gas incorporation system and vacuum pumps.

As the annealing chamber, a Khantal tube APM^{TM} has been acquired from

Sandvic, Hallstahammar, Sweden. This material was selected as it exhibits good thermal stability up to 1520 K, which is above the temperature range needed for our materials.

The tube was placed inside a comercial furnace. The coupling of the Khantal APM^{TM} tube to the rest of the system was done by welding to a DN40 CF flange. The other side of the tube was sealed using a piece of the same Khantal APM^{TM} alloy. The DN40 CF flange was connected to a DN25 ISO-K reducer using a cooper gasket. This system ensures a coupling with leak rates $< 10^{-9}$ mbar l/s. On the other hand, the connections between the tube and the remaining part of the setup (pumping, pressure read-out and gas incorporation system) have been done by conventional KF flanges and viton O-rings.

A refrigeration systems consisting of a cooper tube wound around the outside of the Khantal tube was made (see Figure A.4). The copper tube was connected to a water flow system to ensure constant cooling. Additionally, in order to minimize the heat transfer due to the radiation, a removable reflective disc of stainless steel was fabricated and introduced into the annealing chamber.

Finally, the furnace was connected to a nEXT Edwards Turbo Pumping Station with both rotary and turbo pumps. In order to avoid Mn losses and oxidation, a reductive atmosphere of Ar + H(5%) is introduced in the chamber before the treatments. To control the pressure inside the chamber before and after gas introduction, a Digital Thermovac TM101 DN16 KF pressure reader from Leybold was used. The detected pressure range goes from 10^3 down to 10^{-4} mbar. Figure A.4 shows an overview of the full setup (FUPOG[1]).

[1] Feuchtwanger-Unzueta-Pérez-Orue-García Furnace.

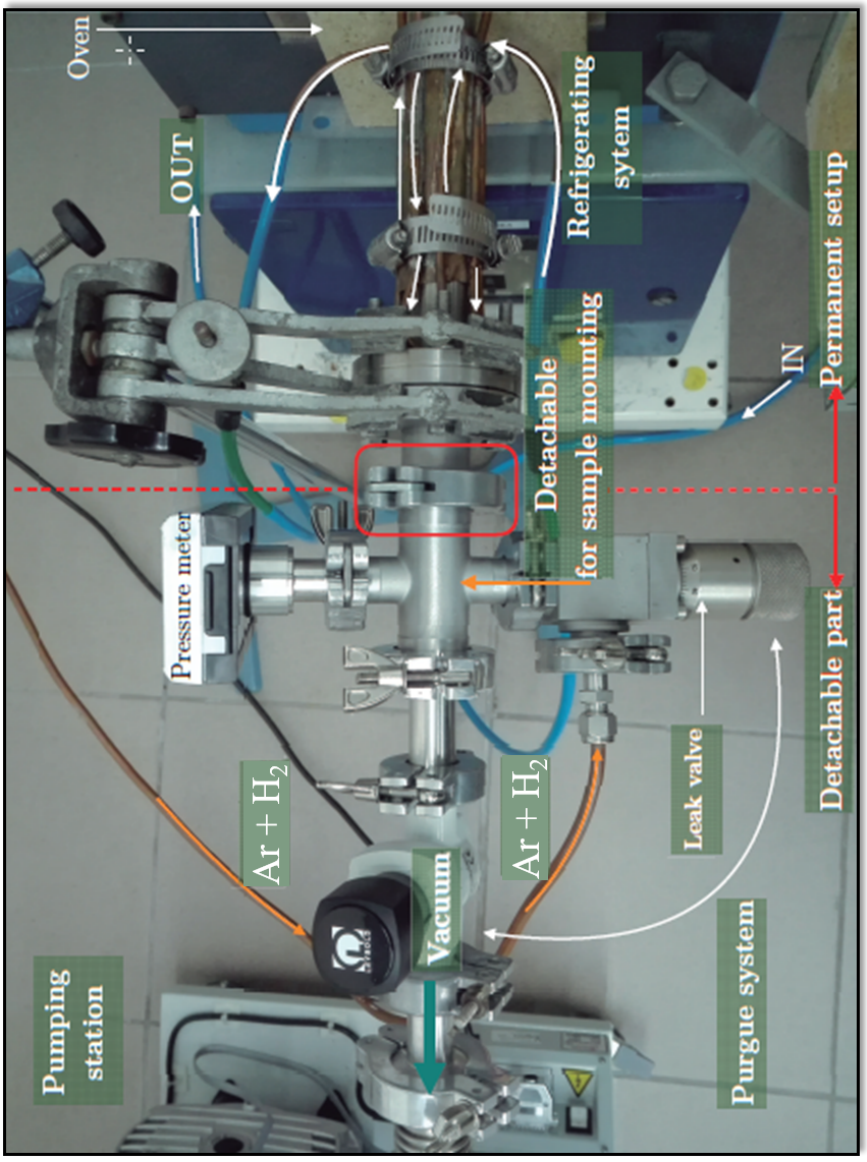

Figure A.4: Picture and schematic view of the furnace.

Appendix B

Characterization Techniques

B.1 Structural characterization

B.1.1 X-Ray and Neutron Diffraction Techniques

X-ray and Neutron Diffraction are very common techniques widely used to characterize the structure of a material. Both techniques are based on the diffraction phenomena produced when a X-ray or neutron beam is scattered by a material.[150,151]

The diffraction phenomenon can be described in a first approximation by Bragg's law:

$$n\lambda = 2dsin\theta \tag{B.1}$$

where d is the distance between the crystallographic planes, n is the interference order (an integer number), λ is the incident X-ray or neutron beam wavelength and θ is the angle between the incidental beam and the scattering planes.

However, in order to understand the differences between neutron and X-ray scattering, as they define the advantages of each technique in specific cases, the problem must be considered as the exact interaction between a wave and a series of periodically spaced point scatteres. What the wave sees as the scatterer is different depending on whether X-rays or neutrons are used, x-rays interact with the electron cloud of the atoms, while neutrons interact with the nuclei and the magnetic moment.

In the case of X-rays, it is well known from Compton and Allison[152] that the

amplitud scattered by an electron, E, at a distance r is:

$$E = \frac{e^2}{mc^2}\frac{1}{r}sin\chi \tag{B.2}$$

where e, m are the charge and the mass of the electron, c is the velocity of the light and χ is the angle between the direction of scattering and the direction of the electric field vibration in the incident radiation. If we consider a single atom with multiple electrons, the scattering amplitude will be proportional to the atomic number, Z. Therefore, the structure of materials with atoms of similar Z may be difficult to evaluate by X-rays. Another fact of X-rays is that as the dimensions of the electronic cloud are comparable with the X-rays wavelenght the amplitude falls of rapidly with the increase of the Bragg angle θ. The falling rate depends on $(\sin\theta)/\lambda$ and is described by the form factor of each atom, f_x, (See Figure B.2). In consequence, the X-ray pattern of crystalline materials, when of high symmetry, will provide very few peaks concentrated at low angles.

In the case of neutrons the interaction mainly occurs with the nucleus and not with the electron, except for magnetic materials. In contrast to the rapid increase of the X-ray scattering amplitude with Z, the neutrons scattering factors, b, are independent on Z and shows no variation with the angle θ. The dependence of b with Z is quite random specially for transition materials, as seen in Figure B.1, and allows to distinguish for scatters with similar Z.

As the nucleus sizes are small in comparison with the wavelength, the 'form factor', also known as scattering lenght, b, for neutrons is a constant (See Figure B.2).

As mentioned before, magnetic atoms comprise an exception on neutron scattering, as in this case, there is an additional interaction between the neutron magnetic moment and the magnetic moment of the atom. This interaction occurs between unpaired electrons of the atoms, given raise to magnetic moment, and the spins of the neutrons, which have a spin quantum number = $\frac{1}{2}$ and a magnetic moment μ = -1.913μ_N , where μ_N is the nuclear magneton constant, μ_N = 5.0507·10^{-27} J/T. Due to the electronic nature of the magnetic interaction, the scattering magnetic amplitude is defined by a magnetic form factor, f_{mag}, similar to the one of X-rays. As in the magnetic neutron scattering just the electrons at the outer shells interact, the f_{mag} falls of more rapidly with θ than the one for X-ray scattering, f_x (See Figure B.2).

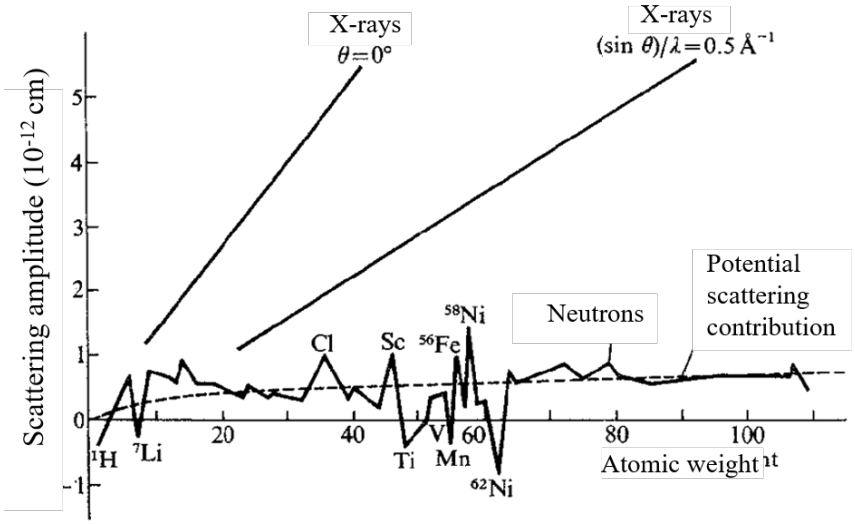

Figure B.1: Variation of the scattering amplitude of atoms for neutrons as a function of their atomic weight. This figure has been taken from Ref.[150]

Figure B.2 shows a simple sketch with the comparison of the variation of f_x, b and f_{mag}. As a result of this, neutron diffraction is the only diffraction method used to reveal the magnetic structure and can provide high contrast in compounds with atoms of similar Z.[153]

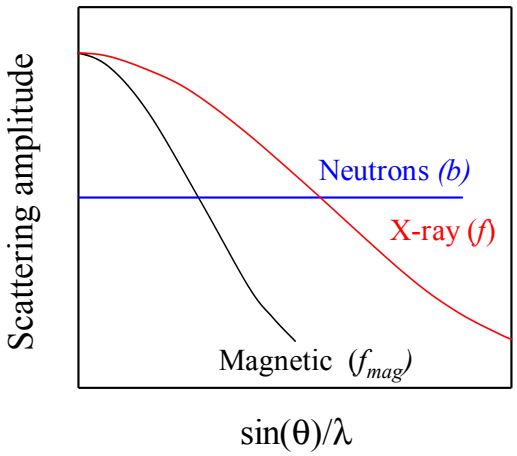

Figure B.2: Schematic representation of the X-ray, neutron and magnetic scattering form factors

The analysis of the neutron or X-ray patterns was carried out with the refinement

techniques proposed by H. M. Rietveld, developed in the FullProf Suite.[112,154] Two different analyses were performed: Pattern Matching and Rietveld method.

The pattern matching analysis does not require any structural information except an aproximate value of the lattice parameters. With this option, it is possible to remove any contribution of the motif to the structure providing a much simpler data treatment and spreading considerably out the application field of the powder pattern.

In the case of a Rietveld analysis, this method allows the refinement of crystallographic and/or magnetic structures by a fit of the complete profile of the experimental powder or single crystal diffractograms (either X-ray or neutrons) to a theoretical profile by using a least squares approach.

Experimental devices

X-ray Diffractometers :
The X-ray diffraction measurements were performed on two diffractometers: A Philips X'Pert Pro diffractometer (UPV/EHU) with Cu-K_α radiation and a theta-theta geometry; and a PANalytical Empyrean Diffractometer (LUT) with a Co radiation and Bragg–Brentano optics and focusing geometry.

D1B High Intensity Two-axis Powder Diffractometer (ILL) :
D1B is a two-axis spectrometer dedicated to powder diffraction experiments requesting a high neutron flux. At small angles where magnetic peaks are expected, a high spatial resolution can be achieved. The intrument has a transmission (Debye-Scherrer) geometry.

Seven pyrolytic graphite monochromator crystals focusing onto the sample position provide a flux of $7.9 \cdot 10^{6}$ n·cm^{-2} s^{-1}. D1B is equipped with 3He/CF4 position sensitive detector composed of a system of multi electrodes with 1280 wires covering a 2θ range of 128 °.

A germanium monochromator was used to obtained a wavelength of 1.28 Å. Additionally, a cryofurnace achieving up to 550 K was used during our measurements.

D9 - Hot Neutron Four-circle Diffractometer (ILL) :
The diffractometer D9 is used for precise and accurate measurements of Bragg intensities up to very high momentum transfer.

The monochromator is a Cu crystal in transmission geometry using the (220) planes. In its standard 'four-circle' geometry the sample holder is an Eulerian cradle

(See Figure B.3). Two circles, denoted φ and χ, are used to adjust the crystal orientation relative to the diffractometer axes. A third circle, ω, sets the orientation of the crystal lattice planes to the diffraction position. Finally, the fourth circle 2θ, rotates the detector to the diffracted beam.

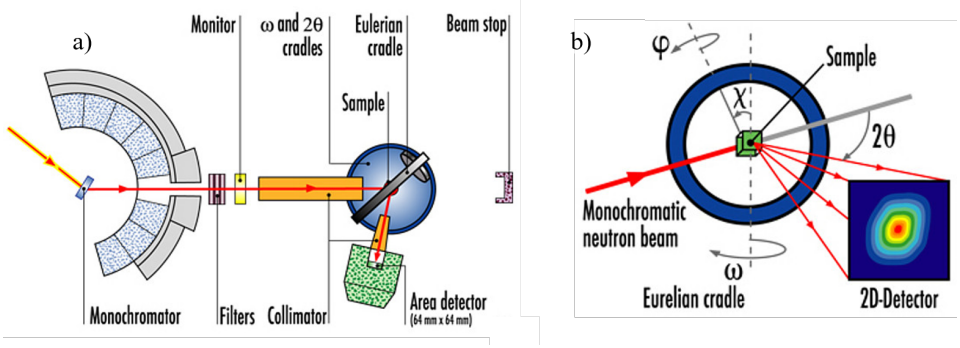

Figure B.3: Schematic of the instrument D9 used at the ILL. (b) Schematic of the 'four-circle' geometry.[155]

The instrument is also equipped with a furnace mounted on the φ circle of the eulerian cradle.

The measurements were carried out using a wavelenght of 0.5 Å and measuring at temperatures of 250, 400 and 540 K.

D3 - The Spin Polarised Hot Neutron Beam Facility (ILL) :
The diffractometer uses readily exchangeable CoFe and Heusler polarizing monochromators within removable shielded cassettes in a symmetric Laue geometry. This polarizing monochromator diffracts only the neutrons with a selected wavelength and spin polarization which is mantained until the cryoflipper.

For measurements carried out with an applied magnetic field a high field configuration was used (See Figure B.4). The polarization reversal is made with a cryoflipper for which the efficiency is wavelength and field independent. A pneumatic half-shutter system in front of the 5 cm diameter single 3 He detector facilitates the determination of the exact orientation matrix for the crystal.

In the high field configuration the sample is in a magnetic field and is cooled down or warmed up in a cryostat. For each Bragg reflection, the peak intensity depends on each polarization state of the beam. A Fourier component of the magnetization distribution in the crystal is obtained from the two intensities.

The measurements in the present work were performed in an applied field of 7

T, using a wavelenght of 0.85 Å. The sample was measured at 300, 400 and 540 K. These temperatures were selected to deteremine the magnetic contributions at the ferromagnetic martensite and the ferromagnetic and paramagnetic austenites.

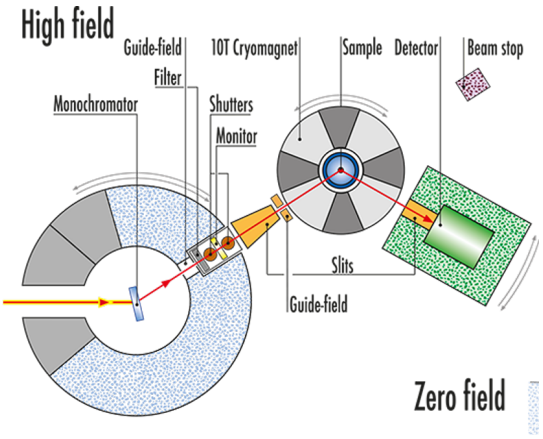

Figure B.4: Schematic of the instrument D3 (ILL) in the high field configuration used.[155]

B.1.2 Scanning Electron Microscopy

Scanning electron microscopy is a common technique used for materials characterization that provides information about the surface or near surface structure, composition, and defects in bulk materials.

The primary function of the scanning electron microscope (SEM) is to enlarge small features by using a high energy electron beam. The main advantage of this technique compared with optical microscopy is the higher resolution that it exhibits due to the shorter wavelength of the electrons. Nowadays a SEM can magnify objects up to one million times their original size and can resolve features smaller than 1 nm in dimension.[156,157]

The first stage in a SEM is the generation of the electrom beam. In some kind of microscopes, it is produced by the thermoionic emission of a W or LaB_6 filament. Other microscopes are equipped with field emission guns which release the electrons by an electric potential in a cold W cathode or a thermally assisted Schottky type W-ZrO_2 emitter. The electrons are accelerated and focused into a small diameter probe by electromagnetic lenses located within the column. The scan coils traced the probe along the sample's surface. The gun, the column, and the specimen chamber are kept under vacuum to allow electron beam generation and advancement.

The image is formed by the interaction of the electron beam and the specimen. This interaction generates a variety of signals such as secondary and backscattered electrons and characteristic X-rays that are collected and processed to obtain images and chemistry of the specimen surface.

SEM experiments were performed on a Schottky-type field emission (JEOL JSM-7000F) at the SGiker services of the University of Basque Country, UPV/EHU, by Dr. Sergio Férnandez. The accelerating voltage is variable between 0.5KV and 30KV. It is equipped with a secondary and backscattered electron detectors, a INCA EDX detector X-sight Serie Si (Li) pentaFET Oxford, and a EBSD detector premium HKL Nordlys II. Additionally, a Hitachi TM-3000 scanning electron microscope with W thermoionic emissiong gun and directional backscattered detector at accelerating voltages from 5 to 15KV was also used.

Energy dispersive X-Ray Spectroscopy

The analysis of characteristic x-rays to provide chemical information is the most widely used microanalytical technique in the SEM.

X-ray signals are typically produced when a primary beam electron causes the ejection of an inner shell electron, i.e., the K, L and M shells, from the sample. To fill the vacancy of the ejected electron, an electron from an outer shell transits, given off an x-ray whose energy can be related to the difference in energies of the two electron orbitals involved. The emitted radiation reaches a detector where the energy and intensity of the X-rays are measured enabling the formation of a spectrum. To accurately quantify the composition from the spectrum, the spectrometer is calibrated by using standard samples of known composition.

Electron backscattered diffraction, EBSD

The electron backscatter diffraction (EBSD) technique provides quantitative microstructural information about the crystallographic nature of materials. It can also give information about grain size, grain boundary character, grain orientation, texture, and phase identity of the sample under the beam. For this technique the specimen is tilted at approx. 70° from the normal position. High accelerating voltage such as 20 kV are normally used. When the primary beam interacts with the crystal lattice part of the high energy backscattered electrons are scattered in a manner that satisfies the Bragg's law. For each set of lattice panes for which Bragg condition is

fulfilled, the diffracted beam emerge out of the specimen in all directions in a cone form. Two cones are formed for each set of lattice planes, one at the front and the second at the rear of the lattice plane. If a phosphor screen is placed a short distance from the tilted sample, the different cones formed from each lattice planes intersect the screen and form sets of straight lines, known as Kikuchi pattern (See Figure B.5). Every set of two parallel lines represent a family of parallel planes with a specific value of d-spacing. Indexing of Kikuchi patterns is done using an specific software which is used to calculate structural information and determine grain orientation.

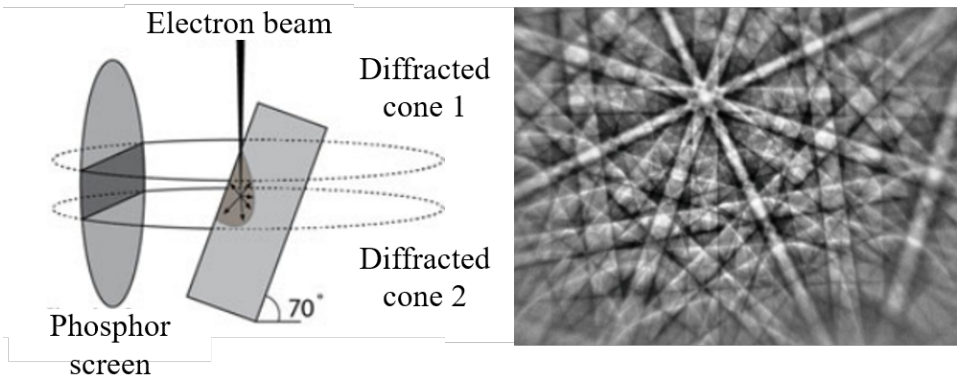

Figure B.5: Schematic illustration of the intersection of the diffraction cones giving rise to Kikuchi bands on a phosphor screen (e) Example of a Kikuchi pattern. Figure adapted from[156]

B.2 Thermal characterization

B.2.1 Differential Scanning Calorimetry

The Differential Scanning Calorimetry measures the change of the difference in the heat flow rate to the sample and to a reference sample while they are subjected to a controlled temperature program.[158] Two basic types of Differential Scanning Calorimeters (DSCs) are distinguished, depending on the signal type measured: a) The heat flux DSC and b) The power compensation DSC.

In the heat flux DSC a defined exchange of the heat to be measured with the environment takes place via a well-defined heat conduction path with given thermal resistance. The primary measurement signal is a temperature difference; it determines the intensity of the exchange and the resulting heat flow rate is proportional

to it.
In the case of the power compensated DSC the measured heat is compensated with electric energy. The measuring system consists of two identical microfurnaces, each one with a temperature sensor, located inside a thermostated aluminum block. During a measurement, the same heating power is supplied to both microfurnaces via a control circuit to follow the specific heatng rate. When a transition or reaction occurs a temperature difference results between both microfurnaces. The temperature difference is both the measurement signal and the input signal of a second control circuit. This second circuit compensates most of the reaction heat flow rate by proportional control by increasing or decreasing an additional heating power of the sample furnace. The compensating heating power is proportional to the remaining temperature difference.

The Differential Scanning Calorimetry (DSC) has been used to determine the phase transformation temperatures of the samples. The martensitic transformation temperatures have been determined by two different equipments, a Mettler Toledo DSC and a PerkinElmer Diamond calorimeter (See Figure B.6). The heating and cooling rate used was defined between 5-20 K/min. The temperature range was from 123 to 823 K.

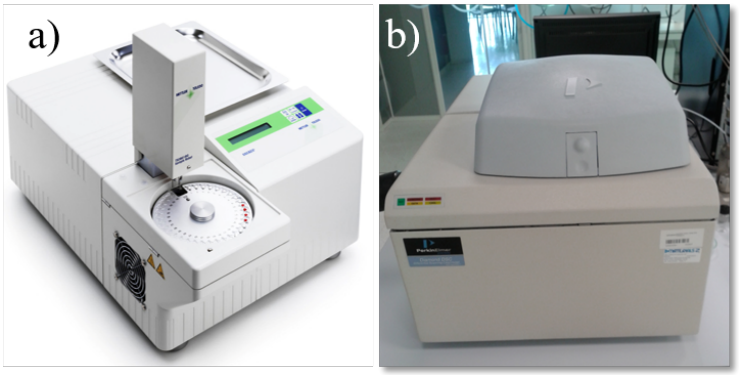

Figure B.6: Mettler Toledo 822e DSC (a) and the PerkinElmer Diamond used in this work.

B.3 Mechanical characterization

B.3.1 Dynamic Mechanical Analyzer

Dynamic Mechanical Analysis provides information on the transformation behavior of the samples under a static stress. The dynamic mechanical analysis, DMA, can be simply described as applying an oscillating force to a sample and analyzing the material's response to that force. The DMA supplies an oscillatory force, causing a sinusoidal stress to be applied to the sample, which generates a sinusoidal strain. By measuring both, the amplitude of deformation at the peak of the sine wave and the lag between the strain and stress sin waves, quantities as the modulus, the viscosity and the damping can be calculated.[159]

Two different tests were carried out on a Dynamic Mechanical Analyzer (DMA1, Mettler Toledo). On the one hand, a quasi-static tensile cycling test has been performed. The specimens were subjected to a constant mechanical stress up to 5–10 N during the testing. The temperature range for the thermal cycling was chosen so that it would cover the full transformation range of the samples. The temperature rate was set at 20 K/min in both heating and cooling. On the other hand, before and after the samples cycling a dynamic tensile test of temperature dependence of elastic modulus and tan δ was performed. For this measurement a 1 Hz sinusoidal deformation is applied during the heating and cooling of the specimen at 20 K/min. The samples were tested controlling the strain to a peak value of 10^{-4} while the stress was measured.

B.3.2 Mechanical Testing Machine

Mechanical tests were performed to characterize principally two mechanical properties: the twinning strain, which determines the maximum (or theoretical) strain that can be obtained by variant reorientation, and the twinning stress, which determines the minimal stress that is required for variant reorientation.

The most common type of test used to measure the mechanical properties of a material is the tension test. In a typical tension test a metallic specimen of specified dimensions is pulled under the action of uniaxial forces applied at both ends until the specimen undergoes fracture. While the applied uniaxial load is continuously

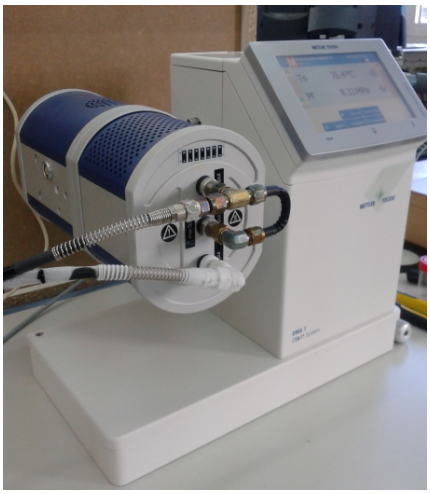

Figure B.7: The DMA 1 Mettler Toledo used for the quasi-static and dynamic mechanical measurements

increasing, the elongation in the specimen is recorded, such that at the end of the test a set of data for corresponding readings of load and displacement values are obtained. Several aspects should be taken into account when planning a mechanical test for Ni-Mn-Ga alloys. First, due to the small sample dimensions and relatively small twinning stress values, the applied loads are typically in the range of few Newtons or even smaller and therefore load-cells with high resolution and sensitivity are required. Second, Ni-Mn-Ga single crystals cannot be cut into dog-bone shapes as required for standard tensile tests. Therefore, most tests are performed under compression.[160]

The equipment utilized for mechanical tests was an MTS Criterion C43.104 mechanical testing machine with a load cell of 5kN, located at the Lappeenranta University of Technology. A temperature chamber was developed and adapted to the equipment.

B.4 Magnetic characterization

B.4.1 Vibrating Sample Magnetometer

A homemade Vibrating Sample Magnetometer has been used to measure the magnetic moment of the samples as a function of the temperature and the applied magnetic field.

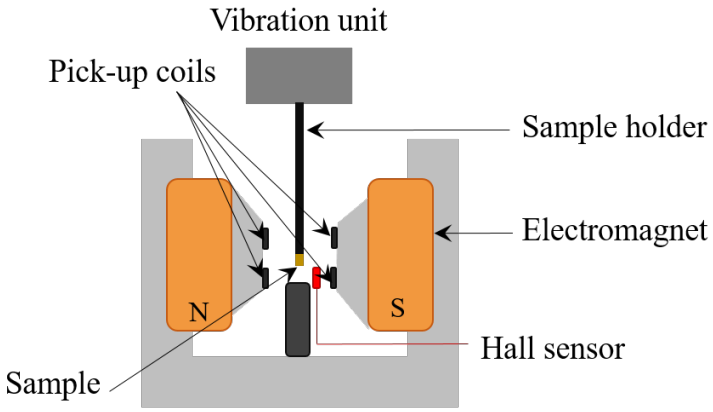

Figure B.8: Schematic operation of a VSM

Vibrating Sample Magnetometry (VSM) systems are used to measure the magnetic properties of materials as a function of magnetic field, temperature, and time. This technique is based on Faraday's law, which states that an electromagnetic force is generated in a coil when there is a change in flux through the coil. In the measurement setup, the sample is located in the air gap of an electromagnet and four detection coils are placed in its surroundings. If the sample is vibrating with sinusoidal motion within the suitably placed pick-up coils in a magnetic field, a sinusoidal electrical signal will be induced in these coils. The voltage, V, presents the same frequency as the sample vibration and its amplitude is proportional to the magnetic moment, the amplitude, and the relative position with respect to the pick-up coils system. The oscillator provides a sinusoidal signal that is translated by the transducer assembly into a vertical vibration, perpendicular to the magnetic field. The sample is fixed to a non-magnetic sample holder and vibrates with a given frequency (63 Hz is used because the first common harmonic with the 50 Hz electrical supply frequency would be 3150 Hz and therefore will add little noise to the measurement) and amplitude, inducing a signal in the pick-up coils described by this equation.

$$V = -NS\frac{dB}{dT} = -NS\frac{d(B_{ext} + g(t)\Delta m)}{dt} \tag{B.3}$$

where g(t) is related to the position of the sample, N, is the number of wire turns in the coil, S, the transversal coil area and, m, the magnetic moment of the sample. Since the field used to magnetize the sample is stationary relative to the pick-up coils all the signal is only generated by the magnetization of the sample, and M vs.

H curves can be measured directly.[161] The induced voltage is measured through a lock-in amplifier using the voice coil drive signal as its reference. The electromagnet used generates a magnetic field up to ± 1.8 T. In the VSM, the temperature can be varied from 123 K to 773 K by a continuous N2 gas flux circulating through a liquid N2 vessel and a heating electric resistance. A schematic drawing of the VSM sample holder and detection mechanism of VSM is shown in Figure B.8

Bibliography

[1] N. Lanska, O. Söderberg, A. Sozinov, Y. Ge, K. Ullakko, and V. Lindroos, "Composition and temperature dependence of the crystal structure of Ni–Mn–Ga alloys," *Journal of Applied Physics*, vol. 95, no. 12, pp. 8074–8078, 2004.

[2] B. Jaffe, R. S. Roth, and S. Marzullo, "Piezoelectric Properties of Lead Zirconate–Lead Titanate Solid–Solution Ceramics," *Journal of Applied Physics*, vol. 25, pp. 809–810, June 1954.

[3] Robert C. O'Handley, *Modern Magnetic Materials: Principles and Applications*. New York: Wiley, 2000.

[4] M. B. Moffett, A. E. Clark, M. Wun-Fogle, J. Linberg, J. P. Teter, and E. A. McLaughlin, "Characterization of Terfenol-D for magnetostrictive transducers," *The Journal of the Acoustical Society of America*, vol. 89, no. 3, pp. 1448–1455, 1991.

[5] A. Ölander, "An electrochemical investigation of solid Cadmium-Gold alloys," *Journal of the American Chemical Society*, vol. 54, pp. 3819–3833, Oct. 1932.

[6] W. J. Buehler, J. V. Gilfrich, and R. C. Wiley, "Effect of Low-Temperature Phase Changes on the Mechanical Properties of Alloys near Composition TiNi," *Journal of Applied Physics*, vol. 34, pp. 1475–1477, May 1963.

[7] J. Mohd Jani, M. Leary, A. Subic, and M. A. Gibson, "A review of shape memory alloy research, applications and opportunities," *Materials & Design (1980-2015)*, vol. 56, pp. 1078–1113, Apr. 2014.

[8] J. Cui, "Shape Memory Alloys and Their Applications in Power Generation and Refrigeration," in *Mesoscopic Phenomena in Multifunctional Materials*, Springer Series in Materials Science, pp. 289–307, Springer, Berlin, Heidelberg, 2014.

[9] M. H. Wu and L. M. Schetky, "Proceedings of the International Conference on Shape Memory and Superelastic Technolgies, Pacific Grove, California, P.171-182 (2000).," p. 9.

[10] Y. Bellouard, "Shape memory alloys for microsystems: A review from a material research perspective," *Materials Science and Engineering: A*, vol. 481-482, pp. 582–589, May 2008.

[11] D. Stoeckel, "Shape memory actuators for automotive applications," *Materials & Design*, vol. 11, pp. 302–307, Dec. 1990.

[12] R. Pecora and I. Dimino, "SMA for Aeronautics," in *Shape Memory Alloy Engineering*, pp. 275–304, Elsevier, 2015.

[13] P. B. Leal and M. A. Savi, "Shape memory alloy-based mechanism for aeronautical application: Theory, optimization and experiment," *Aerospace Science and Technology*, vol. 76, pp. 155–163, May 2018.

[14] F. Auricchio, E. Boatti, and M. Conti, "SMA Biomedical Applications," in *Shape Memory Alloy Engineering*, pp. 307–341, Elsevier, 2015.

[15] B. O'Brien, F. M. Weafer, and M. S. Bruzzi, "1.3 Shape Memory Alloys for Use in Medicine," in *Comprehensive Biomaterials II* (P. Ducheyne, ed.), pp. 50–78, Oxford: Elsevier, 2017.

[16] T. Yoneyama and S. Miyazaki, *Shape Memory Alloys for Biomedical Applications*. Elsevier, Nov. 2008. Google-Books-ID: eu2iAgAAQBAJ.

[17] G. Lange, A. Lachmann, A. H. A. Rahim, M. H. Ismail, and C. Y. Low, "Shape Memory Alloys as Linear Drives in Robot Hand Actuation," *Procedia Computer Science*, vol. 76, pp. 168–173, 2015.

[18] M. Sreekumar, T. Nagarajan, M. Singaperumal, M. Zoppi, and R. Molfino, "Critical review of current trends in shape memory alloy actuators for intelligent robots," *Industrial Robot: An International Journal*, vol. 34, pp. 285–294, June 2007.

[19] M. O. Gök, M. Z. Bilir, and B. H. Gürcüm, "Shape Memory Applications in Textile Design," *Procedia - Social and Behavioral Sciences*, vol. 195, pp. 2160–2169, July 2015.

[20] K. Ullakko, J. K. Huang, C. Kantner, R. C. O'Handley, and V. V. Kokorin, "Large magnetic–field–induced strains in Ni $_2$ MnGa single crystals," *Applied Physics Letters*, vol. 69, pp. 1966–1968, Sept. 1996.

[21] V. A. Chernenko, E. Cesari, V. V. Kokorin, and I. N. Vitenko, "The Development of New Ferromagnetic Shape Memory Alloys in Ni-Mn-Ga System," *Scripta Metallurgica et Materialia*, vol. 33, no. 8, pp. 1239–1244, 1995.

[22] E. Faran and D. Shilo, "Ferromagnetic shape memory alloys challenges, applications, and experimental characterization," *Experimental Techniques*, 2015.

[23] R. M. Bozorth, *Ferromagnetism*. 1993.

[24] L. Straka, J. Drahokoupil, O. Pacherová, K. Fabiánová, V. Kopeckỳ, H. Seiner, H. Hänninen, and O. Heczko, "The relation between lattice parameters and very low twinning stress in $Ni_{50}Mn_{25+x}Ga_{25-x}$ magnetic shape memory alloys," *Smart Materials and Structures*, vol. 25, no. 2, p. 025001, 2015.

[25] M. Zelenỳ, A. Sozinov, L. Straka, T. Björkman, and R. M. Nieminen, "First-principles study of Co-and Cu-doped Ni_2MnGa along the tetragonal deformation path," *Physical Review B*, vol. 89, no. 18, p. 184103, 2014.

[26] M. Rameš, O. Heczko, A. Sozinov, K. Ullakko, and L. Straka, "Magnetic properties of Ni–Mn–Ga-Co-Cu tetragonal martensites exhibiting magnetic shape memory effect," *Scripta Materialia*, vol. 142, pp. 61–65, 2018.

[27] F. Albertini, L. Morellon, P. A. Algarabel, M. R. Ibarra, L. Pareti, Z. Arnold, and G. Calestani, "Magnetoelastic effects and magnetic anisotropy in Ni_2MnGa polycrystals," *Journal of Applied Physics*, vol. 89, pp. 5614–5617, May 2001.

[28] A. Likhachev, A. Sozinov, and K. Ullakko, "Modeling the strain response, magneto-mechanical cycling under the external stress, work output and energy losses in Ni–Mn–Ga," *Mechanics of materials*, vol. 38, no. 5-6, pp. 551–563, 2006.

[29] F. Heusler, "Magnetic manganese alloys," *Verhandl Deuts Phys Ges*, vol. 5, p. 219, 1903.

[30] A. Sozinov, N. Lanska, A. Soroka, and W. Zou, "12% magnetic field-induced strain in Ni-Mn-Ga based non-modulated martensite," *Applied Physics Letters*, vol. 102, p. 021902, Jan. 2013.

[31] E. Pagounis, R. Chulist, M. Szczerba, and M. Laufenberg, "High-temperature magnetic shape memory actuation in a Ni–Mn–Ga single crystal," *Scripta Materialia*, vol. 83, pp. 29–32, July 2014.

[32] O. Heczko, L. Straka, N. Lanska, K. Ullakko, and J. Enkovaara, "Temperature dependence of magnetic anisotropy in Ni–Mn–Ga alloys exhibiting giant field-induced strain," *Journal of Applied Physics*, vol. 91, no. 10, p. 8228, 2002.

[33] O. Söderberg, A. Sozinov, Y. Ge, S. Hannula, and V. Lindroos, "Giant magnetostrictive materials," *Handbook of magnetic materials*, vol. 16, pp. 1–40, 2006.

[34] M. Acet, L. Mañosa, and A. Planes, *Magnetic-field-induced effects in martensitic Heusler-based magnetic shape memory alloys*, vol. 19. Elsevier, 2011.

[35] A. Sozinov, A. A. Likhachev, and K. Ullakko, "Crystal structures and magnetic anisotropy properties of Ni-Mn-Ga martensitic phases with giant magnetic-field-induced strain," *IEEE Transactions on Magnetics*, vol. 38, pp. 2814–2816, Sept. 2002.

[36] P. Müllner, V. A. Chernenko, and G. Kostorz, "Large cyclic magnetic field-induced deformation in orthorhombic (14M) Ni–Mn–Ga martensite," *Journal of Applied Physics*, vol. 95, pp. 1531–1536, Feb. 2004.

[37] J. Ma, I. Karaman, and R. D. Noebe, "High temperature shape memory alloys," *International Materials Reviews*, vol. 55, pp. 257–315, Sept. 2010.

[38] G. Firstov, J. Van Humbeeck, and Y. N. Koval, "High temperature shape memory alloys problems and prospects," *Journal of intelligent material systems and structures*, vol. 17, no. 12, pp. 1041–1047, 2006.

[39] G. Firstov, J. Van Humbeeck, and Y. N. Koval, "High-temperature shape memory alloys: some recent developments," *Materials Science and Engineering: A*, vol. 378, no. 1-2, pp. 2–10, 2004.

[40] J. Van Humbeeck, "High temperature shape memory alloys," *Transactions-American Society of Mechanical Engineers Journal of Engineering Materials and Technology*, vol. 121, pp. 98–101, 1999.

[41] V. A. Chernenko, "Compositional instability of β-phase in Ni-Mn-Ga alloys," *Scripta Materialia*, vol. 40, no. 5, pp. 523–527, 1999.

[42] O. Söderberg, Y. Ge, A. Sozinov, S.P. Hannula, V.K. Lindroos,, *Handbook of Magnetic Materials,*, vol. 16. Amsterdam: Elsevier Science, k.h.j. buschow ed., 2006.

[43] X. Jin, M. Marioni, D. Bono, S. M. Allen, R. C. O'Handley, and T. Y. Hsu, "Empirical mapping of Ni–Mn–Ga properties with composition and valence electron concentration," *Journal of Applied Physics*, vol. 91, no. 10, p. 8222, 2002.

[44] K. Rolfs, M. Chmielus, J. M. Guldbakke, R. C. Wimpory, A. Raatz, W. Petry, P. Müllner, and R. Schneider, "Key Properties of Ni-Mn-Ga Based Single Crystals Grown with the SLARE Technique," *Advanced Engineering Materials*, vol. 14, pp. 614–635, Aug. 2012.

[45] V. Chernenko, E. Villa, S. Besseghini, and J. Barandiaran, "Giant two-way shape memory effect in high temperature Ni–Mn–Ga single crystal," *Physics Procedia*, vol. 10, pp. 94–98, 2010.

[46] V. A. L'vov, A. Kosogor, J. M. Barandiaran, and V. A. Chernenko, "Destabilization of Ni–Mn–Ga martensite: Experiment and theory," *Acta Materialia*, vol. 60, pp. 1587–1593, Feb. 2012.

[47] V. Chernenko, V. L'vov, S. Zagorodnyuk, and T. Takagi, "Ferromagnetism of thermoelastic martensites: Theory and experiment," *Physical Review B*, vol. 67, no. 6, p. 064407, 2003.

[48] J. Ma, I. Karaman, and R. D. Noebe, "High temperature shape memory alloys," *International Materials Reviews*, vol. 55, pp. 257–315, Sept. 2010.

[49] G. S. Firstov, J. Van Humbeeck, and Y. N. Koval, "Comparison of high temperature shape memory behaviour for ZrCu-based, Ti–Ni–Zr and Ti–Ni–Hf alloys," *Scripta Materialia*, vol. 50, pp. 243–248, Jan. 2004.

[50] P. J. S. Buenconsejo, H. Y. Kim, H. Hosoda, and S. Miyazaki, "Shape memory behavior of Ti–Ta and its potential as a high-temperature shape memory alloy," *Acta Materialia*, vol. 57, pp. 1068–1077, Feb. 2009.

[51] J. Van Humbeeck, "Shape memory alloys with high transformation temperatures," *Materials Research Bulletin*, vol. 47, no. 10, pp. 2966–2968, 2012.

[52] K. Otsuka and C. M. Wayman, *Shape Memory Materials*. Cambridge University Press, Oct. 1999. Google-Books-ID: DvItE9XUlN8C.

[53] R. Santamarta, E. Cesari, J. Muntasell, J. Font, J. Pons, and P. Ochin, "Thermal and microstructural evolution under ageing of several high-temperature Ni–Mn–Ga alloys," *Intermetallics*, vol. 18, pp. 977–983, May 2010.

[54] A. Pérez-Sierra, J. Pons, R. Santamarta, I. Karaman, and R. Noebe, "Stability of a Ni-rich Ni-Ti-Zr high temperature shape memory alloy upon low temperature aging and thermal cycling," *Scripta Materialia*, vol. 124, pp. 47–50, 2016.

[55] C. Wedel and K. Itagaki, "High-temperature phase relations in the ternary Ga-Mn-Ni system," *Journal of Phase Equilibria and Diffusion*, vol. 22, no. 3, p. 324, 2001.

[56] D. Schlagel, Y. Wu, W. Zhang, and T. Lograsso, "Chemical segregation during bulk single crystal preparation of Ni–Mn–Ga ferromagnetic shape memory alloys," *Journal of Alloys and Compounds*, vol. 312, pp. 77–85, Nov. 2000.

[57] C. Segui, E. Cesari, J. Pons, and V. Chernenko, "Internal friction behaviour of Ni–Mn–Ga," *Materials Science and Engineering: A*, vol. 370, no. 1-2, pp. 481–484, 2004.

[58] E. Cesari, V. Chernenko, V. Kokorin, J. Pons, and C. Segui, "Internal friction associated with the structural phase transformations in Ni–Mn–Ga alloys," *Acta materialia*, vol. 45, no. 3, pp. 999–1004, 1997.

[59] M. Zemansky and D. Dittman, *Heat and thermodynamics, 1997*, vol. 10020.

[60] H. B. Callen, "Thermodynamics and an introduction to thermostatistics," 1998.

[61] D. Y. Cong, G. Saha, and M. R. Barnett, "Thermomechanical properties of Ni–Ti shape memory wires containing nanoscale precipitates induced by stress-assisted ageing," *Acta Biomaterialia*, vol. 10, pp. 5178–5192, Dec. 2014.

[62] C. KE, S. Cao, X. MA, and X. Zhang, "Modeling of Ni_4Ti_3 precipitation during stress-free and stress-assisted aging of bi-crystalline NiTi shape memory alloys," *Transactions of Nonferrous Metals Society of China*, vol. 22, no. 10, pp. 2578–2585, 2012.

[63] J. P. Liu, E. Fullerton, O. Gutfleisch, and D. Sellmyer, eds., *Nanoscale Magnetic Materials and Applications*. Boston, MA: Springer US, 2009.

[64] V. A. Chernenko, M. Chmielus, and P. Müllner, "Large magnetic-field-induced strains in Ni–Mn–Ga nonmodulated martensite," *Applied Physics Letters*, vol. 95, p. 104103, Sept. 2009.

[65] A. Sozinov, A. Soroka, N. Lanska, M. Rameš, L. Straka, and K. Ullakko, "Temperature dependence of twinning and magnetic stresses in $Ni_{46}Mn_{24}Ga_{22}Co_4Cu_4$ alloy with giant 12% magnetic field-induced strain," *Scripta Materialia*, vol. 131, pp. 33–36, 2017.

[66] C.-M. Li, H.-B. Luo, Q.-M. Hu, R. Yang, B. Johansson, and L. Vitos, "Site preference and elastic properties of Fe-, Co-, and Cu-doped Ni 2 MnGa shape memory alloys from first principles," *Physical Review B*, vol. 84, July 2011.

[67] C. Tan, G. Dong, L. Gao, J. Sui, Z. Gao, and W. Cai, "Microstructure, martensitic transformation and mechanical properties of $Ni_{50}Mn_{30}Ga_{20-x}Cu_x$ ferromagnetic shape memory alloys," *Journal of Alloys and Compounds*, vol. 538, pp. 1–4, 2012.

[68] K. Koho, O. Söderberg, N. Lanska, Y. Ge, X. Liu, L. Straka, J. Vimpari, O. Heczko, and V. Lindroos, "Effect of the chemical composition to martensitic transformation in Ni–Mn–Ga–Fe alloys," *Materials Science and Engineering: A*, vol. 378, pp. 384–388, July 2004.

[69] D. E. Soto-Parra, X. Moya, L. Mañosa, A. Planes, H. Flores-Zúñiga, F. Alvarado-Hernández, R. A. Ochoa-Gamboa, J. A. Matutes-Aquino, and D. Ríos-Jara, "Fe and Co selective substitution in Ni_2MnGa: Effect of magnetism on relative phase stability," *Philosophical Magazine*, vol. 90, pp. 2771–2792, July 2010.

[70] R. Singh, M. M. Raja, R. Mathur, and M. Shamsuddin, "Studies on ferromagnetic shape memory Ni–Mn–Ga alloys with Fe and rare-earths additives," *Journal of Alloys and Compounds*, vol. 506, pp. 73–76, Sept. 2010.

[71] J. Bai, J.-M. Raulot, Y. Zhang, C. Esling, X. Zhao, and L. Zuo, "The effects of alloying element co on Ni-Mn-Ga ferromagnetic shape memory alloys from first-principles calculations," *Applied Physics Letters*, vol. 98, no. 16, p. 164103, 2011.

[72] A. Soroka, A. Sozinov, N. Lanska, M. Rameš, L. Straka, and K. Ullakko, "Composition and temperature dependence of twinning stress in non-modulated martensite of Ni–Mn–Ga-Co-Cu magnetic shape memory alloys," *Scripta Materialia*, vol. 144, pp. 52–55, 2018.

[73] M. Zelený, A. Sozinov, T. Björkman, L. Straka, and R. Nieminen, "Ab Initio Study of Properties of Co- and Cu- Doped Ni-Mn-Ga Alloys," *Materials Today: Proceedings*, vol. 2, pp. S601–S604, 2015.

[74] V. Seshubai, A. S. Kumar, and M. Ramudu, "Influence of site occupancy on the structure, microstructure and magnetic properties of ternary and quasi-ternary alloys of Ni-Mn-Ga," pp. 74–86, 2012.

[75] Y. Li, J. Wang, and C. Jiang, "Study of Ni–Mn–Ga–Cu as single-phase wide-hysteresis shape memory alloys," *Materials Science and Engineering: A*, vol. 528, pp. 6907–6911, Aug. 2011.

[76] M. Kataoka, K. Endo, N. Kudo, T. Kanomata, H. Nishihara, T. Shishido, R. Umetsu, M. Nagasako, and R. Kainuma, "Martensitic transition, ferromagnetic transition, and their interplay in the shape memory alloys $Ni_2Mn_{1-x}Cu_xGa$," *Physical Review B*, vol. 82, no. 21, p. 214423, 2010.

[77] P.-P. Li, J.-M. Wang, and C.-B. Jiang, "Martensitic transformation in Cu-doped NiMnGa magnetic shape memory alloys," *Chinese Physics B*, vol. 20, p. 028104, Feb. 2011.

[78] R. Singh, M. Manivel Raja, R. Mathur, and M. Shamsuddin, "Effect of Fe substitution on the phase stability and magnetic properties of Mn-rich Ni–Mn–Ga ferromagnetic shape memory alloys," *Journal of Magnetism and Magnetic Materials*, vol. 323, pp. 574–578, Mar. 2011.

[79] S. K. Ayila, R. Machavarapu, and S. Vummethala, "Site preference of magnetic atoms in Ni-Mn-Ga-M (M = Co, Fe) ferromagnetic shape memory alloys," *physica status solidi (b)*, vol. 249, pp. 620–626, Mar. 2012.

[80] V. V. Khovailo, T. Abe, V. V. Koledov, M. Matsumoto, H. Nakamura, R. Note, M. Ohtsuka, V. G. Shavrov, and T. Takagi, "Influence of Fe and Co on phase transitions in Ni-Mn-Ga alloys," *Materials transactions*, vol. 44, no. 12, pp. 2509–2512, 2003.

[81] H. Kato and K. Sasaki, "Avoiding error of determining the martensite finish temperature due to thermal inertia in differential scanning calorimetry: model

and experiment of Ni–Ti and Cu–Al–Ni shape memory alloys," *Journal of Materials Science*, vol. 47, pp. 1399–1410, Feb. 2012.

[82] D. Kikuchi, T. Kanomata, Y. Yamaguchi, H. Nishihara, K. Koyama, and K. Watanabe, "Magnetic properties of ferromagnetic shape memory alloys $Ni_2Mn_{1-x}Fe_xGa$," *Journal of alloys and compounds*, vol. 383, no. 1-2, pp. 184–188, 2004.

[83] V. Chernenko, V. L'vov, E. Cesari, J. Pons, R. Portier, and S. Zagorodnyuk, "New Aspects of Structural and Magnetic Behaviour of Martensites in Ni–Mn–Ga Alloys," *Materials Transactions*, vol. 43, no. 5, pp. 856–860, 2002.

[84] J. Pons, V. A. Chernenko, R. Santamarta, and E. Cesari, "Crystal structure of martensitic phases in Ni-Mn-Ga shape memory alloys," *Acta Materialia*, vol. 48, no. 12, pp. 3027–3038, 2000.

[85] Y. Sutou, Y. Imano, N. Koeda, T. Omori, R. Kainuma, K. Ishida, and K. Oikawa, "Magnetic and martensitic transformations of NiMnX (X= In, Sn, Sb) ferromagnetic shape memory alloys," *Applied Physics Letters*, vol. 85, no. 19, pp. 4358–4360, 2004.

[86] A. Arrott, "Criterion for ferromagnetism from observations of magnetic isotherms," *Physical Review*, vol. 108, no. 6, p. 1394, 1957.

[87] O. Heczko, S. Fähler, T. M. Vasilchikova, T. N. Voloshok, K. V. Klimov, Y. I. Chumlyakov, and A. N. Vasiliev, "Thermodynamic, kinetic, and magnetic properties of a $Ni_{54}Fe_{19}Ga_{27}$ magnetic shape-memory single crystal," *Physical Review B*, vol. 77, May 2008.

[88] P. J. Webster, K. R. A. Ziebeck, S. L. Town, and M. S. Peak, "Magnetic order and phase transformation in Ni $_2$ MnGa," *Philosophical Magazine Part B*, vol. 49, pp. 295–310, Mar. 1984.

[89] Z. H. Liu, M. Zhang, W. Q. Wang, W. H. Wang, J. L. Chen, G. H. Wu, F. B. Meng, H. Y. Liu, B. D. Liu, J. P. Qu, and Y. X. Li, "Magnetic properties and martensitic transformation in quaternary Heusler alloy of NiMnFeGa," *Journal of Applied Physics*, vol. 92, pp. 5006–5010, Nov. 2002.

[90] W. Jun, X. Ren, C. Le-Yi, T. Yan-Mei, X. Lian-Qiang, T. Shao-Long, and D. You-Wei, "Relation between martensitic transformation temperature range and lattice distortion ratio of NiMnGaCoCu Heusler alloys," *Chinese Physics B*, vol. 23, no. 4, p. 048107, 2014.

[91] Y. Ma, C. Jiang, Y. Li, H. Xu, C. Wang, and X. Liu, "Study of $Ni_{50+x}Mn_{25}Ga_{25-x}$ (x= 2–11) as high temperature shape memory alloys," *Acta materialia*, vol. 55, no. 5, pp. 1533–1541, 2007.

[92] M. Zelený, A. Sozinov, T. Björkman, L. Straka, O. Heczko, and R. M. Nieminen, "Effect of Magnetic Ordering on the Stability of Ni–Mn–Ga–Co–Cu) Alloys Along the Tetragonal Deformation Path," *IEEE Transactions on Magnetics*, vol. 53, pp. 1–6, Nov. 2017.

[93] G. J. Li, E. K. Liu, H. G. Zhang, Y. J. Zhang, G. Z. Xu, H. Z. Luo, H. W. Zhang, W. H. Wang, and G. H. Wu, "Role of covalent hybridization in the martensitic structure and magnetic properties of shape-memory alloys: The case of $Ni_{50}Mn_{5+x}Ga_{35-x}Cu_{10}$," *Applied Physics Letters*, vol. 102, p. 062407, Feb. 2013.

[94] M. Zelenỳ, A. Sozinov, T. Björkman, L. Straka, and R. Nieminen, "Ab initio study of properties of Co-and Cu-doped Ni–Mn–Ga alloys," *Materials Today: Proceedings*, vol. 2, pp. S601–S604, 2015.

[95] S. Roy, E. Blackburn, S. Valvidares, M. Fitzsimmons, S. Vogel, M. Khan, I. Dubenko, S. Stadler, N. Ali, S. Sinha, *et al.*, "Delocalization and hybridization enhance the magnetocaloric effect in Cu-doped Ni_2MnGa," *Physical Review B*, vol. 79, no. 23, p. 235127, 2009.

[96] A. Pérez-Checa, J. Feuchtwanger, D. Musiienko, A. Sozinov, J. Barandiaran, K. Ullakko, and V. Chernenko, "High temperature $Ni_{45}Co_5Mn_{25-x}Fe_xGa_{20}Cu_5$ ferromagnetic shape memory alloys," *Scripta Materialia*, vol. 134, pp. 119–122, 2017.

[97] M. Zelenỳ, A. Sozinov, T. Björkman, L. Straka, O. Heczko, and R. M. Nieminen, "Effect of magnetic ordering on the stability of Ni–Mn–Ga (–co–cu) alloys along the tetragonal deformation path," *IEEE Transactions on Magnetics*, vol. 53, no. 11, pp. 1–6, 2017.

[98] G. Li, E. Liu, H. Zhang, Y. Zhang, G. Xu, H. Luo, H. Zhang, W. Wang, and G. Wu, "Role of covalent hybridization in the martensitic structure and magnetic properties of shape-memory alloys: The case of $Ni_{50}Mn_{5+x}Ga_{35-x}Cu_{10}$," *Applied Physics Letters*, vol. 102, no. 6, p. 062407, 2013.

[99] I. Galanakis and E. Şaşıoğlu, "Variation of the magnetic properties of Ni_2MnGa heusler alloy upon tetragonalization: a first-principles study," *Journal of Physics D: Applied Physics*, vol. 44, no. 23, p. 235001, 2011.

[100] P. Brown, J. Crangle, T. Kanomata, M. Matsumoto, K.-U. Neumann, B. Ouladdiaf, and K. Ziebeck, "The crystal structure and phase transitions of the magnetic shape memory compound Ni_2MnGa," *Journal of Physics: Condensed Matter*, vol. 14, no. 43, p. 10159, 2002.

[101] M. L. Richard, *Systematic analysis of the crystal structure, chemical ordering, and microstructure of Ni–Mn–Ga ferromagnetic shape memory alloys.* PhD thesis, Massachusetts Institute of Technology, 2005.

[102] M. Richard, J. Feuchtwanger, S. Allen, R. O'handley, P. Lázpita, J. Barandiaran, J. Gutierrez, B. Ouladdiaf, C. Mondelli, T. Lograsso, *et al.*, "Chemical order in off-stoichiometric Ni–Mn–Ga ferromagnetic shape-memory alloys studied with neutron diffraction," *Philosophical Magazine*, vol. 87, no. 23, pp. 3437–3447, 2007.

[103] J. M. Barandiarán, J. Gutiérrez, P. Lázpita, and J. Feuchtwanger, "Neutron diffraction studies of magnetic shape memory alloys," in *Materials Science Forum*, vol. 684, pp. 73–84, Trans Tech Publ, 2011.

[104] V. Sánchez-Alarcos, V. Recarte, J. Pérez-Landazábal, and G. Cuello, "Correlation between atomic order and the characteristics of the structural and magnetic transformations in Ni–Mn–Ga shape memory alloys," *Acta materialia*, vol. 55, no. 11, pp. 3883–3889, 2007.

[105] J. Barandiarán, V. Chernenko, P. Lázpita, J. Gutiérrez, M. Fdez-Gubieda, and A. Kimura, "Neutron and synchrotron studies of structure and magnetism of shape memory alloys," in *Journal of Physics: Conference Series*, vol. 663, p. 012014, IOP Publishing, 2015.

[106] P. Webster, K. Ziebeck, S. Town, and M. Peak, "Magnetic order and phase transformation in Ni_2MnGa," *Philosophical Magazine B*, vol. 49, no. 3, pp. 295–310, 1984.

[107] P. Entel, A. Dannenberg, M. Siewert, H. C. Herper, M. E. Gruner, V. D. Buchelnikov, and V. A. Chernenko, "Composition-dependent basics of smart heusler materials from first-principles calculations," in *Materials Science Forum*, vol. 684, pp. 1–29, Trans Tech Publ, 2011.

[108] D. Comtesse, M. E. Gruner, M. Ogura, V. Sokolovskiy, V. Buchelnikov, A. Grünebohm, R. Arróyave, N. Singh, T. Gottschall, O. Gutfleisch, *et al.*, "First-principles calculation of the instability leading to giant inverse magnetocaloric effects," *Physical Review B*, vol. 89, no. 18, p. 184403, 2014.

[109] P. Brown, A. Y. Bargawi, J. Crangle, K.-U. Neumann, and K. Ziebeck, "Direct observation of a band jahn-teller effect in the martensitic phase transition of Ni_2MnGa," *Journal of Physics: Condensed Matter*, vol. 11, no. 24, p. 4715, 1999.

[110] P. Lázpita, J. Gutiérrez, J. Barandiarán, V. Chernenko, C. Mondelli, and L. Chapon, "Magnetic moment distribution modeling in non stoichiometric Ni–Mn–Ga ferromagnetic shape memory alloys," in *Journal of Physics: Conference Series*, vol. 549, p. 012016, IOP Publishing, 2014.

[111] C. Shull, E. Wollan, G. Morton, and W. Davidson, "Neutron diffraction studies of NaH and NaD," *Physical Review*, vol. 73, no. 8, p. 842, 1948.

[112] J. Rodríguez-Carvajal, "Recent advances in magnetic structure determination by neutron powder diffraction," *Physica B: Condensed Matter*, vol. 192, no. 1-2, pp. 55–69, 1993.

[113] V. A. Chernenko, V. A. L vov, V. V. Khovailo, T. Takagi, T. Kanomata, T. Suzuki, and R. Kainuma, "Interdependence between the magnetic properties and lattice parameters of Ni–Mn–Ga martensite," *Journal of Physics: Condensed Matter*, vol. 16, pp. 8345–8352, Nov. 2004.

[114] V. Recarte, J. Pérez-Landazábal, V. Sánchez-Alarcos, and J. Rodríguez-Velamazán, "Study of the transformation sequence on a high temperature martensitic transformation Ni-Mn-Ga-Co shape memory alloy," in *Journal of Physics: Conference Series*, vol. 549, p. 012017, IOP Publishing, 2014.

[115] P. Lázpita, J. Barandiarán, J. Gutiérrez, J. Feuchtwanger, V. Chernenko, and M. Richard, "Magnetic moment and chemical order in off-stoichiometric Ni-Mn-Ga ferromagnetic shape memory alloys," *New Journal of Physics*, vol. 13, no. 3, p. 033039, 2011.

[116] E. Şaşıoğlu, L. M. Sandratskii, and P. Bruno, "Role of conduction electrons in mediating exchange interactions in Mn-based heusler alloys," *Physical Review B*, vol. 77, no. 6, p. 064417, 2008.

[117] J. Kübler, A. William, and C. Sommers, "Formation and coupling of magnetic moments in heusler alloys," *Physical Review B*, vol. 28, no. 4, p. 1745, 1983.

[118] V. Recarte, J. Perez-Landazabal, V. Sanchez-Alarcos, E. Cesari, M. Jiménez-Ruiz, K. Schmalzl, and V. Chernenko, "Direct evidence of the magnetoelastic interaction in Ni_2MnGa magnetic shape memory system," *Applied Physics Letters*, vol. 102, no. 20, p. 201906, 2013.

[119] P. Lázpita, J. Barandiarán, J. Gutiérrez, C. Mondelli, A. Sozinov, and V. Chernenko, "Polarized neutron study of Ni–Mn–Ga alloys: Site-specific spin density affected by martensitic transformation," *Physical review letters*, vol. 119, no. 15, p. 155701, 2017.

[120] K. Momma, T. Ikeda, A. A. Belik, and F. Izumi, "Dysnomia, a computer program for maximum-entropy method (mem) analysis and its performance in the mem-based pattern fitting," *Powder Diffraction*, vol. 28, no. 3, pp. 184–193, 2013.

[121] J. Nocedal, "Updating quasi-newton matrices with limited storage," *Mathematics of computation*, vol. 35, no. 151, pp. 773–782, 1980.

[122] C. Frontera and J. Rodríguez-Carvajal, "Fullprof as a new tool for flipping ratio analysis," *Physica B: Condensed Matter*, vol. 335, no. 1-4, pp. 219–222, 2003.

[123] P. Schleger, A. Puig-Molina, E. Ressouche, O. Rutty, and J. Schweizer, "A general maximum-entropy method for model-free reconstructions of magnetization densities from polarized neutron diffraction data," *Acta Crystallographica Section A: Foundations of Crystallography*, vol. 53, no. 4, pp. 426–435, 1997.

[124] K. Momma and F. Izumi, "Vesta 3 for three-dimensional visualization of crystal, volumetric and morphology data," *Journal of applied crystallography*, vol. 44, no. 6, pp. 1272–1276, 2011.

[125] L. Straka, H. Hänninen, A. Soroka, and A. Sozinov, "Ni-Mn-Ga single crystals with very low twinning stress," vol. 303, no. 1, p. 012079, 2011.

[126] P. Müllner, V. Chernenko, and G. Kostorz, "A microscopic approach to the magnetic-field-induced deformation of martensite (magnetoplasticity)," *Journal of Magnetism and Magnetic Materials*, vol. 267, pp. 325–334, Dec. 2003.

[127] L. Straka, J. Drahokoupil, O. Pacherová, K. Richterová, V. Kopecký, H. Hänninen, and O. Heczko, "Thermally induced changes of structure in $Ni_{50}Mn_{25+x}Ga_{25-x}$ magnetic shape memory single crystals with very low twinning stress," *Smart Materials and Structures*, vol. 25, p. 025001, Feb. 2016. arXiv: 1411.1550.

[128] V. A. L'vov and V. A. Chernenko, "Magnetic Anisotropy of Ferromagnetic Martensites," *Materials Science Forum*, vol. 684, pp. 31–47, May 2011.

[129] N. Glavatska, G. Mogilniy, I. Glavatsky, S. Danilkin, D. Hohlwein, A. Beskrovnij, and V. K. Lindroos, "Temperature dependence of martensite structure and its effect on magnetic-field-induced strain in Ni_2MnGa magnetic shape memory alloys," *Journal de Physique IV (Proceedings)*, vol. 112, pp. 963–967, Oct. 2003.

[130] L. Straka, O. Heczko, and H. Hänninen, "Activation of magnetic shape memory effect in Ni–Mn–Ga alloys by mechanical and magnetic treatment," *Acta Materialia*, vol. 56, no. 19, pp. 5492–5499, 2008.

[131] O. Heczko, L. Straka, V. Novak, and S. Fähler, "Magnetic anisotropy of nonmodulated Ni–Mn–Ga martensite revisited," *Journal of Applied Physics*, vol. 107, p. 09A914, May 2010.

[132] L. Straka, O. Heczko, and K. Ullakko, "Investigation of magnetic anisotropy of Ni–Mn–Ga seven-layered orthorhombic martensite," *Journal of magnetism and magnetic materials*, vol. 272, pp. 2049–2050, 2004.

[133] O. Söderberg, L. Straka, V. Novák, O. Heczko, S.-P. Hannula, and V. Lindroos, "Tensile/compressive behaviour of non-layered tetragonal ni52. 8mn25. 7ga21. 5 alloy," *Materials Science and Engineering: A*, vol. 386, no. 1-2, pp. 27–33, 2004.

[134] L. Straka, A. Soroka, H. Seiner, H. Hänninen, and A. Sozinov, "Temperature dependence of twinning stress of type I and type II twins in 10M modulated Ni–Mn–Ga martensite," *Scripta Materialia*, vol. 67, no. 1, pp. 25–28, 2012.

[135] A. Sozinov, A. A. Likhachev, N. Lanska, O. Söderberg, K. Koho, K. Ullakko, and V. K. Lindroos, "Stress-induced variant rearrangement in Ni-Mn-Ga single crystals with nonlayered tetragonal martensitic structure," *Journal de Physique IV (Proceedings)*, vol. 115, pp. 121–128, June 2004.

[136] P. Müllner and A. King, "Deformation of hierarchically twinned martensite," *Acta Materialia*, vol. 58, no. 16, pp. 5242–5261, 2010.

[137] M. Chmielus, K. Rolfs, R. Wimpory, W. Reimers, P. Müllner, and R. Schneider, "Effects of surface roughness and training on the twinning stress of Ni–Mn–Ga single crystals," *Acta Materialia*, vol. 58, pp. 3952–3962, June 2010.

[138] M. Chmielus, C. Witherspoon, K. Ullakko, P. Müllner, and R. Schneider, "Effects of surface damage on twinning stress and the stability of twin microstructures of magnetic shape memory alloys," *Acta Materialia*, vol. 59, pp. 2948–2956, May 2011.

[139] O. Heczko, "Magnetic shape memory effect and magnetization reversal," *Journal of Magnetism and Magnetic Materials*, vol. 290, pp. 787–794, 2005.

[140] L. Straka and O. Heczko, "Magnetic anisotropy in Ni–Mn–Ga martensites," *Journal of Applied Physics*, vol. 93, no. 10, pp. 8636–8638, 2003.

[141] A. Sozinov, A. A. Likhachev, and K. Ullakko, "Magnetic and magnetomechanical properties of Ni-Mn-Ga alloys with easy axis and easy plane of magnetization," in *Smart Structures and Materials 2001: Active Materials: Behavior and Mechanics*, vol. 4333, pp. 189–197, International Society for Optics and Photonics, 2001.

[142] S. Chikazumi and C. D. Graham, *Physics of Ferromagnetism 2e*, vol. 94. Oxford University Press on Demand, 2009.

[143] F. Albertini, L. Pareti, A. Paoluzi, L. Morellon, P. Algarabel, M. Ibarra, and L. Righi, "Composition and temperature dependence of the magnetocrystalline anisotropy in $Ni_{2+x}Mn_{1+y}Ga_{1+z}$ (x+y+z= 0) heusler alloys," *Applied physics letters*, vol. 81, no. 21, pp. 4032–4034, 2002.

[144] S. S. A. Razee, J. B. Staunton, B. Ginatempo, E. Bruno, and F. J. Pinski, "Ab initio theoretical description of the dependence of magnetocrystalline anisotropy on both compositional order and lattice distortion in transition metal alloys," *Physical Review B*, vol. 64, June 2001.

[145] J. Enkovaara, A. Ayuela, L. Nordström, and R. M. Nieminen, "Magnetic anisotropy in Ni_2MnGa," *Physical Review B*, vol. 65, Mar. 2002.

[146] V. Chernenko, V. L'vov, E. Cesari, J. Pons, R. Portier, and S. Zagorodnyuk, "New aspects of structural and magnetic behaviour of martensites in Ni–Mn–Ga alloys," *Materials TransactionsThe relation between lattice parameters and very low twinning stress*, vol. 43, no. 5, pp. 856–860, 2002.

[147] J. Davies, *Conduction and induction heating*. No. 11, IET, 1990.

[148] S. Koohpayeh, D. Fort, and J. Abell, "The optical floating zone technique: A review of experimental procedures with special reference to oxides," *Progress in Crystal Growth and Characterization of Materials*, vol. 54, no. 3-4, pp. 121–137, 2008.

[149] A. Cröll, "German association crystal growth (dgkk)," *Newsletter*, vol. 65, p. 13, 1997.

[150] G. E. Bacon, *Neutron diffraction*. Clarendon Press, Oxford, 1975.

[151] J. M. Cowley, *Diffraction physics*. Elsevier, 1995.

[152] A. H. Compton and S. K. Allison, "X-rays in theory and experiment," 1935.

[153] L. Dobrzynski and K. Blinowski, *Neutrons and solid state physics*. Prentice Hall, 1994.

[154] J. Rodríguez-Carvajal, "Recent developments of the program fullprof," *Commission on powder diffraction (IUCr). Newsletter*, vol. 26, pp. 12–19, 2001.

[155] Website, "Instituto laue-langevin, neutrons for science https://www.ill.eu/fr."

[156] A. Ul-Hamid, "A beginners' guide to scanning electron microscopy."

[157] W. Zhou and Z. L. Wang, *Scanning microscopy for nanotechnology: techniques and applications*. Springer science & business media, 2007.

[158] G. Höhne, W. Hemminger, and H.-J. Flammersheim, "Types of differential scanning calorimeters and modes of operation," in *Differential Scanning Calorimetry*, pp. 9–30, Springer, 2003.

[159] K. P. Menard, *Dynamic mechanical analysis: a practical introduction*. CRC press, 2008.

[160] E. Faran and D. Shilo, "Ferromagnetic shape memory alloys challenges, applications, and experimental characterization," *Experimental Techniques*, 2015.

[161] S. Foner, "Vibrating sample magnetometer," *Review of Scientific Instruments*, vol. 27, no. 7, pp. 548–548, 1956.